

EXPERIMENTAL AND NUMERICAL INVESTIGATION OF DAMAGE
INDUCED BY TRANSVERSE IMPACT IN COMPOSITE BEAMS AND
PLATES

A THESIS SUBMITTED TO
THE GRADUATE SCHOOL OF NATURAL AND APPLIED SCIENCES
OF
MIDDLE EAST TECHNICAL UNIVERSITY



BY

MİRAC ONUR BOZKURT

IN PARTIAL FULFILLMENT OF THE REQUIREMENTS
FOR
THE DEGREE OF MASTER OF SCIENCE
IN
AEROSPACE ENGINEERING

SEPTEMBER 2019

Approval of the thesis:

**EXPERIMENTAL AND NUMERICAL INVESTIGATION OF DAMAGE
INDUCED BY TRANSVERSE IMPACT IN COMPOSITE BEAMS AND
PLATES**

submitted by **MİRAÇ ONUR BOZKURT** in partial fulfillment of the requirements
for the degree of **Master of Science in Aerospace Engineering Department, Middle
East Technical University** by,

Prof. Dr. Halil Kalıpçılar
Dean, Graduate School of **Natural and Applied Sciences**

Prof. Dr. İsmail H. Tuncer
Head of Department, **Aerospace Engineering**

Assoc. Prof. Dr. Demirkan Çöker
Supervisor, **Aerospace Engineering, METU**

Prof. Dr. Kemal Levend Parnas
Co-Supervisor, **Mechanical Engineering, TEDU**

Examining Committee Members:

Prof. Dr. Altan Kayran
Aerospace Engineering, METU

Assoc. Prof. Dr. Demirkan Çöker
Aerospace Engineering, METU

Prof. Dr. Kemal Levend Parnas
Mechanical Engineering, TEDU

Assoc. Prof. Dr. Ercan Gürses
Aerospace Engineering, METU

Assoc. Prof. Dr. Hüsnü Dal
Mechanical Engineering, METU

Date: 10.09.2019



I hereby declare that all information in this document has been obtained and presented in accordance with academic rules and ethical conduct. I also declare that, as required by these rules and conduct, I have fully cited and referenced all material and results that are not original to this work.

Name, Surname: Miraç Onur Bozkurt

Signature:

ABSTRACT

EXPERIMENTAL AND NUMERICAL INVESTIGATION OF DAMAGE INDUCED BY TRANSVERSE IMPACT IN COMPOSITE BEAMS AND PLATES

Bozkurt, Miraç Onur
Master of Science, Aerospace Engineering
Supervisor: Assoc. Prof. Dr. Demirkan Çöker
Co-Supervisor: Prof. Dr. Kemal Levend Parnas

September 2019, 135 pages

Engineering parts made of composite material are susceptible to impacts such as tool drop, hail strike, and bird strike. Since impact induced damage leads to considerable losses in the residual strength, damage mechanisms should be understood well and modelled accurately. For this purpose, damage process in composite laminates under low-velocity impact is investigated experimentally and numerically for two geometries: (i) beams and (ii) plates.

In the first part of the thesis, experimental and numerical study of 2-D line impact on $[0_5/90_3]_s$ and $[90_5/0_3]_s$ CFRP beam specimens are conducted. The experiments using an in-house built drop-weight test setup where micro-crack formation and delamination propagation sequences in $[0_5/90_3]_s$ beams are captured for the first time via ultra-high-speed camera system at rates up to 525,000 fps. Strain fields prior to failure are calculated with digital image correlation method. Post-mortem damage patterns in the beams are characterized using a digital microscope. Finite element simulations of the beam experiments are conducted in ABAQUS/Explicit. Composite ply damage is simulated via a continuum damage model with LaRC04 initiation criteria. Cohesive zone method is used to simulate delamination damage.

In the second part of the thesis, experimental and numerical study of standard drop-weight impact on $[0_8/90_2]_s$ and $[0_4/90_4/0_2]_s$ CFRP and GFRP plates are carried out. Final delamination patterns in the plates are captured using non-destructive inspection techniques. In the numerical part, virtual test setup is modeled in ABAQUS/Explicit to simulate impact test on plate specimens. A 3-D continuum damage mechanics based ply material model with Hashin failure criteria is developed and implemented into the finite element model via a user-written subroutine VUMAT. Delamination damage is simulated by inserting cohesive elements at the interfaces of plies having different orientations. Results of the simulations agreed well with the experimental results in terms of initiation, propagation and final pattern of the impact induced damage.

Keywords: Composite, Low-velocity Impact, Virtual Test Setup, Delamination, Matrix Cracking

ÖZ

KOMPOZİT KİRİŞ VE PLAKALARDA DÜZLEM DIŞI DARBEYE BAĞLI OLUŞAN HASARIN DENEYSEL VE SAYISAL OLARAK İNCELENMESİ

Bozkurt, Miraç Onur
Yüksek Lisans, Havacılık ve Uzay Mühendisliği
Tez Danışmanı: Doç. Dr. Demirkan Çöker
Ortak Tez Danışmanı: Prof. Dr. Kemal Levend Parnas

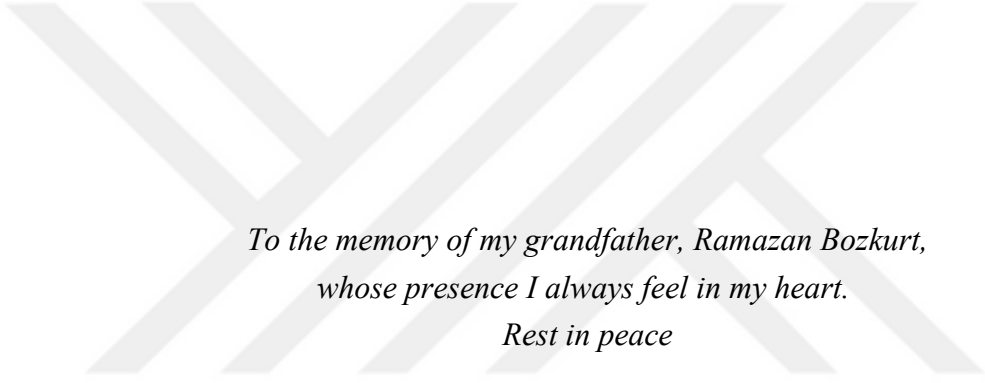
Eylül 2019, 135 sayfa

Kompozit malzemelerden yapılan mühendislik parçaları, takım düşmesi, dolu çarpması ve kuş çarpması gibi darbelere maruz kalmaktadırlar. Darbe kaynaklı hasar, kalıntı gücünde önemli kayıplara neden olduğundan, hasar mekanizmaları iyi anlaşılmalı ve doğru bir şekilde modellenmelidir. Bu amaçla, kompozit kiriş ve levhalarda düşük hızlı darbe altındaki hasarın oluşum süreci deneysel ve sayısal olarak incelenmiştir.

Tezin ilk kısmında, $[0_5/90_3]_s$ ve $[90_5/0_3]_s$ CFRP kirişlerinin iki boyutlu çizgisel darbe deneyleri ve simülasyonları çalışılmıştır. Deneyler, el yapımı bir düşen ağırlık test düzeneği kullanılarak gerçekleştirilmiştir ve $[0_5/90_3]_s$ kirişlerdeki mikro-çatlak oluşumu ve delaminasyon ilerleme süreçleri, yüksek hızlı kamera sistemi ile 525.000 kare/s'ye kadar ulaşan hızlarda görüntülenmiştir. Hasar öncesi gerinim alanları dijital görüntü korelasyon yöntemiyle hesaplanmıştır. Kirişlerdeki nihai hasar dağılımları, dijital bir mikroskop kullanılarak karakterize edilmiştir. Kiriş deneylerinin sonlu elemanlar analizleri ABAQUS/Explicit'te gerçekleştirilmiştir. Kompozit katman hasarı, LaRC04 başlangıç kriterine sahip bir sürekli ortam hasar modeli ile simüle edilmiştir. Delaminasyon hasarının simülasyonu için yapışkan arayüz yöntemi kullanılmıştır.

Tezin ikinci kısmında, $[0_8/90_2]_s$ ve $[0_4/90_4/0_2]_s$ CFRP ve GFRP plakaların standart ağırlık düşürme deneyleri ve bu deneylerin simülasyonları çalışılmıştır. Plakalardaki nihai delaminasyon dağılımları, tahribatsız muayene teknikleri kullanılarak görüntülenmiştir. Çalışmanın sayısal bölümünde, kiriş ve plaka kuponları üzerinde yapılan darbe testlerini simüle etmek amacıyla ABAQUS/Explicit'te bir sanal darbe test düzeneği modellenmiştir. Hashin hasar başlangıç kriterine sahip sürekli hasarı mekaniği temelli 3-B bir katman malzeme modeli geliştirilmiş ve kullanıcı tarafından yazılmış bir VUMAT altprogramı ile sonlu elemanlar modeline uygulanmıştır. Delaminasyon hasarı, farklı yönelimli katmanların arayüzlerine yapışkan elemanlar yerleştirilerek simüle edilmiştir. Çalışmanın genelinde, simülasyon ve deney sonuçları arasında, darbenin neden olduğu hasarın başlangıcı, ilerlemesi ve nihai şekli bakımından iyi bir uyum elde edilmiştir.

Anahtar Kelimeler: Kompozit, Düşük Hızlı Darbe, Sanal Test Düzeneği, Delaminasyon, Matris Çatlaması



*To the memory of my grandfather, Ramazan Bozkurt,
whose presence I always feel in my heart.
Rest in peace*

ACKNOWLEDGEMENTS

I would like to express my deepest gratitude to my advisor, Assoc. Prof. Dr. Demirkan Çöker, for his peerless guidance and support during three years of M.Sc. study. I would like to thank my co-supervisor and the coordinator of our DKTM project, Prof. Dr. Levend Parnas, for giving to me the chance of studying with himself for the past three years.

I would also like to acknowledge Assoc. Prof. Dr. Ercan Gürses and Tanay Topaç for their valuable guidance in the early times of my studies. I would like to thank Dr. Altan Kayran and Dr. Hüsnü Dal for attending my thesis defense presentation with their valuable comments. I would also like to acknowledge Prof. Dr. Oğuz Uzol for offering me peaceful working area and opportunity to use METUWIND facilities.

I would like to thank the members of the Coker Research Group, Ahmet Çevik, Burcu Taşdemir, Tamer Tahir Ata, Burak Ogün Yavuz, Can Muyan, Aydın Amireghbali, and our former officemate Dr. Touraj Farsadi for their irreplaceable friendship, assistance and guidance throughout the study. I am also grateful to my friends Bora Ferruh Uz, Ozan Toprak and Mert Çelik for their contributions during building of the in-house drop-weight test setup in addition to their marvelous friendships. I would also thank to my unofficial undergraduate assistants Umut Altuntaş and Hagin Bengo for their particular contributions to my studies. I would also like to express my special appreciation to Emine Burçin Özen for her all along mental and physical assistance with a neverending faith in me.

Last but not the least, I would like to acknowledge with gratitude the support and love of my family – my father Orhan Bozkurt, my mother Sema Bozkurt and my little brother Alp Ozan Bozkurt. Thank you very much for your endless love and encouragement that I feel throughout my life.

Finally, part of this study was financially supported by Turkish Aerospace – Rotary Wing Technology Center under contract DKTM/2015/05. Structures and Materials Laboratory of METUWIND and Structural Health Monitoring Laboratory of SU-IMC are acknowledged for use of their facilities during the experiments.



TABLE OF CONTENTS

ABSTRACT	v
ÖZ	vii
ACKNOWLEDGEMENTS.....	x
TABLE OF CONTENTS	xii
LIST OF TABLES.....	xvi
LIST OF FIGURES	xvii
CHAPTERS	
1. INTRODUCTION.....	1
2. EXPERIMENTAL INVESTIGATION OF LOW-VELOCITY IMPACT DAMAGE IN FIBER-REINFORCED COMPOSITE BEAMS	5
2.1. Introduction.....	5
2.2. Experimental Method.....	5
2.2.1. Material and Specimen Preparation	5
2.2.2. Experimental Setup	6
2.2.3. Test Procedure	9
2.3. Experimental Results	11
2.3.1. [0/90] _s Specimens	11
2.3.1.1. Static Tests.....	11
2.3.1.2. Impact Tests.....	24
2.3.2. [90/0] _s Specimens	34
2.3.2.1. Static Tests.....	34
2.3.2.2. Impact Tests.....	37

2.4. Conclusions	40
3. NUMERICAL INVESTIGATION OF LOW-VELOCITY IMPACT DAMAGE IN FIBER-REINFORCED COMPOSITE BEAMS	43
3.1. Introduction	43
3.2. Numerical Method.....	43
3.2.1. Modelling of Composite Damage.....	44
3.2.1.1. Intralaminar Damage Model	44
3.2.1.2. Interlaminar Damage Model	48
3.2.2. Finite Element Model	50
3.2.2.1. Geometry and Boundary Conditions.....	50
3.2.2.2. Material Properties	52
3.2.2.3. Mesh and Element Size.....	53
3.2.2.4. Contact and Friction Models.....	54
3.3. Numerical Results	55
3.3.1. $[0_5/90_3]_s$ Beams	55
3.3.2. $[90_5/0_3]_s$ Beams	65
3.4. Conclusions	67
4. EXPERIMENTAL INVESTIGATION OF LOW-VELOCITY IMPACT DAMAGE IN FIBER-REINFORCED COMPOSITE PLATES.....	69
4.1. Introduction	69
4.2. Analytical Model for Impact Response of Composite Plates.....	69
4.3. Experimental Method	75
4.3.1. Material and Specimen Preparation.....	75
4.3.2. Experimental Setup.....	76

4.3.3. Test Procedure	78
4.3.4. Determination of Impact Energies	80
4.3.4.1. Analytical Determination of Delamination Threshold Energy	80
4.3.4.2. Preliminary Tests to Estimate Impact Energy Levels.....	81
4.3.4.3. Estimation of Impact Energies for Real Specimens	85
4.4. Experimental Results	86
4.4.1. Results of CFRP Specimens	87
4.4.1.1. [0 ₄ /90 ₄ /0 ₂] _s CFRP Plates	87
4.4.1.2. [0 ₈ /90 ₂] _s CFRP Plates.....	89
4.4.2. Results of GFRP Specimens.....	92
4.4.2.1. [0 ₄ /90 ₄ /0 ₂] _s GFRP Plates.....	92
4.4.2.2. [0 ₈ /90 ₂] _s GFRP Plates	95
4.5. Conclusions.....	96
5. NUMERICAL INVESTIGATION OF LOW-VELOCITY IMPACT DAMAGE IN COMPOSITE BEAMS AND PLATES	99
5.1. Introduction.....	99
5.2. Numerical Method	99
5.2.1. Intralaminar Damage Model	99
5.2.1.1. Damage Initiation	99
5.2.1.2. Damage Evolution	104
5.2.2. Interlaminar Damage Model	107
5.2.3. Virtual Test Setup.....	110
5.3. Numerical Results	114
5.3.1. Impact Dynamics.....	114

5.3.2. Ply Damage.....	116
5.3.3. Delamination.....	118
5.4. Conclusions	119
6. CONCLUSIONS	123
6.1. Summary of the Thesis.....	123
6.2. Conclusions of the Study on Composite Beams	123
6.3. Conclusions of the Study on Composite Plates.....	125
6.4. Concluding Remarks and Future Work.....	126
REFERENCES.....	129

LIST OF TABLES

TABLES

Table 2.1. Test matrix for impact and static loading of CFRP composite beams.	11
Table 3.1. Mechanical properties of Hexcel 913C/HTS.....	52
Table 3.2. Interface properties of Hexcel 913C/HTS	53
Table 4.1. Stacking sequences, predicted delamination forces and energies, kF values, and experimental energies of the dummy CFRP and GFRP plates.	82
Table 4.2. Stacking sequences, predicted delamination forces and energies, kF values, and experimental energies of the real CFRP and GFRP specimens.....	86
Table 5.1. Mechanical properties of carbon/epoxy material of plates.....	112
Table 5.2. Interface properties of carbon/epoxy material of plates.	112

LIST OF FIGURES

FIGURES

Figure 2.1. (a) Schematic representation of the specimen geometry and micrographs showing polished surfaces of (b) $[0_5/90_3]_s$ and (c) $[90_5/0_3]_s$ specimens.....	6
Figure 2.2. In-house LVI setup used in the impact tests of beams.	8
Figure 2.3. Experimental setup for static tests	9
Figure 2.4. Load-displacement curves of $[0/90]_s$ – Sta1 and Sta2 specimens under static loading.	12
Figure 2.5. In-situ damage formation in $[0/90]_s$ – Sta2 under static loading captured at 70,000 fps.....	14
Figure 2.6. In-situ damage formation on the left-hand side of $[0/90]_s$ – Sta1 under static loading captured at 525,000 fps	15
Figure 2.7. (a) ϵ_{xx} , (b) ϵ_{yy} , and (c) ϵ_{xy} distributions prior to failures on the $[0/90]_s$ – Sta2 under static loading. (The interframe time is 1.43 μ s for the sequential frames representing failure on one side.).....	18
Figure 2.8. UHSC pictures showing the evolution of the damage under static loading on the right half of $[0_5/90_3]_s$ – Sta1 taken at 525,000 fps. (0 μ s refers to the time of the picture in which a delamination front is seen for the first time)	19
Figure 2.9. Variation of (a) crack tip position with time and (b) crack tip speed with crack length for the delamination shown in Figure 2.8.....	21
Figure 2.10. Post-mortem damage in the $[0_5/90_3]_s$ – Sta2 and close-up views of diagonal matrix cracks and delamination.....	22
Figure 2.11. Post-mortem damage in the $[0_5/90_3]_s$ – Sta1 and close-up views of diagonal matrix cracks.	23
Figure 2.12. Load history recorded in the 9.15 J impact test of $[0_5/90_3]_s$ – Imp1.....	25

Figure 2.13. UHSC pictures showing (a) the intact specimen, (b) formation of the major matrix cracks at the LHS and (c) formation of the single major matrix crack at the RHS of $[0_5/90_3]_s$ – Imp1 under 9.15 J impact.	26
Figure 2.14. ϵ_{xy} distribution prior to failure on the $[0/90]_s$ – Imp2 under 9.15 J impact loading . (The interframe time is 1.43 μs for the sequential frames).....	27
Figure 2.15. UHSC pictures showing the evolution of the impact induced damage on the left half of $[0_5/90_3]_s$ – Imp3 taken at 525,000 fps. (0 μs refers to the time of the picture in which a delamination front is seen for the first time).....	29
Figure 2.16. (a) Crack tip position vs. time and (b) crack tip speed vs. time graphs for the delamination at the top 0/90 interface.....	32
Figure 2.17. Post-mortem damage in the $[0_5/90_3]_s$ – Imp1 and close-up views of diagonal matrix cracks and delamination.	33
Figure 2.18. Post-mortem damage in the $[0_5/90_3]_s$ – Imp3 and close-up views of diagonal matrix cracks and micro-matrix cracks.....	34
Figure 2.19. Schematic representation of damage formation sequence in $[90/0]_s$ – Sta1 under static loading.....	35
Figure 2.20. (a) ϵ_{xx} strain distribution before each local failure and (b) damage state after each local failure in the $[90_5/0_3]_s$ – Sta1 under static loading.	36
Figure 2.21. Post-mortem damage in the $[90_5/0_3]_s$ – Sta1 and close-up views of vertical matrix cracks and delaminations.	37
Figure 2.22. In-situ damage formation in $[90/0]_s$ – Imp1 under 7.32 J impact captured at 60,000 fps.....	38
Figure 2.23. Post-mortem damage in the $[90_5/0_3]_s$ – Imp1 and close-up views of vertical matrix cracks and delamination.	39
Figure 3.1. Constitutive bilinear stress – displacement response for intralaminar damage model.....	46
Figure 3.2. Constitutive traction – separation law for cohesive zone model in mixed-mode	48
Figure 3.3. Geometry, initial conditions and boundary conditions of the line impact finite element model.	51

Figure 3.4. Damage formation sequence in the $[0_5/90_3]_s$ CFRP beam subjected to 9.15 J impact.	56
Figure 3.5. Comparison of the diagonal matrix damage observed in the simulation (left) and the experiment (right).	57
Figure 3.6. Matrix and delaminations damage progression inside the $[0_5/90_3]_s$ CFRP beam visualized via translucent images.	58
Figure 3.7. Tensile matrix damage formation sequence on half portion of the $[0_5/90_3]_s$ CFRP beam together with the pioneer transverse shear stress (τ_{23}) contours observed on the elements under tension stress in the clustered 90° plies.	60
Figure 3.8. Variations of crack tip position for 9.15 J and 7.7 J impact analyses with time in comparison with the experimental measurements.	61
Figure 3.9. Variation of delamination crack tip positions with time for (a) 7.7 J and (b) 9.15 J impact configurations in comparison with the results of static and 9.15 J impact experiments and original finite element analyses of 7.7 J and 9.15 J impact configurations, respectively.	63
Figure 3.10. Damage formation sequence in the $[0_5/90_3]_s$ CFRP beam subjected to 9.15- J impact with 1 mm-shifted impactor.	64
Figure 3.11. Damage formation sequence in the $[90_5/0_3]_s$ CFRP beam subjected to 7.32 J impact	66
Figure 4.1. Three different types of impact response: (a) ballistic impact, (b) impact on an infinite plate, and (c) quasi-static impact [44].	70
Figure 4.2. Impact characterization diagram [43].	75
Figure 4.3. (a) INSTRON 9340 drop tower impact system, (b) specimen fixture, and (c) hemispherical impactor tup.	77
Figure 4.4. Post-mortem damage visualization of (a) GFRP specimens using a monochromatic light source, and (b) CFRP specimens using an optical infrared thermography setup.	78
Figure 4.5. Measurement of (a) GFRP and (b) CFRP plate thicknesses using a digital comparator.	79

Figure 4.6. Post-mortem pictures of the dummy GFRP specimens of (a) $[0_7/25/-25/25/-25/0_9]$ and $kF = 2$, (b) $[0_7/25/-25/25/-25/0_9]$ and $kF = 3$, (c) $[0_7/25/-25/25/-25/0_9]$ and $kF = 2.5$, (d) $[(0_2/90_2)_3/0_4/90_2/0_2]$ and $kF = 2.5$	84
Figure 4.7. Thermography image of a dummy $[(0_2/90_2)_3/0_4/90_2/0_2]$ CFRP specimen showing the delamination damage under 12.5 J impact ($kF = 2.35$).	85
Figure 4.8. Load-displacement curves of $[0_4/90_4/0_2]_s$ CFRP specimens.	87
Figure 4.9. Post-mortem thermography images of the C-IMP-P-4-1 specimen.....	88
Figure 4.10. Post-mortem thermography images of the C-IMP-P-4-2 specimen.....	89
Figure 4.11. Load-displacement curves of $[0_8/90_2]_s$ CFRP specimens.....	90
Figure 4.12. Post-mortem thermography images of the C-IMP-P-5-1 specimen.....	91
Figure 4.13. Post-mortem thermography images of the C-IMP-P-5-2 specimen.....	91
Figure 4.14. Load-displacement curves of $[0_4/90_4/0_2]_s$ GFRP specimens.....	92
Figure 4.15. Post-mortem pictures of the main $[0_4/90_4/0_2]_s$ GFRP specimens of (a) $kF = 1.5$, (b) $kF = 2.5$, (c) $kF = 2.5$, (d) $kF = 2$	94
Figure 4.16. Load-displacement curves of $[0_8/90_2]_s$ GFRP specimens.	95
Figure 4.17. Post-mortem pictures of the main $[0_8/90_2]_s$ GFRP specimens of (a) $kF = 2$, (b) $kF = 2$, (c) $kF = 1.5$	96
Figure 5.1. Variation of the in-situ (a) transverse tensile and (b) inplane shear strengths with thin ply and thick ply models over 1 mm ply thickness for 913 132 HTA UD Carbon Prepreg material.	102
Figure 5.2. Linear softening response for ply material with equivalent stress-strain approach.....	104
Figure 5.3. Mixed-mode bilinear traction-separation response of cohesive material.	107
Figure 5.4. Geometry and boundary conditions of the virtual impact test setup.....	110
Figure 5.5. Composite plate model showing the details of the mesh and the materials defined to the finite elements.....	111
Figure 5.6. (a) Displacement vs. time, (b) load vs. time, and (c) load vs. displacement curves from the finite element analysis of $[0_4/90_4/0_2]_s$ CFRP plate specimen under 15 J - impact.....	115

Figure 5.7. Through-the-thickness views matrix damage distribution under the impact zone at different contact times (Images are taken with multiple cut planes: x-z and y-z).....	117
Figure 5.8. Simulated footprints on the (a) top and (b) bottom surfaces of the plate at the end of the analysis.	118
Figure 5.9. Delamination damage at 0/90 interfaces of the laminate at the end of the simulation ($t_i = 5.00 \text{ ms}$).	119
Figure 5.10. Comparison of the projected delaminations obtained in the 15 J experiment on $[0_4/90_4/0_2]_s$ CFRP plate and its simulation.	121
Figure 5.11. Comparison of impact footprint on top surface of the plate and impact damage in on backface obtained in the simulations and experiments.	121

LIST OF ABBREVIATIONS

ABBREVIATIONS

CDM	Continuum damage mechanics
CFRP	Carbon fiber reinforced polymer
CZM	Cohesive zone method
DCB	Double cantilever beam
DIC	Digital image correlation
ENF	End-notched flexure test
FC	Fiber compression
FE	Finite element
FT	Fiber tension
GFRP	Glass fiber reinforced polymer
LVI	Low-velocity impact
MC	Matrix compression
MT	Matrix tension
NDI	Non-destructive inspection
UHSC	Ultra-high-speed camera

CHAPTER 1

INTRODUCTION

Use of composite materials in aerospace structures becomes increasingly favorable due to their preferable mechanical features such as high inplane strength and stiffness-to-weight ratios. The low strength of composite laminates in through-the-thickness direction, however, has remained a problematic issue. The fact that composite structures are uncontrollably subjected to out-of-plane impact loading causes this weakness to manifest in three major forms of failure mechanisms, namely: matrix cracking, delamination and fiber rupture.

The variety and complexity of failure mechanisms necessitate comprehending the damage formation sequence in a low-velocity impact (LVI) event. In early experimental studies [1] ,[2], damage process is reported to start with matrix cracks and followed by delamination and fiber breakage, respectively. For proper use of multidirectional composite laminates in design of aerospace structures, recent studies attempted accurate numerical simulations of impact induced failure mechanisms. Development of virtual experimental setups by means of simulations based on numerical methods received a particular attention with the aim of reducing the number of tests. Lopes et al. [3], [4] simulated the impact damage on dispersed stacking laminates using continuum damage mechanics (CDM) based composite ply damage model and cohesive zone method (CZM). Further effort was made by Lopes et al. on physically-sound simulation of low-velocity impact on fiber reinforced laminates [5], [6]. They discretized the laminate with a structural mesh and developed an element erosion criterion to simulate fiber split in high energy impact cases. González et al. [7] performed sequential simulations of drop-weight impact and compression after impact tests on composite laminates to assess the residual strength of laboratory coupons under compressive loading. They used a material model accounting for ply failure and

delamination in both type of virtual tests. Soto et al. [8] investigated low velocity impact damage in thin ply laminates. They concluded that matrix cracking effects are negligible for thin ply laminates while delamination and fiber failure are dominant damage modes. Topac et al. [9] investigated in-situ damage process in $[0/90]_s$ composite beams subjected to LVI both experimentally and numerically. They modeled damage in the composite beam using a CDM based failure model with LaRC04 initiation criteria and a delamination model with CZM. Simulation results agreed well with experiments in terms of damage initiation time, location and the interaction of the failure modes.

Fail-safe exercises in the design of parts where advanced composite materials are used made prediction of the failure onset fundamental. Since traditional fully-interactive failure criteria including Tsai-Wu, Tsai-Hill failure criteria and non-interactive failure criteria like maximum stress and strain criteria are insufficient to predict failure modes, Hashin [10], [11] and Puck [12], [13] established partially-interactive mode-based failure criteria. Accurate prediction of failure mechanisms is considered essential for estimation of final collapse. Because of some weaknesses of Hashin criteria about the interaction between stress state and shear strength, several researchers proposed some modifications to Hashin failure criteria. The World-Wide Failure Exercises [14] was conducted to assess the capability of available failure criteria. More recently, NASA published LaRC04 failure criteria [15] which includes shear non-linearity and in-situ strengths. Several studies [3]-[7], [9] used LaRC04 failure criteria in drop-weight impact simulations and obtained good agreement with their experimental results.

The use of failure criteria may not be enough to predict ultimate failure of a composite material due to accumulation of damage until the final collapse. Scalar damage variable which assess the degree of damage between initial and complete failure has been defined by Kachanov [17]. Irreversibility of the damage processes are modeled through the thermodynamics basis of constitutive models. A complementary free energy density function for damaged composite ply has been proposed by Malvern

[18]. Matzenmiller proposed the three-dimensional form of damaged compliance matrix [19]. To model the damage propagation, numerous constitutive damage models in mesoscale have been developed in recent years [20]-[25].

Maimi et al. [25], [26] proposed a continuum damage model for the prediction of the onset and evolution of intralaminar damage mechanisms in fiber-reinforced composites. They used a set of scalar damage variables for failure mechanisms in longitudinal and transverse directions. Crack closure effects under load reversal has been considered. A viscous model is also proposed to alleviate the convergence difficulties related to softening response of the composite materials. The constitutive model was used in succeeding transverse impact studies [3]-[7] and the final damage form obtained in numerical analyses agreed well with the experiments.

In this study, low-velocity impact damage process of composites is investigated in cross-ply beam and plate type composite laminates. The objective is making a correlation between failure mechanisms elucidated via 2D line impact on beam laminates and predicting damage accumulation in plate laminates at the end of LVI induced damage process. The study presented here is considered as a first step toward building a virtual impact test setup with a high-fidelity computational model.

The thesis is structured as follows: In Chapter 2, the sequence of the damage induced by transverse LVI in cross-ply CFRP beams is investigated via in-situ experimentation. In Chapter 3, the damage process observed in the LVI experiments are simulated using an explicit finite element method coupled with continuum damage mechanics based composite damage model and cohesive zone method. In the last chapter, investigation of final damage in cross-ply CFRP and GFRP plates subjected to drop-weight impact tests is performed and modelling of a virtual drop-weight impact test setup is presented including the results of preliminary simulations.



CHAPTER 2

EXPERIMENTAL INVESTIGATION OF LOW-VELOCITY IMPACT DAMAGE IN FIBER-REINFORCED COMPOSITE BEAMS

2.1. Introduction

In the study, static and LVI experiments are conducted on CFRP composite beams. A non-standard drop-weight type LVI setup is designed and manufactured. In the LVI experiments, a cylindrical impactor and a flat beam specimen fixture are used for better understanding of damage mechanisms in parallel to the 2-D line impact approach proposed by Choi et al. [1]. Static tests are carried out on an electromechanical testing machine using the same impactor and specimen fixture. In the experiments, load acting on the steel impactor is measured by an in-line load cell and load history is acquired. Initiation and propagation of the damage are recorded with ultra-high speed camera (UHSC) system. Strain field before damage formation is obtained using DIC method. Micrographs of post-mortem damage patterns are captured by a digital microscope.

2.2. Experimental Method

In this section, experimental method followed in low-velocity impact testing of composite beams is described. Specimen preparation, experimental setup and test procedure are explained in detail.

2.2.1. Material and Specimen Preparation

Beam specimens are manufactured in $[0_5/90_3]_s$ and $[90_5/0_3]_s$ configurations by hand layup technique using Hexcel 913C/HTS unidirectional prepregs and cured with autoclave processing. Two CFRP composite flat plates are inspected with ultrasonic C-Scan to ensure the non-existence of any inherent delamination which might have

arisen during manufacturing. The 4.8 mm-thick plates are cut into 100 mm \times 17 mm beams, as shown in Figure 2.1a, using a diamond cutter. Following the cutting process, one side of each beam are polished with 400-to-4000 grit SiC papers to obtain better in-situ and post-mortem visualization. Polished surfaces are scanned with Huvitz HDS-5800 digital microscope for early diagnosis of any defects which might have been induced by manufacturing or cutting processes. No significant defect detected in the micrographs of the specimens prior to tests (see Figure 2.1b and c).

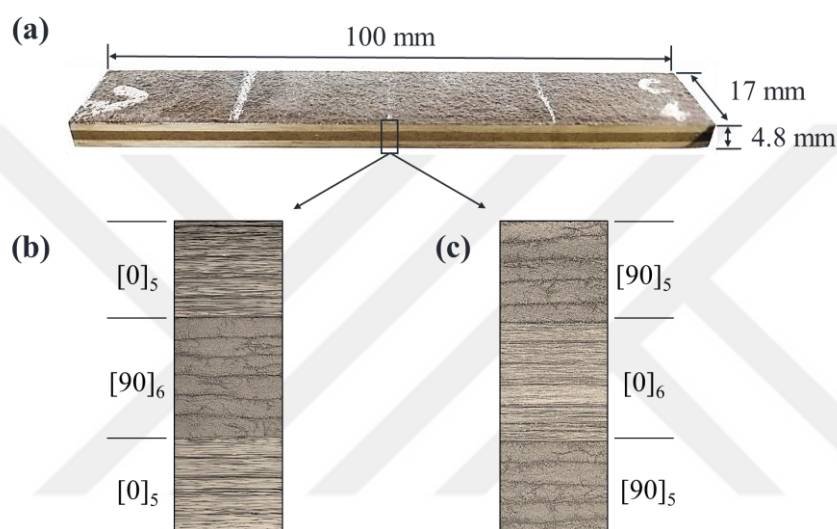


Figure 2.1. (a) Schematic representation of the specimen geometry and micrographs showing polished surfaces of (b) $[0_5/90_3]_s$ and (c) $[90_5/0_3]_s$ specimens

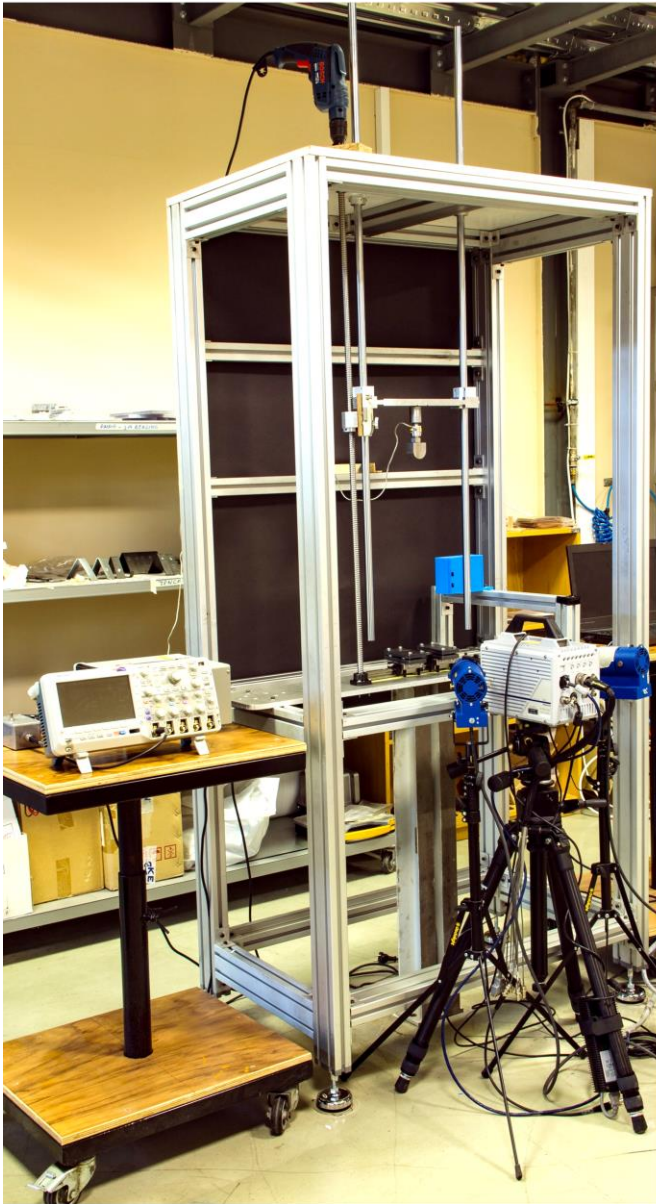
2.2.2. Experimental Setup

To conduct LVI tests, a non-standard drop-weight impact setup, shown in Figure 2.2, is designed and manufactured. The flat beam specimen fixture, which consists of two couples of top and bottom rectangular steel plates placed on linear guideways, allows visualization of the damage process from the side of the beam specimen. Prior to tests, the positions of the guideways, which are adjusted according to unsupported beam length and impact location, are secured to represent fixed end boundary conditions by preventing their sliding towards the impact zone. The specimen is sandwiched by the top and bottom plates and squeezed via bolt and nut fasteners passing through the

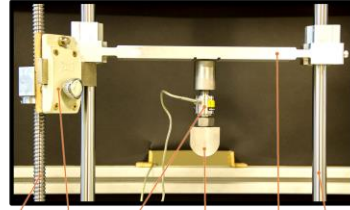
holes located at corners of each plate. The specimen may get thinner under impact loading due to Poisson effect and may slide underneath the plates by overcoming friction created by squeezing. To increase the friction between the plates and the specimen, adhesive regions are created on the inner surfaces of the plates by applying double-sided tapes for a short time and removing them.

Impactor crosshead assembly, shown in Figure 2.2, consists of a steel crosshead, an in-line load cell and a hemi-cylindrical steel impactor located at the tip of the assembly and weighs 1865-g. The 44-kN capacity FUTEK load cell is positioned between the crosshead and the impactor providing that at least 90% of total impact mass stays above it. The crosshead has been designed to allow for extra-weight addition to achieve higher impact energies when necessary. Linear bearings are embedded at both ends of the crosshead and slide almost frictionless over two parallel guiding shafts. Height of the crosshead assembly is adjusted up to a maximum value of 1-m with a ball screw mechanism driven by a drill motor which is preferred for offering high stall torque values. A quick-release mechanism attached on the ball nut holds the crosshead assembly stationary and releases it for free fall when triggered. Velocity indicator system consisting of a flag attached on the crosshead assembly and two subsequent photo-diode emitter/detector sensors measuring the average velocity of the impactor 5-mm above the upper surface of the specimen. The instantaneous velocity of the impactor at the initial contact is calculated by extrapolating the measured velocity.

Data acquisition system of the test setup consists of three main elements: the load cell, an in-house made differential amplifier and an oscilloscope. Differential amplifier receives voltage output generated by the load cell during the contact and amplifies 1000 times by also filtering the noise. Oscilloscope samples the amplified voltage data at a rate of 100 kHz. High frequency ringing oscillations caused by the compliance of the impactor crosshead assembly are filtered by the oscilloscope. After the impactor rebounds from the specimen surface, a piece of sheet metal is slid manually over the specimen to prevent secondary hits to the specimen. Voltage-time data taken by the oscilloscope are converted to load-time data with a post-processing computer code.

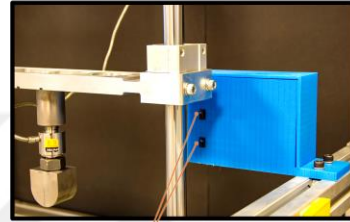


Impactor crosshead assembly



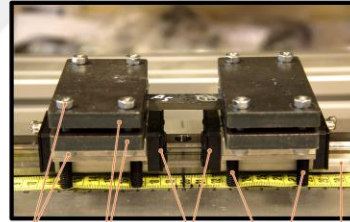
Ball screw Load cell Crosshead
Release mechanism Impactor Guiding shafts

Velocity indicator



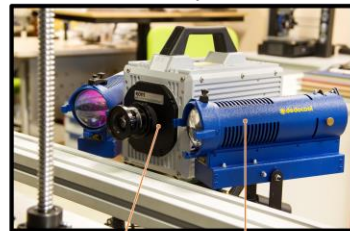
Emitter/detector sensors

Specimen fixture



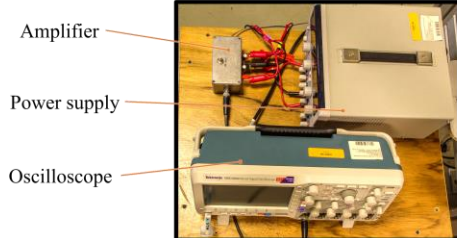
Bolts & nuts Squeezing plates Linear rail guideways Stoppers Linear rail

UHSC system



Ultra-high speed camera Lights

Data acquisition system



Amplifier

Power supply

Oscilloscope

Figure 2.2. In-house LVI setup used in the impact tests of beams.

In static tests, the same boundary conditions are created by installing the impactor and the specimen fixture to 10-kN Shimadzu electromechanical testing machine as seen in Figure 2.3. Static loading is achieved by displacement controlled downward motion of the crosshead at a speed of 0.5 mm/min. Force and displacement data are measured by the load cell embedded to the machine and the machine itself, respectively, and are collected at 10 Hz.

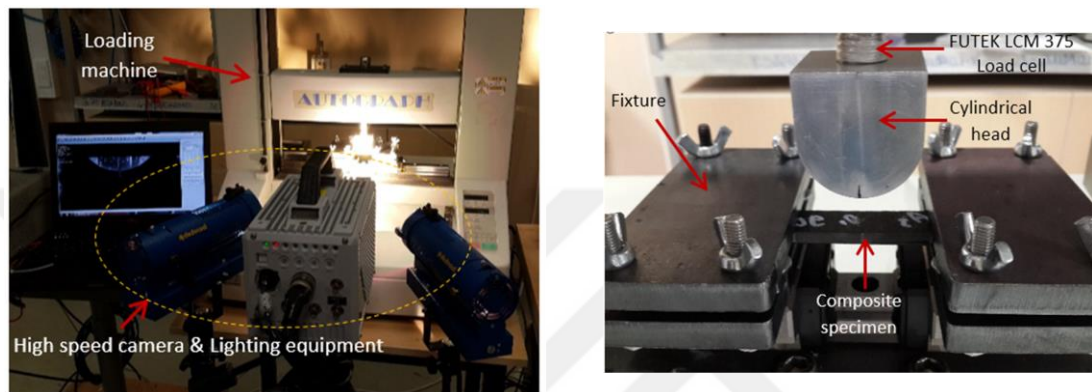


Figure 2.3. Experimental setup for static tests

2.2.3. Test Procedure

The test matrix, seen in Table 1, is constituted considering the number of specimens, parameters affecting the damage and the techniques used for better understanding of damage formation. For $[0_5/90_3]_s$, impact tests are performed at 9.15 impact energy, corresponding to 50 cm release height. For $[90_5/0_3]_s$ layups, on the other hand, 7.32 impact energy is applied by dropping the impactor from 40 cm height. In addition to impact tests, static tests are conducted.

In all impact and static tests, in-situ formation and progression of damage are captured at 70,000 or 525,000 fps via UHSC system seen in Figure 2.2. The UHSC system consists of one Photron SA5 ultra-high speed camera and two Dedocool COOLH lightening systems equipped with 250 W Osram HLX Tungsten lamps. The calibration of the camera is made by adjusting its distance to the side of the specimen and the optical configurations such as lens type, resolution and captured area. At 70,000 fps,

pictures of a 50 mm × 19 mm area including whole unsupported portion of the beam are taken with 512 × 192 pixels resolution by using 50 mm lens and 15 mm extension ring and positioning the camera 36.5 cm far from the specimen side. At 525,000 fps, on the other hand, the same lens and extension ring are used, and the camera is positioned 59 cm far from the specimen side providing that one half of the beam is monitored in a 25 mm × 10 mm area with 128 × 48 pixels resolution. Even though high shutter speeds and high diaphragm opening are preferred to increase brightness and sharpness of the dynamic pictures as much as possible, low resolution of the display limits the discernibility of the damage process especially in the experiments recorded at 525,000 fps. In these experiments, one side of beams are painted white to make matrix and interface damages more apparent.

In one static and one impact test of both $[0_5/90_3]_s$ and $[90_5/0_3]_s$ beams, strain distribution on the specimen is computed during elastic loading using two-dimensional digital image correlation (DIC) method. Polished sides of the specimens on which DIC analysis is performed are white-painted using an air brush to create a stochastic pattern. UHSC pictures with 512×192 pixels resolution are taken at 70,000 fps during failure events in the experiments and are imported to the open software NCORR open DIC software for post-processing. Subset radius is set to 10 pixels with 1 pixel overlapping each other. In the calculations, deformations are computed evaluating the change in the stochastic pattern in each subset between subsequent images. Strains are obtained by time differentiation of the deformation distribution. Radius for strain computation is set to 5 or 6 pixels to obtain qualitatively the best visualization of the strain distribution with these values.

Post-mortem characterization of the damage induced by impact or static loading is performed upon each experiment. For this purpose, micrographs of the damaged specimens are taken by Huvitz HDS-5800 digital microscope at 50×, 200× and 500× magnification levels.

Table 2.1. Test matrix for impact and static loading of CFRP composite beams.

Layup	Specimen	Energy	UHSC capturing rate [fps]	DIC
[0 ₅ /90 ₃] _s	Imp1	9.15 J	70,000	No
	Imp2	9.15 J	70,000	Yes
	Imp3	9.15 J	525,000	No
	Sta1	Static	525,000	No
	Sta2	Static	70,000	Yes
[90 ₅ /0 ₃] _s	Imp1	7.32 J	60,000	No
	Sta1	Static	70,000	Yes

2.3. Experimental Results

In this section, results of the static and impact experiments conducted on [0/90]_s and [90/0]_s CFRP beams are presented.

2.3.1. [0/90]_s Specimens

2.3.1.1. Static Tests

Results of the static experiments of two [0₅/90₃]_s specimens are presented in the following subsections.

Global Response

Two [0/90]_s specimens are loaded statically until that failure is observed in both right and left side of the embedded 90° plies. The load displacement curves obtained from these static tests are shown in Figure 2.4. Although the elastic responses of the specimens are in good agreement, there is an unexpected difference between the initial failure loads. [0/90]_s – Sta2 resists up to a bending load of 5.14 kN, while [0/90]_s – Sta1 is capable of carrying only 3.15 kN before the first load drop. Following the initial failure, both tests are paused manually for a time required to record high speed camera pictures of the failure event. Until the pause, loading continues for a small

amount of time and during the pause, the load decreases slightly. Then, further displacement is applied till the second load drop occurs at 3.39 kN and 3.95 kN for $[0/90]_s$ – Sta1 and Sta2, respectively. These load values are closer to each other in contrast to the first failure loads. One interesting observation on the failure loads is that the load value corresponding to the second load drop is smaller than the one recorded at the first failure for $[0/90]_s$ – Sta2 while the opposite is true for $[0/90]_s$ – Sta1. This may imply that a premature failure occurred in the $[0/90]_s$ – Sta1 specimen and this is investigated in the following sections via high speed camera pictures and micrographs.

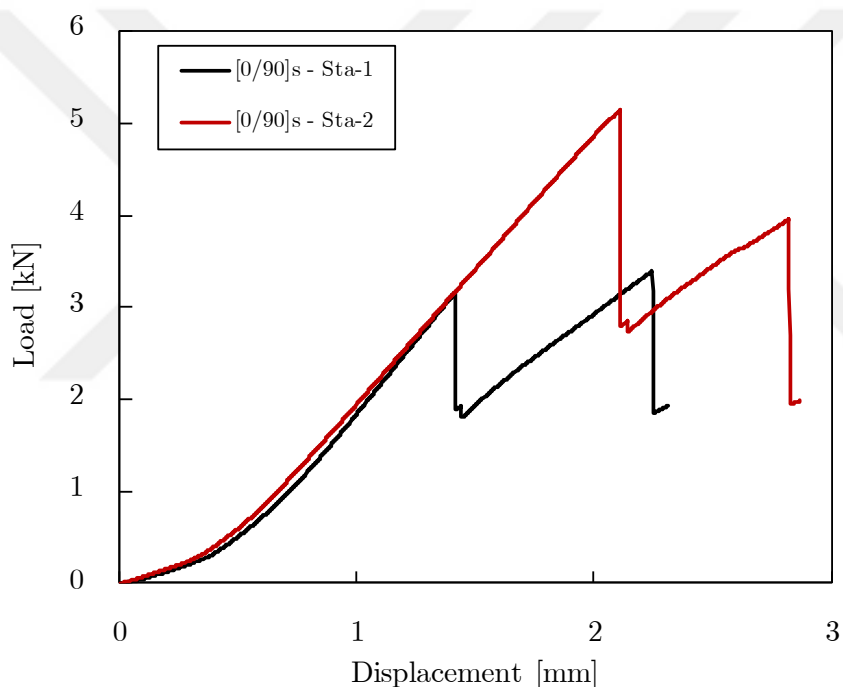


Figure 2.4. Load-displacement curves of $[0/90]_s$ – Sta1 and Sta2 specimens under static loading.

In-situ Damage Characterization

In-situ damage formation in $[0/90]_s$ – Sta2 under static loading is captured at 70,000 fps and presented in Figure 2.5. When the impactor displacement is 2.11 mm, the instant of the last picture showing the intact specimen is taken as reference. At +14.3

μs , a 45° matrix crack inclined to the impact zone is observed in the middle group of 90° layers on the left-hand side of the specimen. The distance of this first matrix crack to the impact line is measured 14.5 mm. At the tips of this matrix crack, small delaminations facing towards impact and clamp zones at the top and bottom $0/90$ interfaces, respectively, are distinguished. At 28.6 μs after the reference, the top delamination is under the impact zone and the tip of the bottom one is in the clamped region and no longer visible. In the next two frames, the top delamination grows gradually until the impact line together with an opening motion.

Similarly, the picture in which the right-hand side of the specimen is seen undamaged for the last time is taken as reference and after 14.3 μs after this instant, a second matrix crack and delaminations nucleated at both interfaces are observed there at an impactor displacement of 2.82 mm. This second matrix crack is almost 45° inclined to the impact zone as the first matrix crack and occurs 19.5 mm away from the impact line. At 28.6 μs after the reference frame, top delaminations seem like merged but post-mortem analysis might provide more clear information about this observation. Delamination opening is also observed through the last three frames. At the last frame, which is captured 42.9 μs after the reference, fibers of the two lowermost layers are broken at a region close to the right-hand side clamped boundary condition and a delamination facing to the impact zone is nucleated by this crack inside the bottom group of 0° layers.

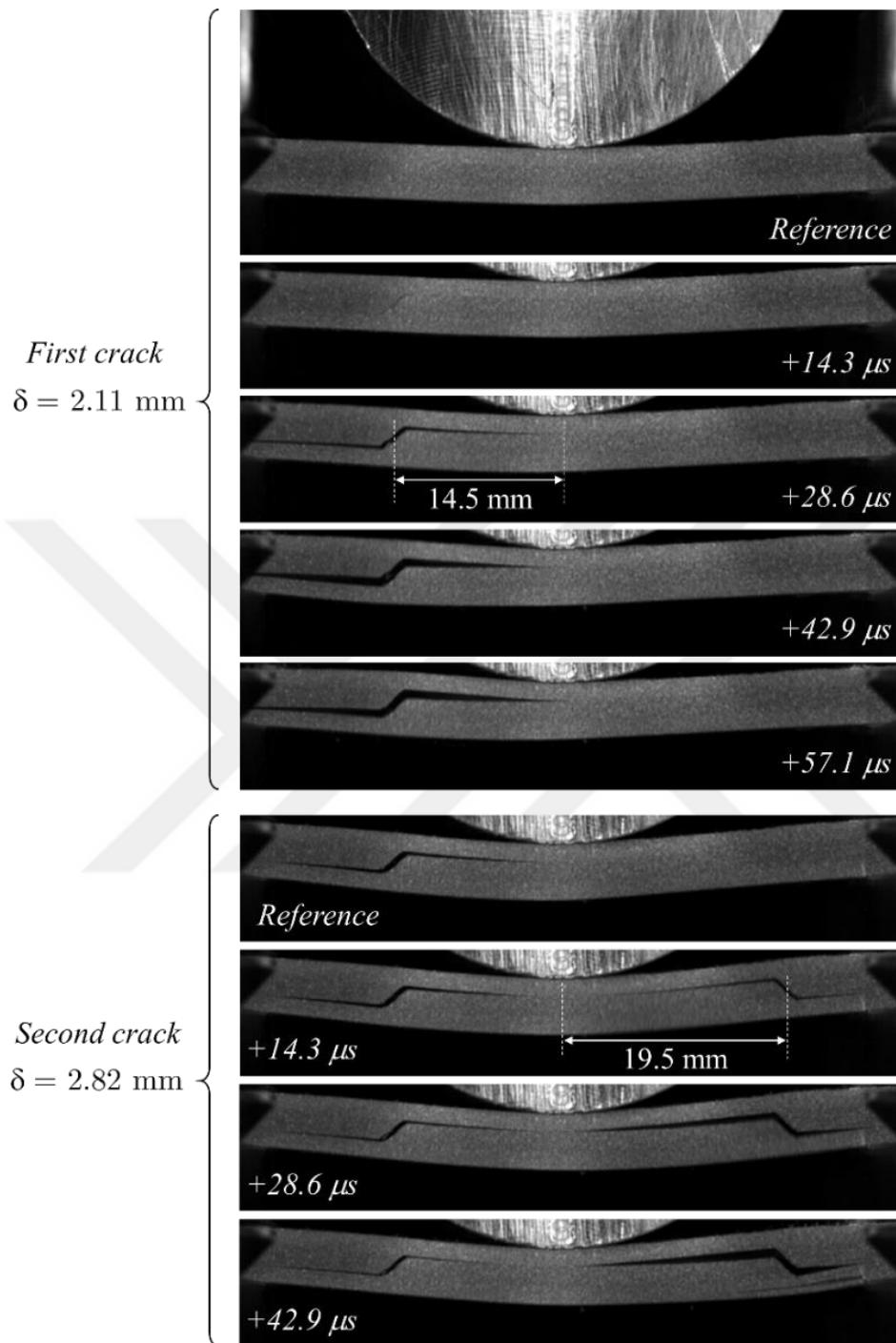


Figure 2.5. In-situ damage formation in $[0/90]_s$ – Sta2 under static loading captured at 70,000 fps.

Formation of the initial damage in static test of the specimen $[0/90]_s$ – Sta1 is recorded at 525,000 fps and presented in Figure 2.6. A diagonal matrix crack occurs 20.8 mm away from the impact line on the left-hand side of the specimen at an impactor displacement of 1.41 mm. This matrix crack does not nucleate any delamination at the interfaces contrary to ordinary. 3867 μ s after the first crack, a second diagonal crack occurs at 13.5 mm from the impact line. Almost 2000 μ s after this matrix crack, delaminations occur at the points where the crack reaches the interfaces. In addition to the premature initial failure of this specimen, the damage sequence is inconsistent with the common observation of damage occurring in $[0/90]_s$ beams. The damage sequence on the right-hand side of the specimen, however, is as usual and presented in the ‘Delamination Propagation’ subsection of this section.

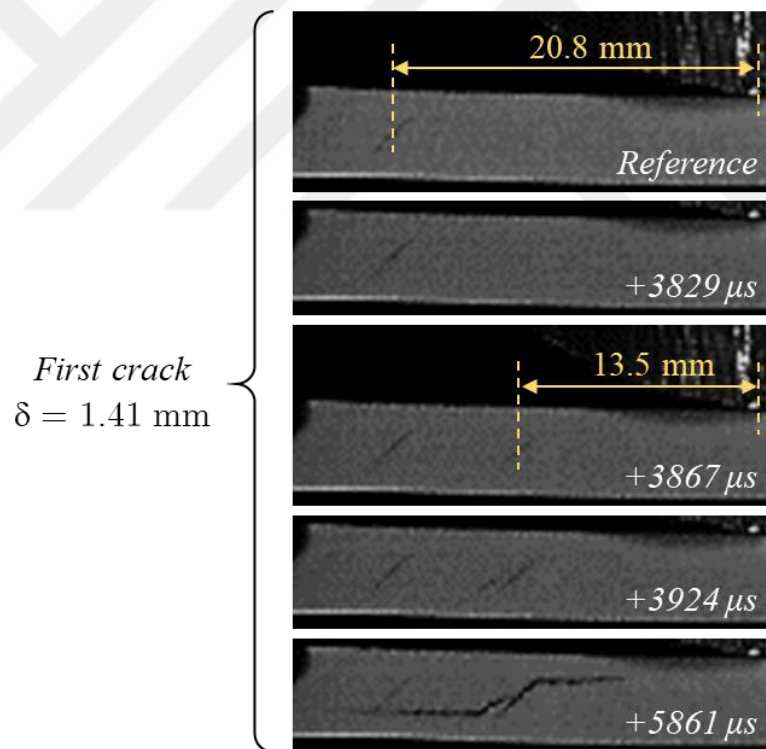


Figure 2.6. In-situ damage formation on the left-hand side of $[0/90]_s$ – Sta1 under static loading captured at 525,000 fps

Digital Image Correlation Analysis

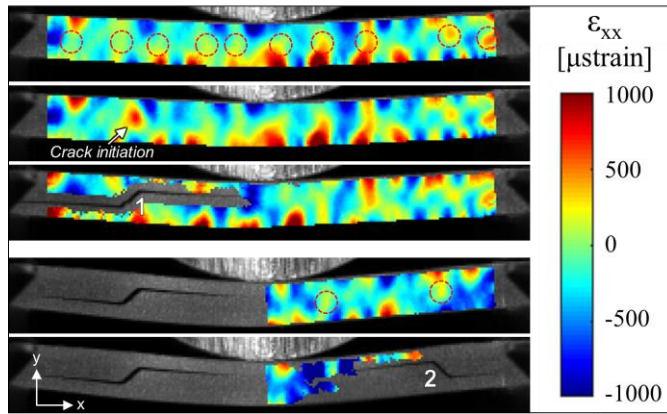
Strain distributions on $[0/90]_s - \text{Sta2}$ prior to failure on left and right-hand sides of the specimen are obtained using DIC method and shown in Figure 2.7. In the figure, ϵ_{xx} , ϵ_{yy} , and ϵ_{xy} components of the strain are presented as (a), (b), and (c), respectively. Each sub-figure consists of 5 frames composing of 3 and 2 sequential frames prior to and at the instant of left and right-hand side failures, respectively. The time interval between the sequential frames counts 1.43 μs . Observations made on the DIC results are as follows:

- In Figure 2.7a and b, red circles point to the positive ϵ_{xx} and ϵ_{yy} zones. Although in Figure 2.7a, the positive zones in the left side are yellow-like ($\sim 250 \mu\text{strain}$) and the ones in the right side are red-like ($\sim 500\text{-}1000 \mu\text{strain}$) generally, initiation of the first crack occurs on the left-hand side of the specimen as shown in 2nd frames. Moreover, the location of this crack is none of these positive spots and remains just between two of them. In case of the second matrix crack which occurs on the other side of the specimen, crack initiates at one of the positive ϵ_{xx} zones encircled with red circles, as seen in last two frames of Figure 2.7a.
- In Figure 2.7b, on the other hand, positive ϵ_{yy} zones are yellow-like except the one located on the right-hand side, implying that the values of the maximum ϵ_{yy} strains are about 500 μstrain except one point. At this point, the ϵ_{yy} is at the order of 1000 μstrain but the initial failure does not occur here. The location of the initial matrix crack overlaps with the one of the positive ϵ_{yy} zones observed on the left-hand side of the specimen. However, none of the positive ϵ_{yy} zones correspond to the initiation of the second matrix crack.
- In Figure 2.7c, high shear stresses (1000-2000 μstrain) are observed along the middle 90° layers on both left and right-hand sides of the specimen. The largest absolute ϵ_{xy} zones ($>1800 \mu\text{strain}$) on this specimen are shown with white circles. It is seen that first matrix crack initiates from one of these hot spots. Similarly, initiation of the second matrix crack occurs at the location of one of

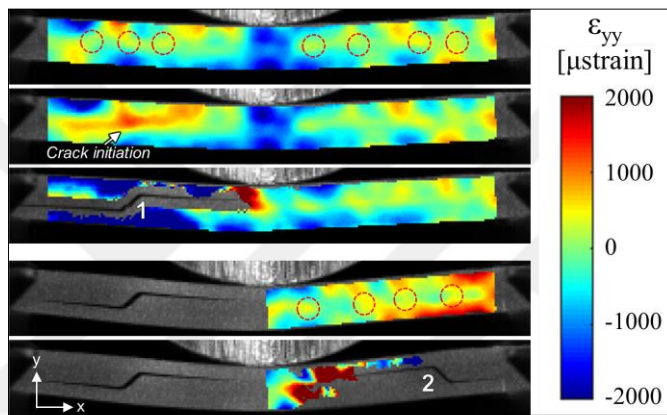
the hot ε_{xy} spots pointed in the 4th frame of Figure 2.7c. Regarding to this consistency and the higher ε_{xy} magnitudes, it can be deduced that formation of these ‘shear cracks’ are controlled by the shear component of the strain in case of these specimen and testing configurations.

Delamination Propagation

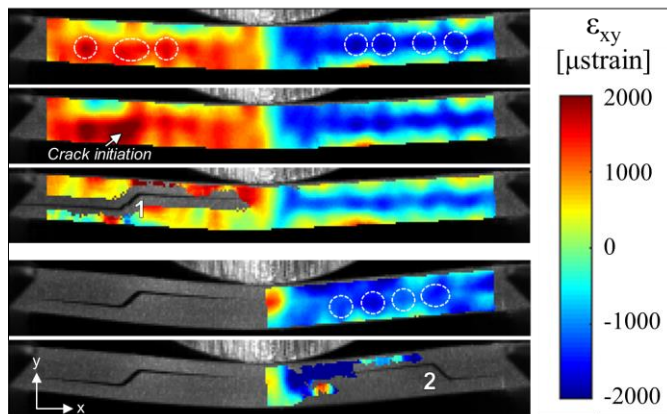
Figure 2.8 shows the UHSC pictures of the damage process in the static testing $[0_3/90_5]_s$ beam on the right half of specimen Sta1 taken at 525,000 fps. Initially, a diagonal matrix crack forms in the group of 90° plies as shown in the blue dashed circle in the first frame. This initial matrix crack is approximately 17.5 mm away from the impact line. After its initiation, it propagates in the 90° plies towards upper and lower 0/90 with an inclined angle. The instant it reaches upper and lower 0/90 interfaces at which delaminations initiate is taken as the reference time, $t = 0$ in Figure 2.8. From this point on, the delamination at the upper interface is followed and its tip is indicated with a blue arrow. The delamination at the lower 0/90 interface which continues towards the right clamped end is out-of-interest. After 19 μs than its initiation, the front of the delamination is seen underneath the impactor at a location close to the impact line and arrests due to high out-of-plane compressive stresses causing crack closure under the impact zone.



(a)



(b)



(c)

Figure 2.7. (a) ϵ_{xx} , (b) ϵ_{yy} , and (c) ϵ_{xy} distributions prior to failures on the $[0/90]_s$ – Sta2 under static loading. (The interframe time is $1.43 \mu\text{s}$ for the sequential frames representing failure on one side.)

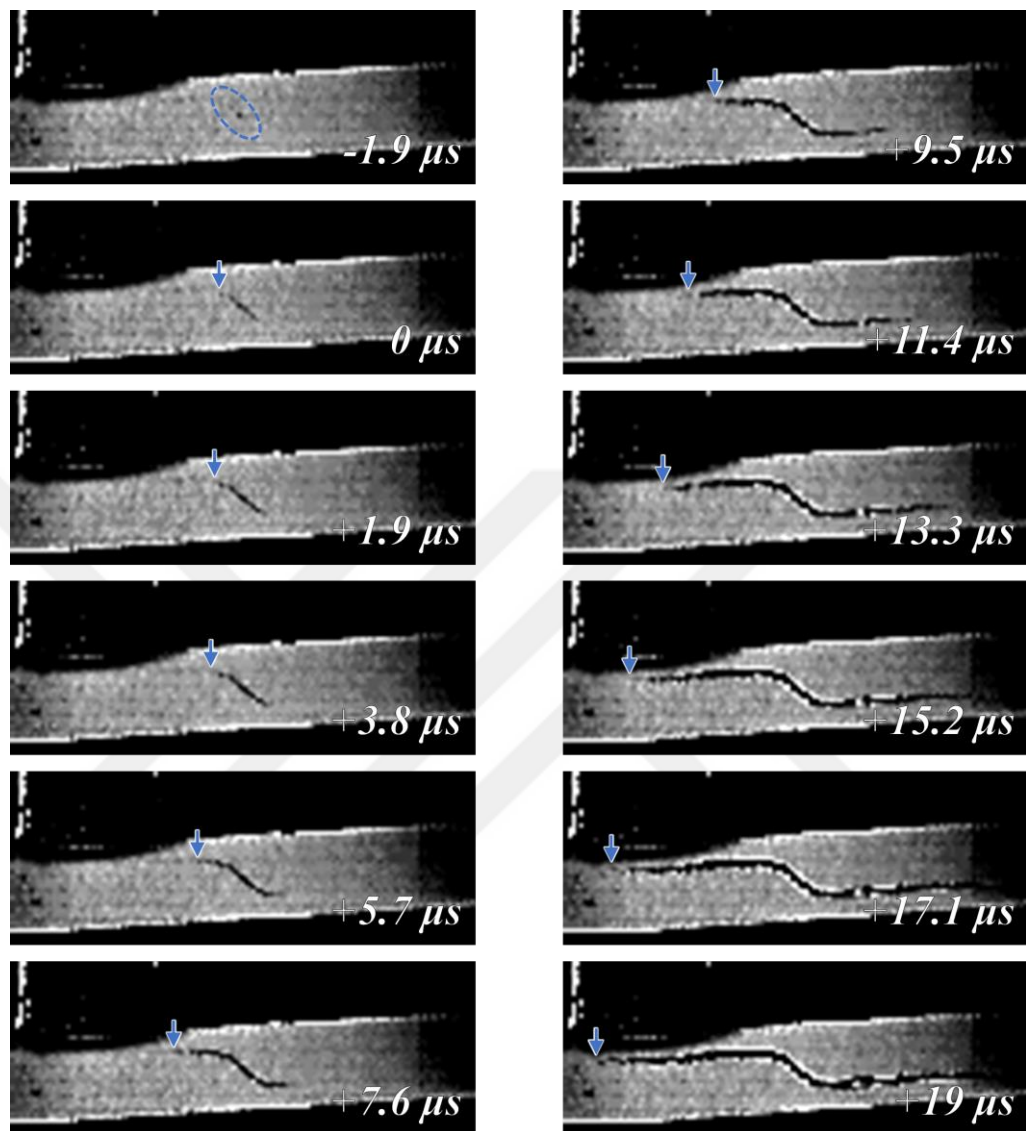


Figure 2.8. UHSC pictures showing the evolution of the damage under static loading on the right half of $[0_5/90_3]_s$ – Sta1 taken at 525,000 fps. ($0 \mu s$ refers to the time of the picture in which a delamination front is seen for the first time)

The delamination crack tip positions as a function of time is shown in Figure 2.9a. The crack tip position is measured from the middle of the beam where initial contact occurs using the sequential frames shown in Figure 2.8. The time at which delamination initiates at the upper $0/90$ interface is taken as $t = 0$, and the positions of

its front is pointed with a blue arrow. Initial delamination forms approximately 11.6 mm away from the impact line, approaches with an increasing slope. In the range of 5 to 15 μs , the delamination continues to propagate with a constant-like slope. After the crack front reaching the impact zone at about $\Delta t = 15.2 \mu\text{s}$, its speed decreases gradually and is arrested while it is 1.6 mm away from the impact line at $\Delta t = 19 \mu\text{s}$.

Crack speeds are calculated using three point numerical differentiation of the crack tip position with respect to time and the variation of the delamination crack tip speeds with time is shown in Figure 2.9b. Delamination initiates with a speed of about 250 m/s. Then, it jumps to 500 m/s in the first 2 μs and remains almost constant until the crack travels approximately 3 mm. After this point, the gradual increase of the crack tip speed is observed, and it reaches a peak value of approximately 850 m/s just before slowing down and being arrested at a maximum crack length of 9.6 mm. The maximum speed that the crack tip reaches is almost half of the transverse Rayleigh wave speed.

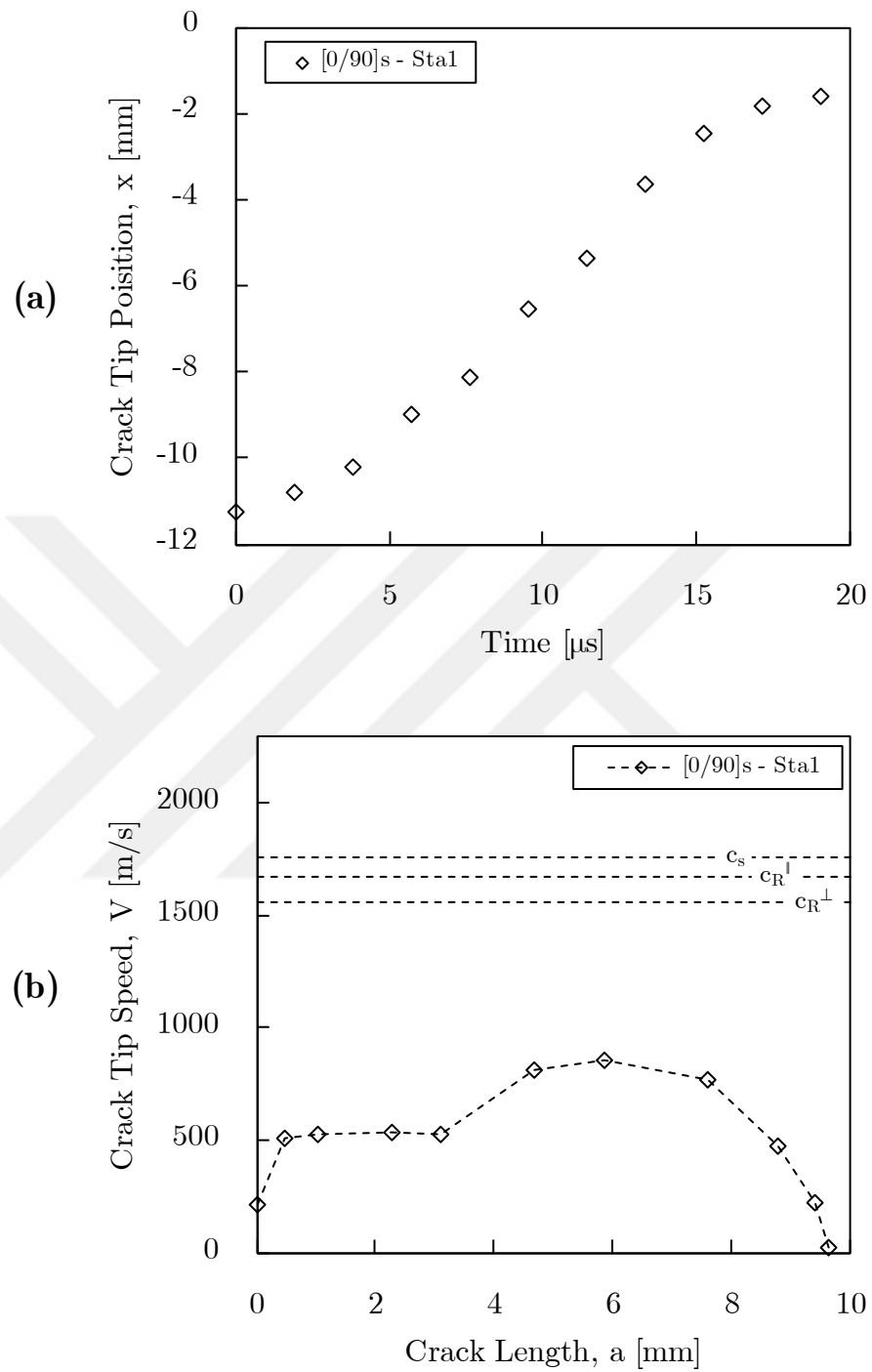


Figure 2.9. Variation of (a) crack tip position with time and (b) crack tip speed with crack length for the delamination shown in Figure 2.8.

Post-mortem Damage Characterization

Post-mortem pictures of the specimens are taken with the digital microscope. Pictures showing the whole span length of the specimens are created using the tiling option at 50x magnification. Close-up pictures of the observed major diagonal matrix cracks which are taken at 200x magnification are shown in red rectangles and their locations are marked on the specimens. Also, the pictures of further observations including micro-matrix cracks or the debris between the delaminated layers are shown in yellow squares.

The final damage pattern in $[0_5/90_3]_s$ – Sta2 consists of two major diagonal matrix cracks, a fiber breakage and multiple delaminations as shown in the micrographs in Figure 2.10. The major diagonal matrix cracks in the middle 90° layers are connected to delaminations at both upper and lower interfaces. The delaminations at the upper interface on each side of the specimen coalesce at the center forming a single delamination. Debris formation inside the lower delamination of the right major diagonal matrix crack is observed as shown in yellow rectangle. A fiber failure zone and a delamination originating from it can be observed near the bottom-right boundary condition.

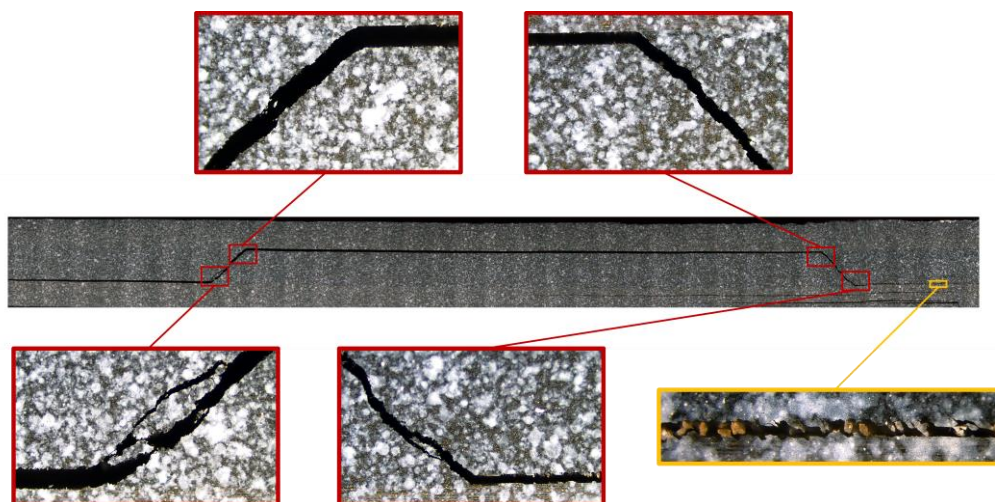


Figure 2.10. Post-mortem damage in the $[0_5/90_3]_s$ – Sta2 and close-up views of diagonal matrix cracks and delamination.

Micrographs of the $[0_5/90_3]_s$ – Sta1 shows that final damage pattern of this specimen includes matrix cracks and delaminations as shown in Figure 2.11. A matrix crack was observed at the far-left end of the span during the experiment. It was also observed that this matrix crack did not nucleate any delamination at the neighbor interfaces. However, this unusual crack formation is assumed as the main reason for premature failure of $[0_5/90_3]_s$ – Sta1. Close-up picture of this matrix crack shown in yellow rectangle reveals that it does not provoke any delamination at the top and bottom interfaces in accordance with the in-situ observations. Unlike the $[0_5/90_3]_s$ – Sta1, the major diagonal matrix cracks in the middle 90° layers of this specimen follows a meandering route rather than directly reaching to the upper and lower interfaces. The specimen fails at a relatively lower load level. The common reason for these dissimilarities and inadequacies may be due to the existence of relatively significant defects.

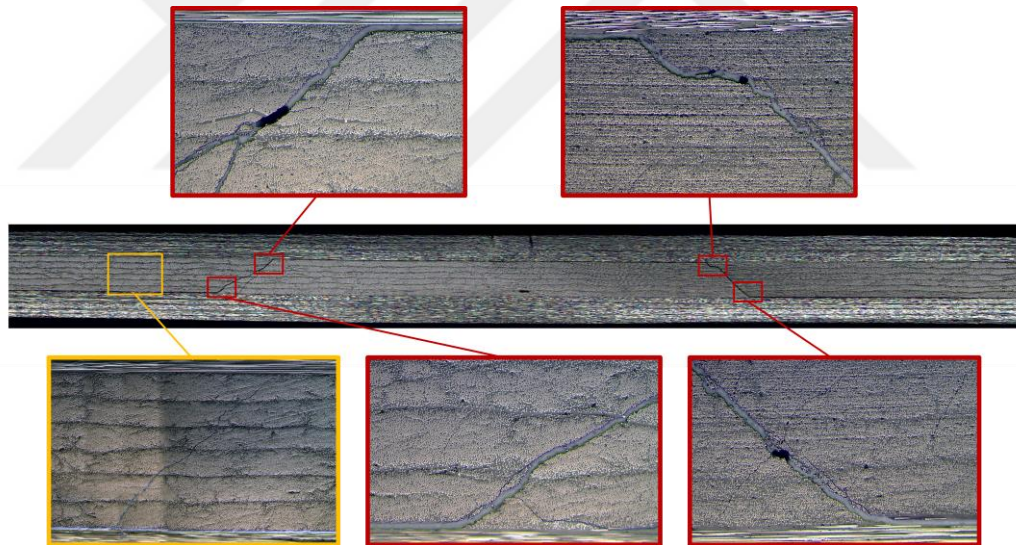


Figure 2.11. Post-mortem damage in the $[0_5/90_3]_s$ – Sta1 and close-up views of diagonal matrix cracks.

2.3.1.2. Impact Tests

Results of the impact experiments conducted on three $[0_5/90_3]_s$ specimens are presented in the following subsections.

Global Response

Among all three the impact experiments, load history could be recorded in only in the test conducted on $[0_5/90_3]_s$ – Imp1. The data in the other two tests could not be acquired because the oscilloscope was triggered by an undesired noise peaks occurring in the meantime between the release of the impactor and the initial contact between the impactor and the specimen.

The load history recorded in the 9.15 J impact test on $[0_5/90_3]_s$ – Imp1 is shown in Figure 2.12. The two significant drops in the load corresponding to the first and the second matrix cracks can be observed in the plot. The time of these drops are consistent with the in-situ measurements made via ultra-high speed camera system (see Figure 2.13). Total contact time is slightly above 4 ms, and this value is also in accordance with the high speed camera pictures.

The impactor displacement was attempted to calculate by integrating acceleration obtained from the equation of motion of the system twice. However, the calculated displacement does not match up with the displacements measured from the high speed camera pictures. Due to the existence of such discrepancy and the lack of further data, global response of the specimens subjected to impact loading should not be evaluated according to load measurement at this time.

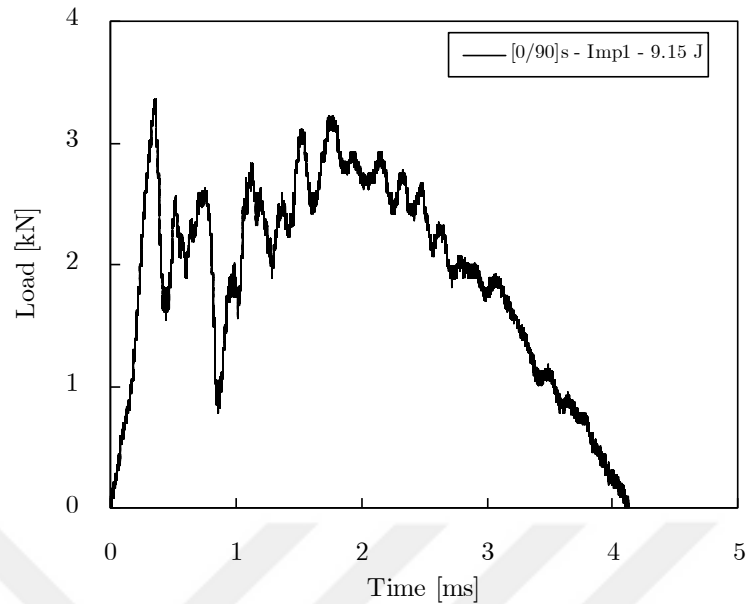
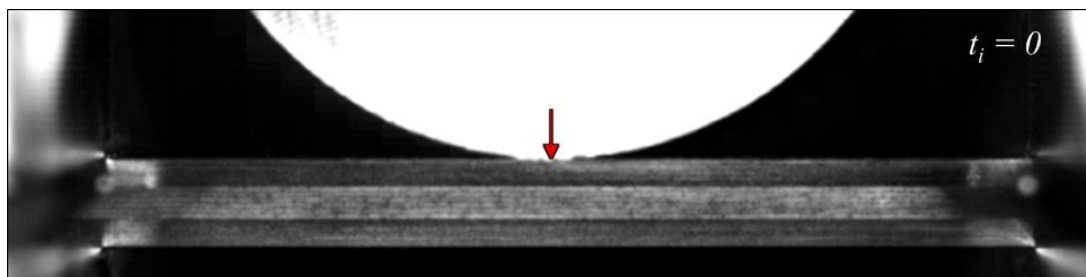


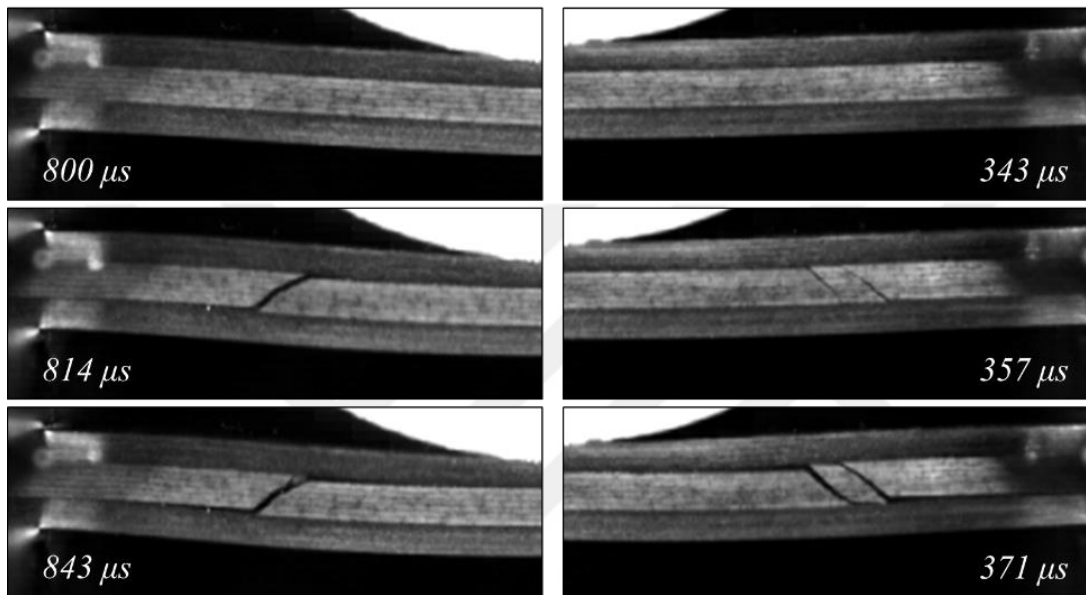
Figure 2.12. Load history recorded in the 9.15 J impact test of $[0_5/90_3]_s - \text{Imp1}$.

In-situ Damage Characterization

In-situ formation of the impact induced damage in $[0_5/90_3]_s - \text{Imp1}$ is shown in Figure 2.13 via the UHSC pictures taken at a capturing rate of 70,000 fps. The instant at which the initial contact between the impactor and the top surface of the specimen, seen in Figure 2.13a is taken as reference. Under the dynamic load generated by a 9.15 J impact, the initial damage occurs at 357 μs as simultaneous diagonal matrix cracks in the middle clustered 90° group of layers at the right hand side of the specimen, as seen in Figure 2.13c. These cracks are inclined to the impact zone with almost 45° angle. At this instant, delaminations facing towards impact and clamp zones at the top and bottom 0/90 interfaces, respectively, are distinguished. In the next frame corresponding to 371 μs , these delaminations are opened and clearly observed. 814 μs after the initial contact, a second matrix crack develops and delaminations are nucleated at both interfaces as seen in Figure 2.13b. Although the experiment is ideally symmetric with respect to impact line, neither the times of crack formation nor the failure pattern is not symmetric. This fact is given full consideration in the rest of the study.



(a)



(b)

(c)

Figure 2.13. UHSC pictures showing (a) the intact specimen, (b) formation of the major matrix cracks at the LHS and (c) formation of the single major matrix crack at the RHS of $[0_5/90_3]_s$ – Imp1 under 9.15 J impact.

Digital Image Correlation

Shear strain distributions on $[0/90]_s - \text{Imp2}$ prior to failure of the RHS of the specimen are obtained using DIC method and shown in Figure 2.14. The time interval between the sequential frames counts $1.43 \mu\text{s}$. In the frame taken at $386 \mu\text{s}$, high shear stresses in the range of $1000\text{-}2000 \mu\text{strain}$ exist along the middle 90° layers on both left and right-hand sides of the specimen. The largest absolute ϵ_{xy} zones ($>1500 \mu\text{strain}$) on the specimen at $400 \mu\text{s}$ are marked with white circles. It is observed that the matrix crack initiates from one of these high shear strain zones. Similar to the discussion made through the DIC analysis of static test results, it is deduced that formation of these ‘shear cracks’ are controlled by the shear component of the strain in case of these specimen and testing configurations.

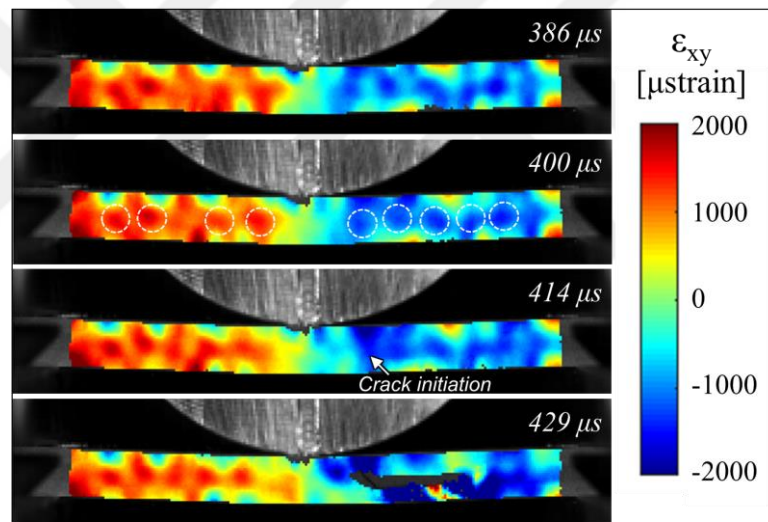


Figure 2.14. ϵ_{xy} distribution prior to failure on the $[0/90]_s - \text{Imp2}$ under 9.15 J impact loading . (The interframe time is $1.43 \mu\text{s}$ for the sequential frames)

Delamination Speeds

UHSC pictures of the evolution of the impact induced damage process in $[0_3/90_5]_s$ beam on the left half of specimen Imp3 taken at 525,000 fps are shown in Figure 2.15. Under a 9.15 J impact, initial damage mechanism is a diagonal matrix crack in the group of 90° plies and is shown inside the blue dashed circle in the first frame. This initial matrix crack forms about 17.5 mm away from the impact point, then it propagates in the 90° plies towards upper and lower 0/90 with an inclined angle. The instant it reaches upper and lower 0/90 interfaces at which delaminations initiate is taken as the reference time, $t = 0$ in Figure 2.15. From this point on, the delamination at the upper interface is followed and its tip is indicated with a blue arrow. The delamination at the lower 0/90 interface continues towards the left end. At $\Delta t = 7.6 \mu s$, a second matrix crack shown inside the red dashed circle in Figure 2.15 forms about 9.7 mm away from the loading line and induces a second delamination front at the upper 0/90 interface at $\Delta t = 11.4 \mu s$. At this instant, the first delamination tip is still behind, and the two separate delamination fronts are observed in the HSC pictures at $\Delta t = 11.4 \mu s$ and $\Delta t = 13.3 \mu s$. The two delaminations coalesce into one single large delamination at about $\Delta t = 15.2 \mu s$ and the secondary oblique matrix crack is closed and is no longer visible in the pictures. It should be noted that the secondary matrix crack is observed through the HSC pictures captured between $\Delta t = 5.7 \mu s$ and $\Delta t = 15.2 \mu s$ and it might not be observable for frame rates less than 100,000 fps. At $\Delta t = 26.6 \mu s$, the delamination front is seen underneath the impactor at a location very close to the impact line and arrests due to high out-of-plane compressive stresses causing crack closure under the impact zone.

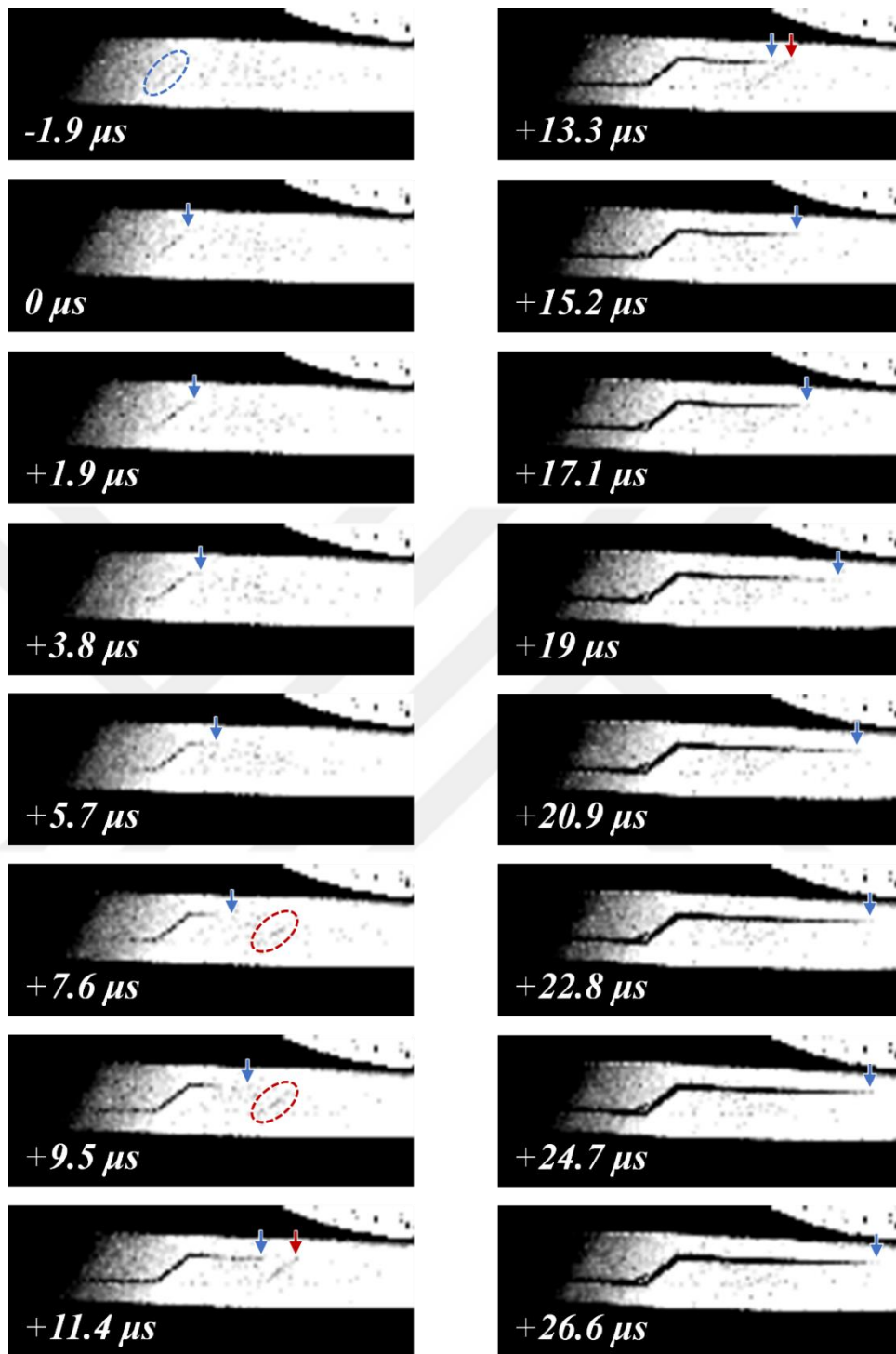


Figure 2.15. UHSC pictures showing the evolution of the impact induced damage on the left half of $[0_5/90_3]_s - \text{Imp3}$ taken at 525,000 fps. ($0 \mu\text{s}$ refers to the time of the picture in which a delamination front is seen for the first time)

The delamination crack tip positions as a function of time is shown in Figure 2.16a in comparison with the data obtained from static test. The crack tip position data used in this plot are extracted from the UHSC pictures shown in the Figure 2.15 and crack tip positions are measured from the middle of the beam where initial contact occurs. The time at which delamination initiates at the upper 0/90 interface is taken as $t = 0$, and the positions of initial and secondary delaminations are represented by blue and red markers, relatively, in accordance with Figure 2.15. Initial delamination forms approximately 16 mm away from the impact line, approaches with an increasing slope until $\Delta t = 7.6 \mu\text{s}$. Between $\Delta t = 7.6 \mu\text{s}$ and $\Delta t = 19 \mu\text{s}$, the delamination continues to propagate with a constant-like slope. At $\Delta t = 11.4 \mu\text{s}$, second delamination occurs 9 mm away from the impact line. The two delaminations merge at about $\Delta t = 15.2 \mu\text{s}$. After reaching the impact zone at about $\Delta t = 20.9 \mu\text{s}$, it slows down and is arrested while it is 2.8 mm away from the impact line at $\Delta t = 26.6 \mu\text{s}$. When the reference time for static test data is shifted to a larger value ($9 \mu\text{s}$) in order to eliminate the delay caused by the difference in the locations where crack initiates, a good correlation between the delamination propagation trajectories obtained in the static and 9.15 J impact tests is observed.

Variation of the delamination crack tip speeds with time is shown in Figure 2.16b. Velocities are calculated using three point numerical differentiation of the crack tip position with respect to time. After its initiation, the first delamination propagates with a speed of about 250 m/s approximately during the first 2 μs . Tip speed increases gradually up to 500 m/s and remains almost constant during the evolution of the second matrix crack (see Figure 2.15). The second delamination initiates about 11 μs later than the first one. During the first 2 μs , it propagates with a speed of 250 m/s like the first crack did after its initiation. In the meantime, the gradual increase of the crack tip speed of the first delamination recommences with the initiation of the second delamination, and it reaches approximately 830 m/s just before merging of the two cracks. Even though the two delaminations behave in a very similar way during the first 2 μs after their initiation, the tip speed of the second delamination increases more

sharply than that of the first one because of the merging. Upon merging, the tip speed of the coalesced crack is about 630 m/s and increases up to a maximum speed of 900 m/s at 19 μ s. After that, the coalesced crack starts to slow down and is arrested at about 26.7 μ s due to high compressive stresses in the impact zone. Results show that the variation and the maximum value of crack tip speeds are found to be consistent in the static and the 9.15 J impact tests.



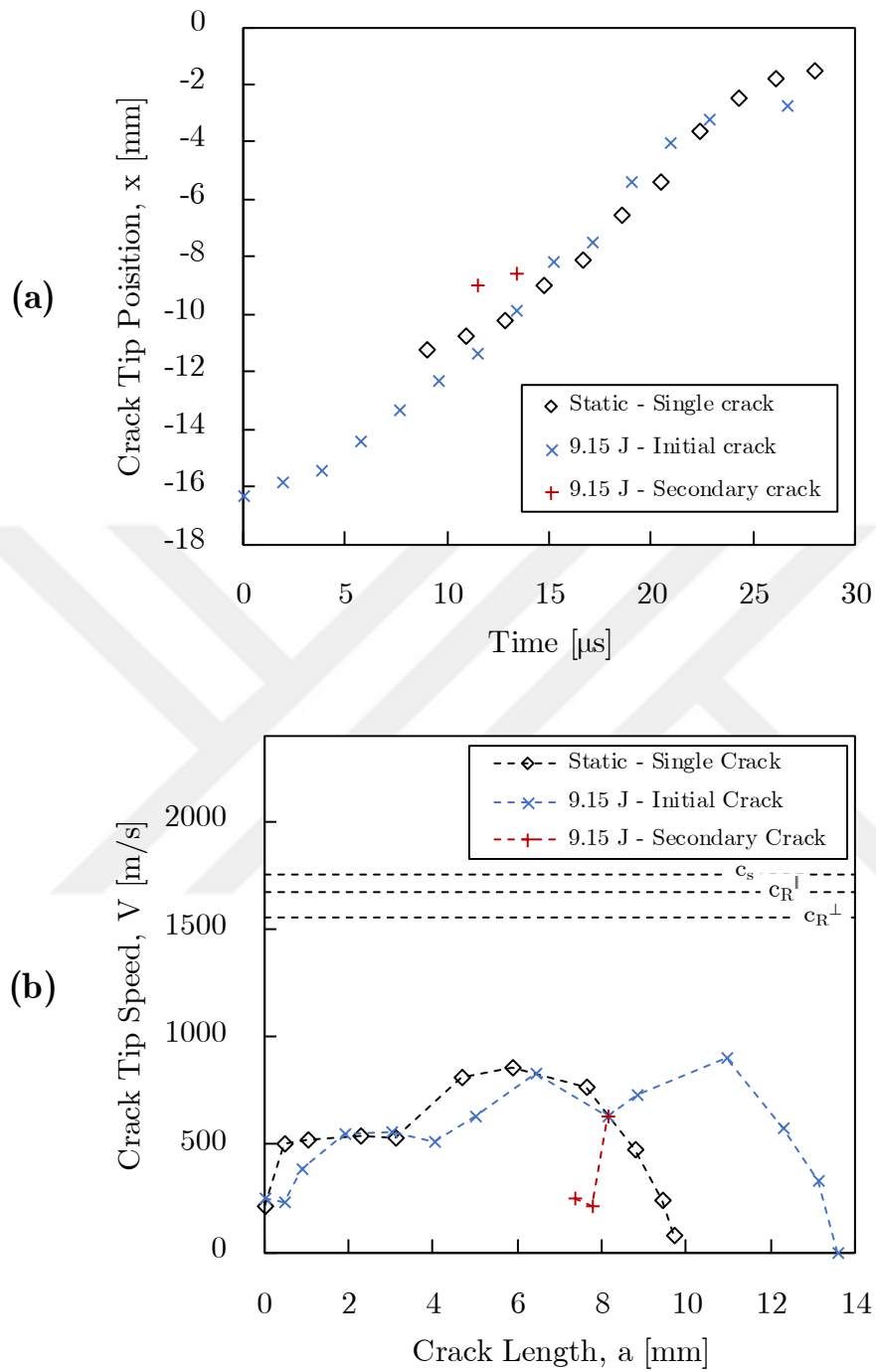


Figure 2.16. (a) Crack tip position vs. time and (b) crack tip speed vs. time graphs for the delamination at the top 0/90 interface.

Post-mortem Damage Characterization

Post-mortem micrographs of the $[0_5/90_3]_s$ – Imp1 shows the final damage pattern and it consists of matrix cracks and delaminations as shown in Figure 2.17. One major diagonal matrix crack is observed at the left side of the specimen and it intersects with the delaminations at upper and lower 0/90 interfaces. Branching of this matrix crack at the upper and lower ends can be seen from the close-up microscopy pictures. A debris is observed between the delaminated layers at the lower interface of this major diagonal matrix crack. There are two major diagonal matrix cracks at the right side of the specimen. Both of them intersect with delaminations at upper and lower 0/90 interfaces. Branching is observed at the lower end of the middle matrix crack.

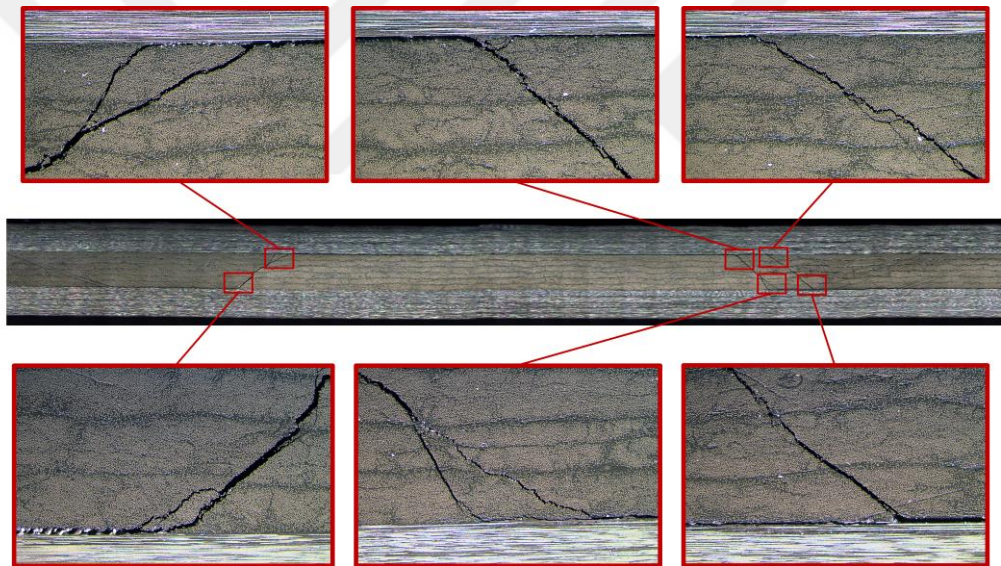


Figure 2.17. Post-mortem damage in the $[0_5/90_3]_s$ – Imp1 and close-up views of diagonal matrix cracks and delamination.

Final damage pattern of the $[0_5/90_3]_s$ – Imp3 is shown in Figure 2.18 and it contains matrix cracks and delaminations. One major diagonal matrix crack which intersects with the delaminations at upper and lower 0/90 interfaces is observed at the left side of the specimen. This matrix crack has branching at the lower end. Another major diagonal matrix crack is observed at the far-right end of the span which is connected

to the delaminations at upper and lower 0/90 interfaces. A micro-crack is observed near the right major diagonal matrix crack and it does not reach upper 0/90 interface unlike the major diagonal matrix cracks. Several micro-cracks which are intersecting with the delamination at the upper 0/90 interface are also observed and shown in yellow rectangles. These micro-cracks do not reach the lower 0/90 interface.

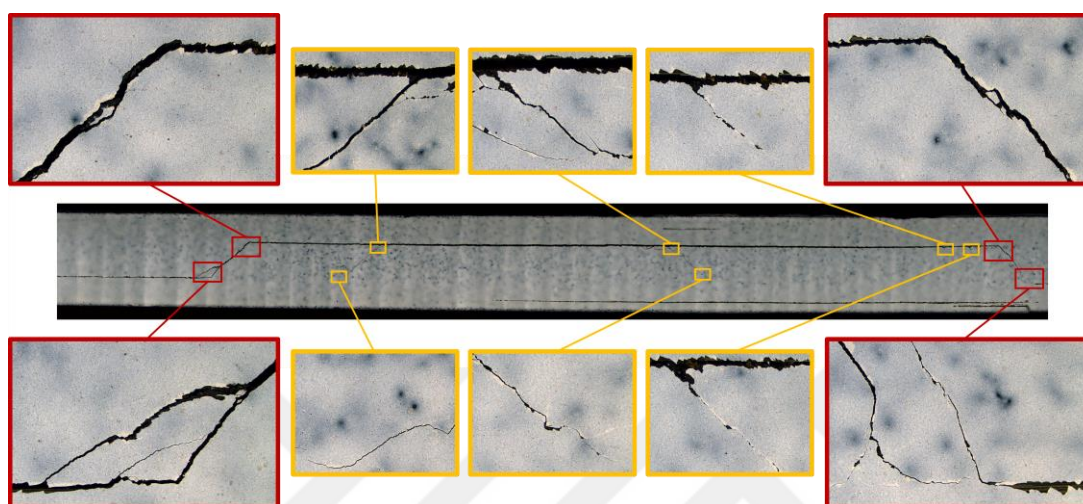


Figure 2.18. Post-mortem damage in the $[0_5/90_3]_s$ – Imp3 and close-up views of diagonal matrix cracks and micro-matrix cracks.

2.3.2. $[90/0]_s$ Specimens

2.3.2.1. Static Tests

Results of the static experiment of one $[90_5/0_3]_s$ specimen is presented in the following subsections.

In-situ Damage Characterization

Damage sequence in $[90_5/0_3]_s$ – Sta1 specimen under static loading is represented schematically in Figure 2.19. Damage initiates as a vertical matrix crack in the lower group of 90° layers at a location close to the impact line as shown in Figure 2.19a. This crack nucleates a delamination facing both left and right end sides of the specimen as secondary vertical matrix cracks. At the meantime, a vertical matrix crack is observed in the upper group of 90° layers near the left boundary condition, as shown

in Figure 2.19b. Then, a new delamination front is created where one of the secondary matrix cracks reaches the lower 0/90 interface. Two more matrix cracks form in the upper group of 90° layers near the right boundary condition. Delaminations are nucleated at the top 0/90 interface by each of the three matrix cracks developed in the upper 90° layers, as seen in Figure 2.19c. The formation of matrix cracks and the propagation of delaminations is observed to be much slower than those observed in the static tests of $[0_5/90_3]_s$ specimens. At the end of the test, a delamination occurs rapidly inside the middle clustered 0° plies, as seen in Figure 2.19d, in a form very similar to interlaminar shear.

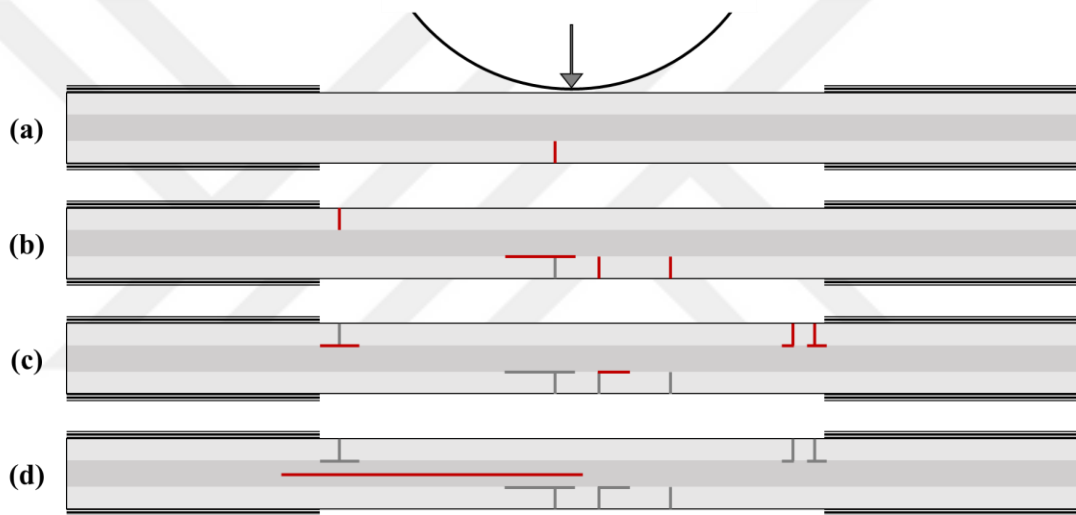


Figure 2.19. Schematic representation of damage formation sequence in $[90/0]_s$ – Sta1 under static loading.

Digital Image Correlation

ϵ_{xx} strain distribution before and damage state and after each local failure in the $[90_5/0_3]_s$ – Sta1 under static loading is presented in Figure 2.20a and b, respectively. Locations where matrix cracks occur are shown in red circles in Figure 2.20a. Corresponding cracks are marked with white circles and their close-up views are shown in Figure 2.20b. Results show that vertical matrix cracks occur where high

longitudinal tensile strains are observed. However, it is noted that not every hot ϵ_{xx} spots provoke a matrix crack.

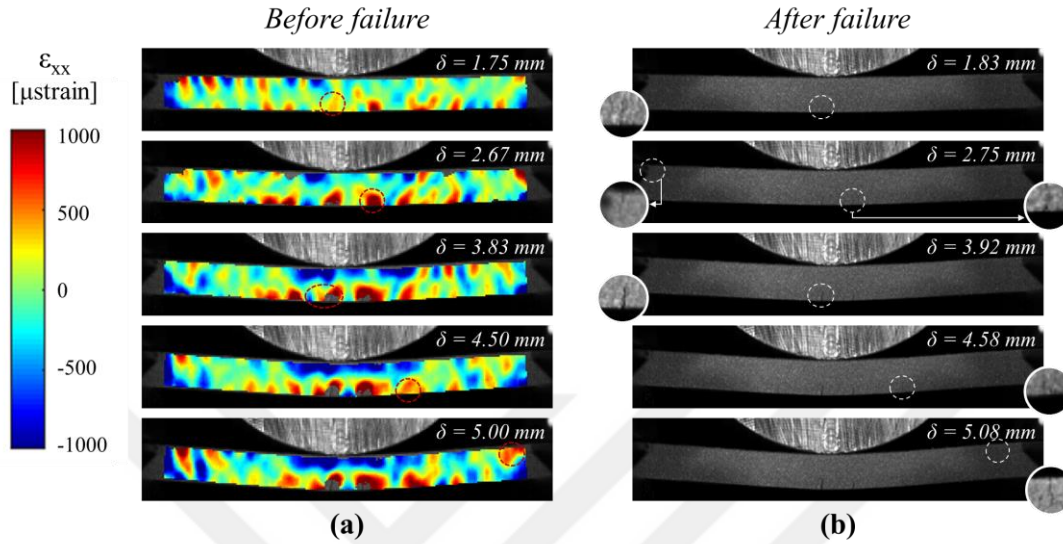


Figure 2.20. (a) ϵ_{xx} strain distribution before each local failure and (b) damage state after each local failure in the $[90_5/0_3]_s$ – Sta1 under static loading.

Post-mortem Damage Characterization

Micrographs in Figure 2.21 show the final damage pattern of $[90_5/0_3]_s$ – Sta1 consisting of matrix cracks and delaminations. All matrix cracks are observed to be vertical rather than diagonal as observed in the case of $[0_5/90_3]_s$ specimens. There are two matrix cracks in the bottom 90° layers near the half-span. A delamination exists where the left matrix crack reaches to the $0/90$ interface while no delamination is observed for the right matrix crack. In the top 90° layers, on the other hand, there are three matrix cracks two of which are located at each end of the span. Delaminations are observed around the intersection of these matrix cracks and top $0/90$ interface. The third matrix crack in the top 90° layers lies at the right side of the specimen without no delamination at its end. The lengths of these delaminations are smaller than the ones observed in $[0_5/90_3]_s$ specimens.

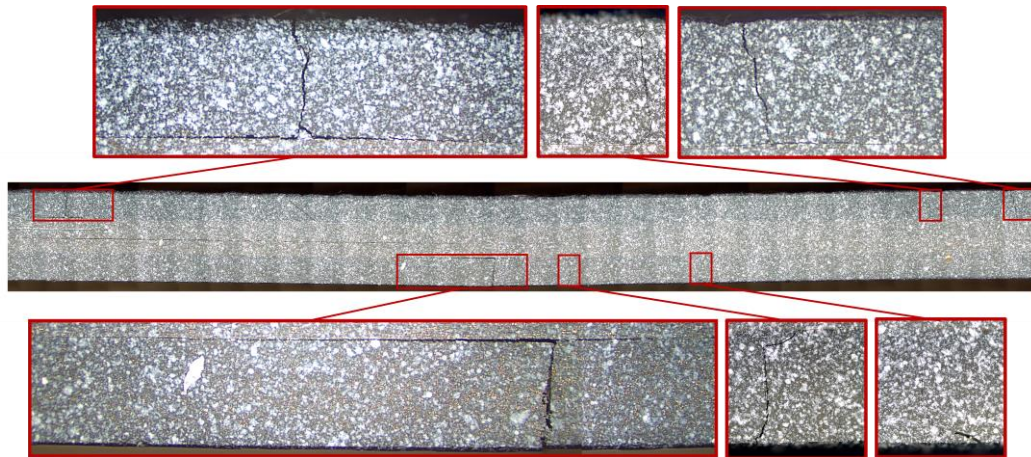


Figure 2.21. Post-mortem damage in the $[90_5/0_3]_s$ – Sta1 and close-up views of vertical matrix cracks and delaminations.

2.3.2.2. Impact Tests

Results of the impact experiment conducted on one $[90_5/0_3]_s$ specimen is presented in the following subsections.

In-situ Damage Characterization

In-situ formation of the damage induced by 7.32 J impact in $[90_5/0_3]_s$ – Imp1 is presented in Figure 2.22 via the UHSC pictures captured at 60,000 fps. Failure sequence is similar to that occurs in static tests. Initial failure is observed 217 μ s after the initial contact and it is in the form of a vertical matrix crack initiated near the middle of the bottom edge of the specimen where longitudinal stresses due to bending are higher. This crack is followed a vertical matrix crack which is observed at 250 μ s in the upper group of 90° layer near the left boundary condition. A secondary matrix crack occurs in the bottom 90° layers at 333 μ s. Finally, second matrix crack is observed at 733 μ s in the upper clustered 90° layers near the right boundary condition. The last frame in Figure 2.22 is taken at 1867 μ s which corresponds to the instant of maximum impactor displacement. The above-mentioned cracks which are shown in the yellow circles can be clearly observed in this frame since they are opened. Small amount of delaminations is also distinguished at the locations where these matrix

cracks meet the neighbor interfaces, but more detailed characterization of the delaminations are performed in the next section via micrographs of the post-mortem specimen.

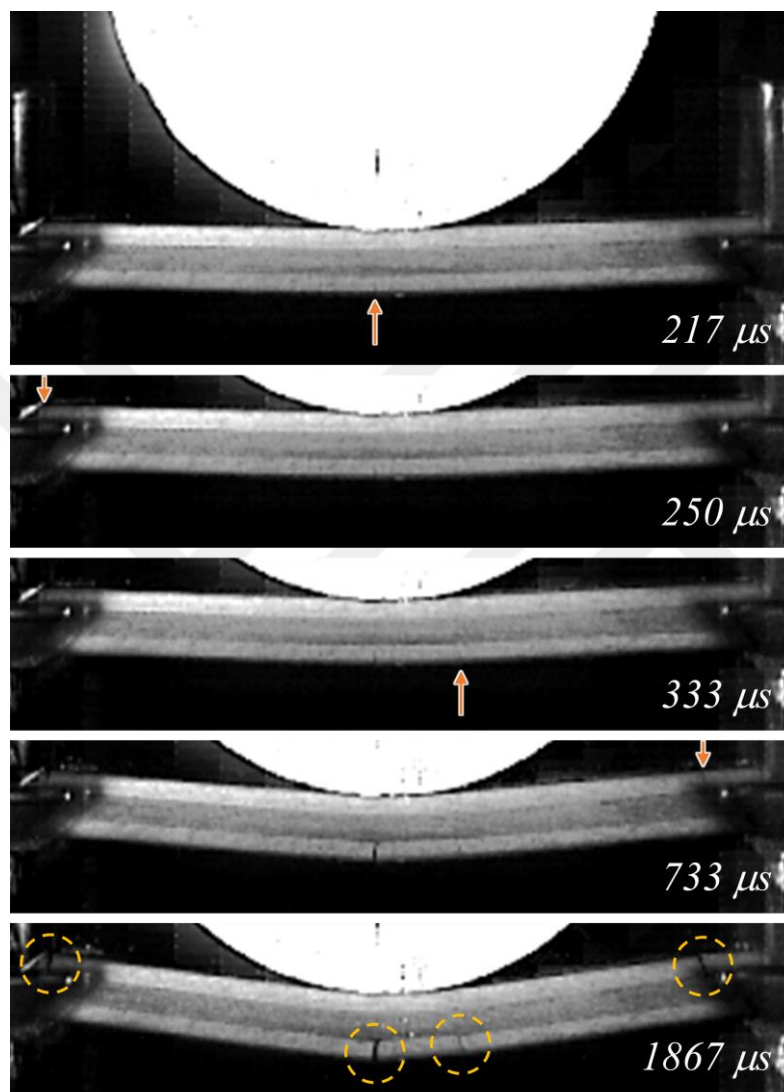


Figure 2.22. In-situ damage formation in $[90/0]_s$ – Imp1 under 7.32 J impact captured at 60,000 fps.

Post-mortem Damage Characterization

Post-mortem damage pattern of the $[90_5/0_3]_s$ – Imp1 includes the microscopy pictures of matrix cracks and delaminations, as shown in Figure 2.23. There are two vertical matrix cracks at each end of the span in the top 90° layers and delaminations are observed at the end of these matrix cracks, between the top 90° and 0° layers. Full-lengths of the delaminations are also shown in the close-up micrographs of the matrix cracks. A micro-crack is observed around the half span of the top 90° layer where the impactor hits, as shown in the yellow rectangle. In the bottom 90° layers, a delamination and two matrix cracks near the half-span are observed. The delamination is located at the $0/90$ interface and at the end of left matrix crack. There were no delaminations observed near the right matrix crack at the bottom 90° layer.

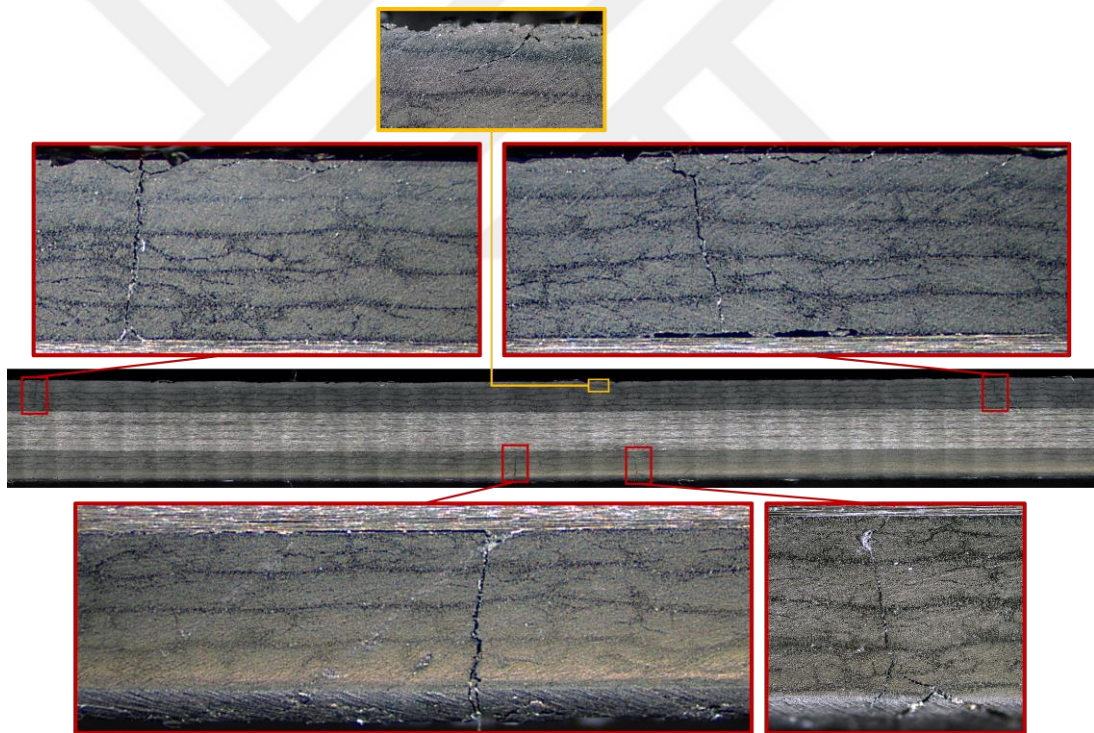


Figure 2.23. Post-mortem damage in the $[90_5/0_3]_s$ – Imp1 and close-up views of vertical matrix cracks and delamination.

2.4. Conclusions

In this study, static and low-velocity impact experiments are conducted on $[0/90]_s$ and $[90/0]_s$ CFRP beams. For this purpose, an in-house drop-weight type experimental setup is designed and manufactured. In the experiments, in-situ damage process is captured via ultra-high speed camera system. Strain fields on the specimen edge are obtained performing digital image correlation analyses. Post-mortem damage patterns are characterized using a digital microscope. The results of the experiments are presented in this section. Conclusions of the study are as follows:

In $[0/90]_s$ beams subjected to transverse static or impact loading,

- Initial failure mechanism is diagonal matrix crack formation followed by delaminations at the top and bottom 0/90 interfaces.
- Digital image correlation analysis show that transverse shear strain is the determinant component of the strain for formation of the diagonal matrix cracks.
- Micro-matrix cracks may occur in the middle group of 90° layers parallel to the initial diagonal crack.
- Experimental evidence of formation of a micro-matrix crack under impact loading is presented with an interframe time of $2 \mu\text{s}$. It is shown that the micro-matrix crack nucleates a new delamination front when it reaches the neighbor interface. At that instant, the front of the former delamination is still behind.
- Propagations of the delamination cracks in $[0/90]_s$ beams under static and impact loading are recorded with an interframe time of $2 \mu\text{s}$. The position of the delamination crack front is drawn with respect to time under static and impact loading. A good correlation is discovered between the delamination crack front trajectories in the static and the impact tests.
- Crack speeds in top 0/90 interface of $[0/90]_s$ beams are calculated under static and impact loadings performing numerical time differentiation of crack tip position data. In case of both static and dynamic loading, crack speed raises up

to 850 m/s. It is inferred from this observation that, under both static and dynamic flexural loading, dynamic crack propagation occurs in $[0/90]_s$ CFRP beams.

- Finally, the experimental data consisting of the crack tip positions and the crack tip speeds can be used as a benchmark for the simulations of the experiments conducted on $[0/90]_s$ beams.

In $[90/0]_s$ beams subjected to transverse static or impact loading,

- Initial failure mechanism is vertical matrix crack formation around the maximum bending stress location in the bottom 90° group of layers.
- Digital image correlation analysis shows that formation of vertical matrix cracks occurs where longitudinal strain concentrations are observed.
- Although vertical matrix cracks nucleate delaminations at their neighboring interfaces in $[90/0]_s$ beams, sizes and propagation speeds of these delaminations are significantly small compared to that observed in $[0/90]_s$ beams.



CHAPTER 3

NUMERICAL INVESTIGATION OF LOW-VELOCITY IMPACT DAMAGE IN FIBER-REINFORCED COMPOSITE BEAMS

3.1. Introduction

In this study, finite element simulations of the line impact experiments conducted on cross-ply CFRP specimens are presented. Impact tests of composite beams are modeled in 3-D space. Low-velocity impact simulations are conducted with explicit finite element analysis. In order to predict composite ply damage, intralaminar damage model which is developed and implemented to ABAQUS/Explicit via a user-written subroutine VUMAT in a previous study [9] is used. Delamination damage is simulated using cohesive zone method. Initiation times and locations of damages and final damage patterns are investigated comparing the results obtained in simulations with experimental results.

3.2. Numerical Method

Simulation technique and damage models used in the finite element model analysis are presented in this section. Although the line impact model can be simplified into a two-dimensional model, finite element model is created using ABAQUS/Explicit in 3D environment to investigate contribution of 3D effects observed in the real experiments. Intralaminar and interlaminar damage models are developed and implemented to the analysis for simulating damage process in $[0_5/90_3]_s$ CFRP beam under LVI.

3.2.1. Modelling of Composite Damage

Two separate damage models are used for simulation of composite ply damage and delamination: intralaminar and interlaminar, respectively. These two damage models are described in the following subsections.

3.2.1.1. Intralaminar Damage Model

In this study, LaRC04 failure criteria is used to determine the damage initiation at composite ply level. Together with failure criteria, bilinear equivalent stress-displacement response of 3-D solid elements constitutes the continuum damage mechanics based three-dimensional composite damage model. Intralaminar damage model is implemented to the finite element model via an ABAQUS/Explicit user-written material subroutine VUMAT which is developed in a previous study [9].

Damage Initiation

Although prediction of fiber and matrix damage initiations are made separately in LaRC04 failure criteria [15], this study includes only matrix failure criterion in agreement with the experiments. Equations predicting the initiation of matrix damage for the current state of the normal stress in the in-plane transverse direction, σ_{22} , are given as follows:

Tensile matrix failure for $\sigma_{22} > 0$,

$$FI^T = (1 - g) \frac{\sigma_{22}}{Y_{is}^T} + g \left(\frac{\sigma_{22}}{Y_{is}^T} \right)^2 + \frac{\Lambda_{23}^o \tau_{23}^2 + \chi(\gamma_{12})}{\chi(\gamma_{12is}^u)} = 1 \quad (3.1)$$

In equation (3.1), toughness ratio g is defined as the ratio of mode I and mode II fracture toughness terms and adds in-plane shear non-linearity. Λ_{23}^o is the transverse shear component of crack tensor and in-plane shear internal energy $\chi(\gamma_{12})$ is the area swept by in-plane shear stress-strain curve. As the middle 90° layer is a thick embedded ply in the laminate ($t = 1.8 \text{ mm} > 0.8 \text{ mm}$), in-situ values of transverse

tensile strength Y_{is}^T and ultimate in-plane shear strain γ_{12is}^u are used in prediction of tensile matrix damage. In-situ tensile strength Y_{is}^T is calculated as $1.12\sqrt{2} Y^T$ [15].

Compressive matrix failure for $\sigma_{22} < 0$,

$$FIC = \left(\frac{\tau^T}{S^T - \eta^T \sigma_n} \right)^2 + \left(\frac{\tau^L}{S_{is}^L - \eta^L \sigma_n} \right)^2 = 1 \quad (3.2)$$

In equation (3.2), τ^L and τ^T are shear tractions on the fracture plane along and transverse to fiber directions, respectively and σ_n is the normal traction as expressed in Mohr-Coulomb criterion. $\eta^T \sigma_n$ and $\eta^L \sigma_n$ are shear stresses on the fracture plane due to friction. In-situ longitudinal shear strength S_{is}^L is defined as $S_{is}^L = \sqrt{2} S^L$ for linear shear law of a thick embedded ply [27], [28]. S^T is the shear strength transverse to the fibers and calculated from compressive transverse strength Y^C and α_o which is the angle of the fracture plane with vertical in pure transverse compression. Although α_o depends on the loading, experiments show that $\alpha_o = 53 \pm 2^\circ$ for most technical composite materials [15].

Damage evolution

After the initiation of damage in tensile or compressive mode, linear softening response shown in Figure 3.1 represents the propagation of damage. The linear softening response for a damaged composite ply is adapted from the model proposed originally for cohesive materials [29].

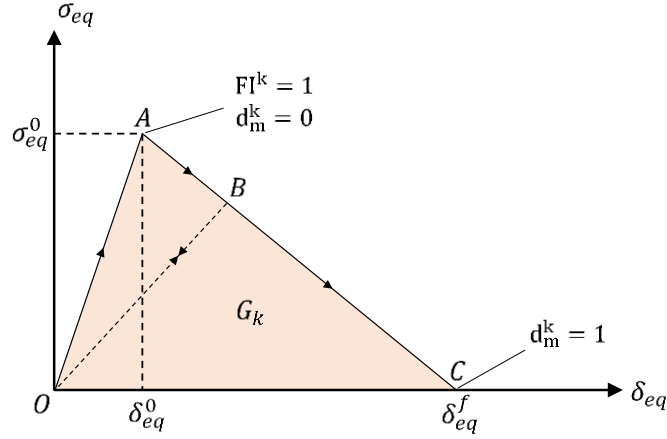


Figure 3.1. Constitutive bilinear stress – displacement response for intralaminar damage model.

In Figure 3.1, O-A line represents the loading of the solid element until damage initiation. A is the point where failure index for tensile or compressive mode FI^k ($k = T, C$) reaches 1, indicating failure initiation. At this point, matrix damage metric d_m^k is 0. On A-C line, damage propagates and d_m^k increases from 0 to 1, following non-linear saturation type behavior specified as

$$d_m^k = \frac{\delta_{eq,k}^f (\delta_{eq} - \delta_{eq,k}^0)}{\delta_{eq} (\delta_{eq,k}^f - \delta_{eq,k}^0)} \quad (3.3)$$

At point C, element is completely damaged. When unloading occurs from a partially damaged state, B-O line is followed. The area under OAC curve G_k is described as energy dissipation until complete failure. For tensile matrix failure, G_T is equivalent to mode I fracture toughness G_{Ic} of material, where G_C can be calculated approximately using mode II fracture toughness G_{IIc} and fracture angle α_0 in case of compressive matrix damage and defined as $G_C = G_{IIc} / \cos(\alpha_0)$ [25]. Equivalent stress σ_{eq} and equivalent displacement δ_{eq} expressions defined for 3-D stress state are given as [9]

$$\sigma_{eq} = \frac{\langle \pm \sigma_{22} \rangle \langle \pm \varepsilon_{22} \rangle + \langle \pm \sigma_{33} \rangle \langle \pm \varepsilon_{33} \rangle + \tau_{12} \varepsilon_{12} + \tau_{13} \varepsilon_{13} + \tau_{23} \varepsilon_{23}}{\delta_{eq}/l^*} \quad (3.4)$$

$$\delta_{eq} = l^* \sqrt{\langle \pm \varepsilon_{22} \rangle^2 + \langle \pm \varepsilon_{33} \rangle^2 + \varepsilon_{12}^2 + \varepsilon_{13}^2 + \varepsilon_{23}^2} \quad (3.5)$$

The “ \pm ” sign is taken as “+” for tensile failure mode and “-” for compressive failure mode in equations (3.4) and (3.5). l^* is the characteristic length of each element defined to reduce the mesh dependency of finite element model and $\langle \rangle$ is the Macaulay bracket, which is defined as $\langle a \rangle = (a + |a|)/2$. It should be noted that $\sigma_{eq,k}^0$ and $\delta_{eq,k}^0$ refer to equivalent stress and equivalent displacement calculated from stress and strain state when FI^k becomes 1. The final equivalent displacement $\delta_{eq,k}^f$ where complete damage happens is found as $2G_k/\sigma_{eq,k}^0$.

For representing degradation of in-plane stiffness properties, damaged stiffness matrix approach is proposed by Matzenmiller [19]. Extended version of damaged compliance matrix to 3-D is given as follows considering only matrix damage [30]

$$S = \begin{bmatrix} \frac{1}{E_1} & -\frac{\nu_{12}}{E_1} & -\frac{\nu_{13}}{E_1} & 0 & 0 & 0 \\ -\frac{\nu_{12}}{E_1} & \frac{1}{E_2(1-d_M)} & -\frac{\nu_{23}}{E_2} & 0 & 0 & 0 \\ -\frac{\nu_{13}}{E_1} & -\frac{\nu_{23}}{E_2} & \frac{1}{E_3(1-d_M)} & 0 & 0 & 0 \\ 0 & 0 & 0 & \frac{1}{2G_{12}(1-d_S)} & 0 & 0 \\ 0 & 0 & 0 & 0 & \frac{1}{2G_{13}(1-d_S)} & 0 \\ 0 & 0 & 0 & 0 & 0 & \frac{1}{2G_{23}(1-d_S)} \end{bmatrix} \quad (3.6)$$

In equation (3.6), d_m and d_s are matrix and shear damage metrics, respectively. Matrix damage metric is determined according to type of the loading. For tensile matrix damage mode, i.e. $\sigma_{22} > 0$, $d_m = d_m^T$ and for compressive mode where $\sigma_{22} < 0$, $d_m = d_m^C$. Shear damage metric is defined as a combination of compressive and

tensile mode damage metrics and calculated as $d_s = 1 - (1 - d_m^T)(1 - d_m^C)$. After degradation, stress state is redefined by $\sigma = C\varepsilon$, where stiffness matrix C is the inverse of the compliance matrix S .

3.2.1.2. Interlaminar Damage Model

Cohesive zone method of is used for simulating delamination along 0/90 interfaces. Similar to intralaminar damage model, a bilinear traction – separation response is defined for cohesive elements. Effect of mode-mixity under multiaxial loading conditions is taken into account by superposition of responses in normal and shear directions, as shown in Figure 3.2.

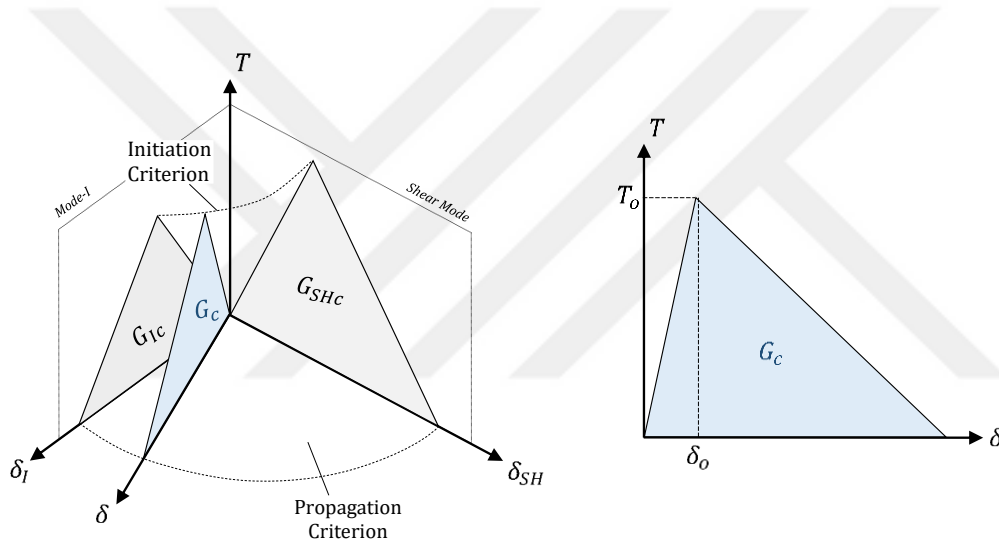


Figure 3.2. Constitutive traction – separation law for cohesive zone model in mixed-mode

Damage Initiation

For a single mode loading case, the initial response of the cohesive elements is assumed linear. The slope of the initial linear portion of the bilinear curve is known as penalty stiffness E_o and it is assumed a high value to prevent unphysical compliance prior to onset of delamination [9]. Damage initiation occurs at the state where the surface tractions at cohesive interfaces increase linearly and reach the interfacial

strength of the corresponding mode, $T_{o,i}$, $i = I, II, III$. Quadratic nominal stress criterion which is used to determine initiation of damage in vicinity of mode-mixity is given as

$$\left(\frac{\langle T_I \rangle}{T_{o,I}}\right)^2 + \left(\frac{T_{II}}{T_{o,II}}\right)^2 + \left(\frac{T_{III}}{T_{o,III}}\right)^2 = 1 \quad (3.7)$$

Since compressive stresses are assumed to generate no damage on cohesive elements, Macaulay operator is applied on opening mode surface traction T_I in the damage initiation criterion. Mixed mode separation value at damage initiation is expressed as

$$\delta_o = T_o/E_o \text{ where initiation traction is } T_o = \sqrt{T_{o,I}^2 + T_{o,II}^2 + T_{o,III}^2}.$$

Damage Evolution

Once the damage initiates in cohesive element, linear softening of traction-separation response starts in which tractions decrease to zero at each critical pure mode displacement $\delta_{c,i}$, $i = I, II, III$. The area under each pure mode traction-separation curve refers to the fracture toughness of corresponding mode, G_{ic} . The pure mode critical displacements can be found by $\delta_{c,i} = 2G_{ic}/T_{o,i}$.

Mode-mixity in damage propagation is taken into account in calculation of critical energy release rate, G_c , under a mixed-mode loading case. G_c is defined by Benzeggagh-Kenane criterion which is given as [32]

$$G_c = G_{Ic} + (G_{SHc} - G_{Ic}) \left(\frac{G_{SH}}{G_T}\right)^\eta \quad (3.8)$$

In equation (3.8), G_{SH} and G_T refer to sum of work done by shear mode tractions and sum of all pure mode tractions, respectively, on corresponding single mode displacements, implying that $G_{SH} = G_{II} + G_{III}$ and $G_T = G_I + G_{II} + G_{III}$. G_{Ic} is the fracture toughness in pure opening mode. Critical energy release rates of shear mode cracks in first and second directions G_{IIc} and G_{IIIc} are assumed equal and shear mode

fracture toughness G_{SHc} is defined accordingly as $G_{SHc} = G_{IIc} = G_{IIIc}$. B-K criterion constant η is a non-dimensional curve fitting parameter which is obtained from mixed-mode fracture toughness test [33].

During the evolution of mixed-mode damage in cohesive elements, in order to provide a linear softening response to interface elements, damage metric D is defined as

$$D = \frac{\delta_c(\delta - \delta_o)}{\delta(\delta_c - \delta_o)} \quad (3.9)$$

where effective mixed-mode separation is calculated with $\delta = \sqrt{(\delta_I)^2 + \delta_{II}^2 + \delta_{III}^2}$ and its critical value is determined by $\delta_c = 2G_c/T_o$.

3.2.2. Finite Element Model

Low-velocity impact experiments conducted in Chapter 2 are simulated with explicit finite element analyses. A three-dimensional model is generated in ABAQUS/Explicit to include nonlinearities due to 3-D effects. In this section, geometry and boundary conditions of finite element model, ply and interface properties of the composite material, mesh and element size specified for discretization of beam geometry and contact and friction models used in the simulations are discussed.

3.2.2.1. Geometry and Boundary Conditions

In the general finite element model, impactor and beam geometries are created. Dimensions of parts are shown in Figure 3.3 together with initial and boundary conditions.

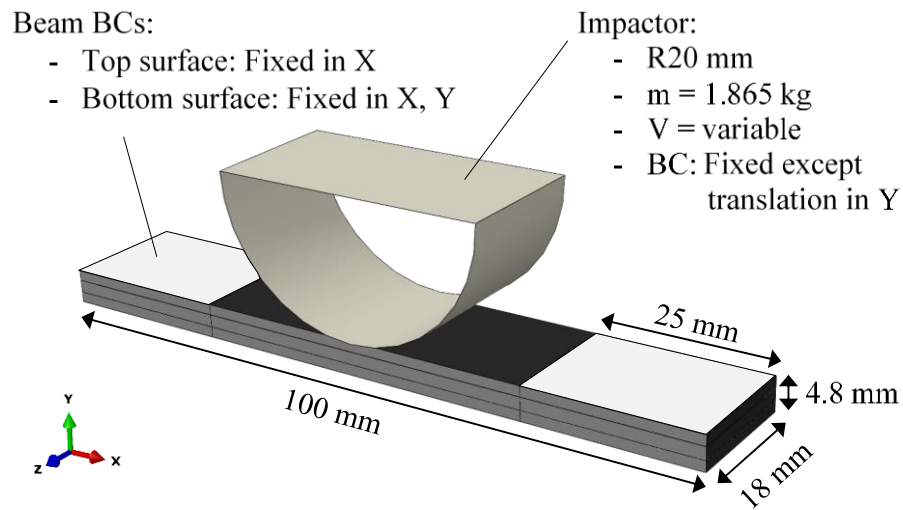


Figure 3.3. Geometry, initial conditions and boundary conditions of the line impact finite element model.

Steel impactor is modeled as an analytical rigid body with a lumped mass of 1.865 kg. In order to conduct virtual experiments with an impact energy corresponding to different release height, an initial velocity in downward direction is calculated and predefined to the impactor body. Lateral translational motions and all rotational motions of the impactor are restrained.

The $100 \times 17 \times 4.8 \text{ mm}^3$ composite beam is modeled as a 3-D deformable solid body at mesoscale. The beam consists of 16 unidirectional composite layers having equal thicknesses of 0.3 mm. In the model, clustered plies are considered as a single homogenized thick ply. Boundary conditions are defined on top and bottom surfaces at $25 \times 18 \text{ mm}^2$ end regions of the beam. In order to simulate experimental conditions as closely as possible, translation of bottom surface is constrained X and Y directions while the top surface is fixed only in X direction to allow the shape change due to Poisson effect under compressive loading.

In some of the analyses, more detailed model of the experiments is used since required. In this model, clamps are also modeled as rigid bodies for better representation of the experimental boundary conditions. The clamps squeeze the beam through an out-of-

plane displacement of 0.005 mm which is defined to the reference nodes assigned to each clamp. A resultant clamping force of 3200 N is obtained on both end of the beams.

3.2.2.2. Material Properties

Ply level mechanical properties of Hexcel 913C/HTS unidirectional tape material are given in Table 3.1. Elastic properties including longitudinal, in-plane transverse, in-plane shear, out-of-plane shear moduli and in-plane and out-of-plane Poisson's ratios ($E_1, E_2, G_{12}, G_{23}, \nu_{12}, \nu_{23}$), strength properties such as transverse tensile, transverse compression and in-plane shear strengths (Y^T, Y^C, S^L) and density value (ρ) are taken from [9]. The remaining material properties E_3, G_{13} and ν_{13} are assumed as: $E_3 = E_2, G_{13} = G_{12}, \nu_{13} = \nu_{12}$ in accordance with [9].

Table 3.1. Mechanical properties of Hexcel 913C/HTS.

Density	1780 kg/m ³
Elastic	$E_1 = 135$ GPa; $E_2 = 9.6$ GPa; $E_3 = 9.6$ GPa $\nu_{12} = 0.3$; $\nu_{13} = 0.3$; $\nu_{23} = 0.45$ $G_{12} = 5.5$ GPa; $G_{13} = 5.5$ GPa; $G_{23} = 4.5$ GPa
Strength	$Y_T = 60$ MPa; $Y_C = 205$ MPa $S_{I2} = 62$ MPa; $S_{I3} = 62$ MPa

Interface properties of Hexcel 913C/HTS material are specified in Table 3.2. Interface strengths $T_{o,I}$ and $T_{o,II}$ are determined from ASTM Standards D6415 [34] and D2344 [35], respectively, and $T_{o,III}$ is take to be equal to the $T_{o,II}$. DCB [36] and ENF [37] tests are conducted for measuring Mode-I and Mode-II fracture toughnesses G_{Ic} and G_{IIc} . G_{IIIc} is assumed as $G_{IIIc} = G_{IIc}$. B-K criterion constant is taken as 1.45 which is designated for a similar material [7]. As mentioned in the description of the

interlaminar damage model, penalty stiffness E_o is assumed a high value to prevent unphysical compliance prior to onset of delamination [9].

Table 3.2. Interface properties of Hexcel 913C/HTS

Interface strength	$T_{o,I} = T_{o,II} = T_{o,III} = 115 \text{ MPa}$
Fracture toughness	$G_{I,c} = 280 \text{ N/m}; G_{II,c} = G_{III,c} = 860 \text{ N/m}$
B-K criterion constant	$\eta = 1.45$
Penalty stiffness	$E_o = 5 \times 10^{14} \text{ N/m}^3$

3.2.2.3. Mesh and Element Size

In the finite element model, each composite layer of the beam is modeled with one solid element in thickness direction as in most studies performed at mesoscale [3], [6], [7], [9]. 8-noded linear brick elements with reduced integration and hourglass control (C3D8R) are used to discretize composite beam and the resultant size of each solid element is $0.2 \times 0.2 \times 0.3 \text{ mm}^3$. Interface elements are offset from the solid mesh between the layers of different fiber angle and an offset thickness of zero is specified such that FE software assigns the smallest possible thickness to interface elements. Each cohesive element shares the nodes with upper surface nodes of top adjacent element and lower surface nodes of bottom adjacent element.

Mesh stability criteria proposed by Yang and Cox [38] is checked for interface elements. The cohesive zone length is determined by $l_{cz,I} = (l_{ch,I})^{1/4} h^{3/4}$ and $l_{cz,II} = \sqrt{l_{ch,II} h}$ for Mode-I and Mode-II delaminations in slender beams. In these expressions, h is the laminate half thickness and $l_{ch,i}$ is the characteristic length of cohesive material for failure modes $i = I, II$ where $l_{ch,i} = G_{ic} E' / T_{o,i}^2$ with G_{ic} , E' and $T_{o,i}$ being fracture toughness, equivalent elastic modulus and interfacial strength. The greatest element length $l_e = 0.2 \text{ mm}$ is compared with cohesive zone lengths $l_{cz,i}$ for Mode-I

and Mode-II failures and it is established that cohesive zone length is spread on a dozen of cohesive elements. It is noted that equivalent elastic modulus of an orthotropic material is defined as $E' = E_1\sqrt{1 - \nu_{12}\nu_{21}}$.

In order to prevent constitutive linear softening of damaged elements with strain reduction, greatest in-plane element size in the model, l^* , should be less than the maximum characteristic in-plane element length l_{max}^* which is determined by $l_{max,M}^* = 2E_M G_M / X_M^2$ where E_M, G_M and X_M are elastic modulus, fracture toughness and ply strength with $M = 2+, 2-, 6$ corresponding to tensile matrix, compressive matrix and shear failure modes [26]. In calculation of l_{max}^* , it is assumed that $E_{2+} = E_{2-} = E_2, E_6 = G_{12}, G_{2+} = G_{Ic}, G_{2-} = G_{IIc} / \cos(53^\circ), G_6 = G_{IIc}, X_{2+} = Y^T, X_{2-} = Y^C$ and $X_6 = S^L$ [4]. The minimum of maximum greatest element sizes is found at compressive matrix direction as $l_{max,2-}^* \approx 0.64$ mm which is approximately 2.3 times larger than greatest in-plane element size in the model, $l^* = \sqrt{l_x l_y} \approx 0.28$ mm.

3.2.2.4. Contact and Friction Models

Contact between the impactor and the beam laminate is modeled by *General Contact Algorithm* of ABAQUS/Explicit. Kinematic and penalty enforcement contact methods are used for normal and tangential behaviors, respectively. This contact model is also applied at possible delaminated interfaces for simulating contact and friction where cohesive elements are fully damaged and removed from the analysis.

Penalty contact method in ABAQUS/Explicit uses Coulomb Friction model. In the Coulomb model, relative tangential motion between two contacted surfaces is restricted until a critical surface traction value, $\tau_c = \mu p$, is reached where μ is the friction coefficient and p is the normal contact pressure at the corresponding surface. In the current model, following the studies of several authors [3], [7], $\mu = 0.3$ for impactor-laminate contact and $\mu = 0.5$ for internal laminate contact is used.

In addition to the above-mentioned contact definitions, contact between the rigid clamps and the beam is defined in the detailed finite element model. Similarly,

kinematic and penalty enforcement contact methods are used for normal and tangential behaviors, respectively. $\mu = 0.3$ is used for clamp-laminate contact.

3.3. Numerical Results

In this section, results of the finite element analyses conducted in ABAQUS/Explicit for simulating the low-velocity impact experiments on $[0_5/90_3]_s$ and $[90_5/0_3]_s$ CFRP beams are presented.

3.3.1. $[0_5/90_3]_s$ Beams

In-situ Damage Process

Finite element analysis of the 9.15 J impact on the $[0_5/90_3]_s$ CFRP composite beam is conducted. Damage formation sequence in the beam is seen in Figure 3.4 through eight consecutive pictures of the beam snapped with a time interval of 1 μ s. This sequence is summarized as follows:

- At 322 μ s after the initial contact between the impactor and the beam, initiation of matrix damage inside the clustered 90° plies is observed on both side of the beam laminate.
- These matrix damages grow towards the interfaces with an inclined angle and form diagonal matrix cracks at 324 μ s. At this instant formation of new matrix damages is observed at locations closer to the impact line.
- At 326 μ s, delaminations which are nucleated by the diagonal matrix cracks when reaching the upper and the bottom $0/90$ interfaces are seen. It is also observed that secondary diagonal matrix cracks are developed towards the midspan of the beam.
- At 328 μ s, growth of the existent delaminations are noted and new delamination fronts are created by secondary matrix cracks.
- On each side of the beam, the two delaminations at the top $0/90$ interface coalesces and form a single delamination at 330 μ s.

- At 332 μs , delaminations propagates towards midspan of the beam at the top 0/90 interface and towards ends of the beam at the bottom 0/90 interface.
- At 334 μs , two delaminations propagating at the 0/90 interface are observed to be merged into one large delamination at the middle of the beam.
- Final damage pattern in the beam is captured at 350 μs .

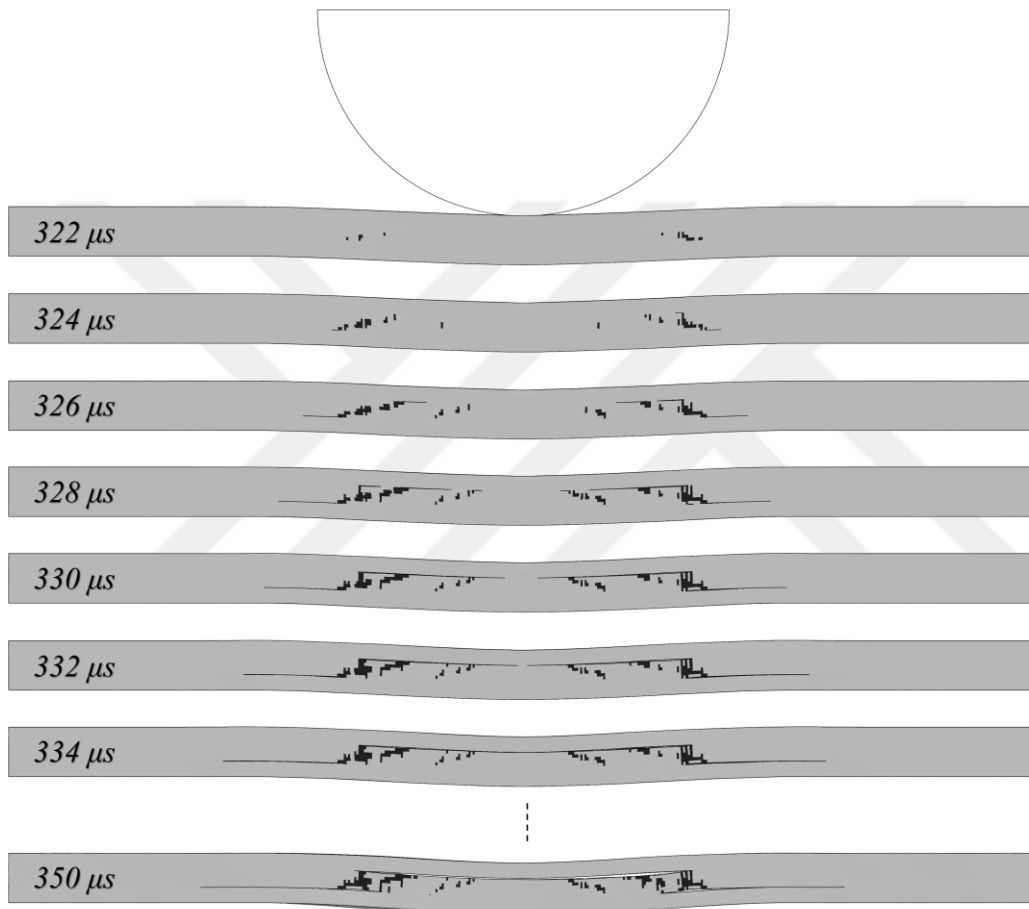


Figure 3.4. Damage formation sequence in the $[0_5/90_3]_s$ CFRP beam subjected to 9.15 J impact.

Figure 3.5 shows the matrix damage observed in the simulation and the experiment. The result show that a good agreement between the experiment and the simulation is achieved in terms of form, initiation location and initiation time of matrix cracks.

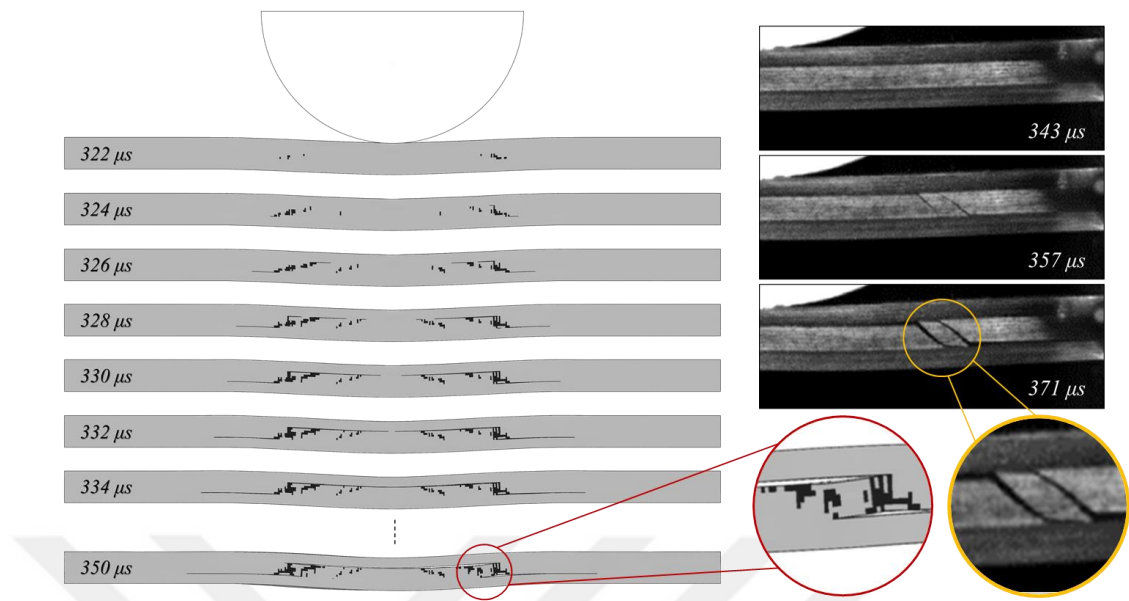


Figure 3.5. Comparison of the diagonal matrix damage observed in the simulation (left) and the experiment (right).

The results of this finite element analysis show that modeling the geometry in three-dimensional space highly affects both interlaminar and intralaminar damage formation sequences. Damage progression inside the beam is visualized via translucent images presented in Figure 3.6. It is seen that initial matrix cracks initiate at the free edges of the beam and propagate towards middle of the beam inside the clustered 90° layers. Concurrently, secondary cracks form at the free edge and then grow similarly with a time lag. Further propagation of matrix cracks generates a non-uniform complex 3D damage pattern.

Delamination formation sequence along the width of the specimen at the upper $0/90$ interface is also seen in the Figure 3.6. It is observed that delaminations initiate at the free edges of the beam where the matrix cracks touch the interfaces at $324 \mu\text{s}$. Delaminations at the top $0/90$ interface propagate towards middle of the beam in both length and depth directions until they merge completely at $334 \mu\text{s}$. Delaminations at the bottom $0/90$ interface, on the other hand, expand towards the end of the beams in length direction and to the inside the beam in depth direction. At $330 \mu\text{s}$, delamination

fronts formed at the front and back faces of the beam meets in depth direction turn into a single delamination at each of four delaminated regions namely top-left, top-right, bottom-left and bottom-right delaminations.

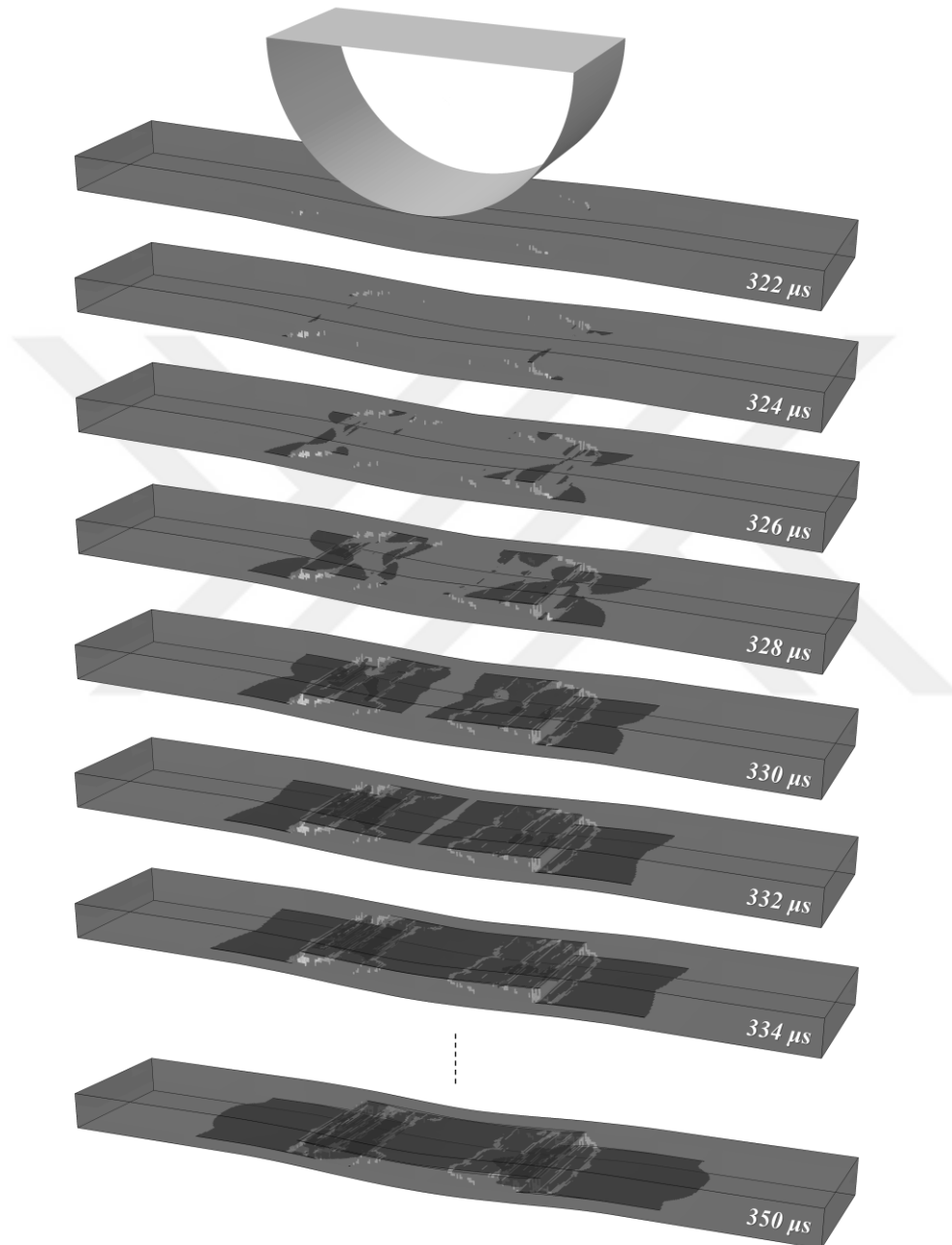


Figure 3.6. Matrix and delaminations damage progression inside the $[0_5/90_3]_s$ CFRP beam visualized via translucent images.

Matrix Crack Initiation and Microcrack Formation Mechanisms

In the impact event of $[0/90]_s$ beams, initial damage occurs in the clustered 90° plies. Initiation of the matrix damage in the beam under 7.7 J impact is investigated using the shear stress contours drawn in the regions under transverse tension. Figure 3.7 shows the sequence of tensile matrix damage formation in 90° plies together with the pioneer transverse shear stress (τ_{23}) contours observed on the elements under tension stress through the length of the beam only. At 230 μs after initial contact between impactor and top surface of the beam, first and major matrix crack forms at a region where shear stresses are maximum. The angle made by this crack and the longitudinal direction is approximately 45° and this corresponds to the angle of the inclination of the principal stress plane which is the common case under shear stress dominance. When the major matrix crack reaches the top and bottom 0/90 interfaces, delamination fronts arise. Although shear stresses are amplified around the matrix crack induced delamination crack tip, no further matrix crack formation is observed in these regions where normal stresses in length of the beam direction are compressive due to the compressive waves spread from sudden breakage location of 90° clustered plies in tension loading. At 231 μs , a secondary matrix crack, which is also called a microcrack, initiates in tensile matrix mode at maximum transverse shear stress location at a distance from major matrix crack. Later a second microcrack occurs in a similar way at a location closer to the impact region, at approximately 232 μs . The angle between microcracks and horizontal are nearly same as the angle made by major matrix crack due to similar shear dominance. At 235 μs after initial contact, it is seen that each microcrack nucleates a new delamination front when they reach the interface.

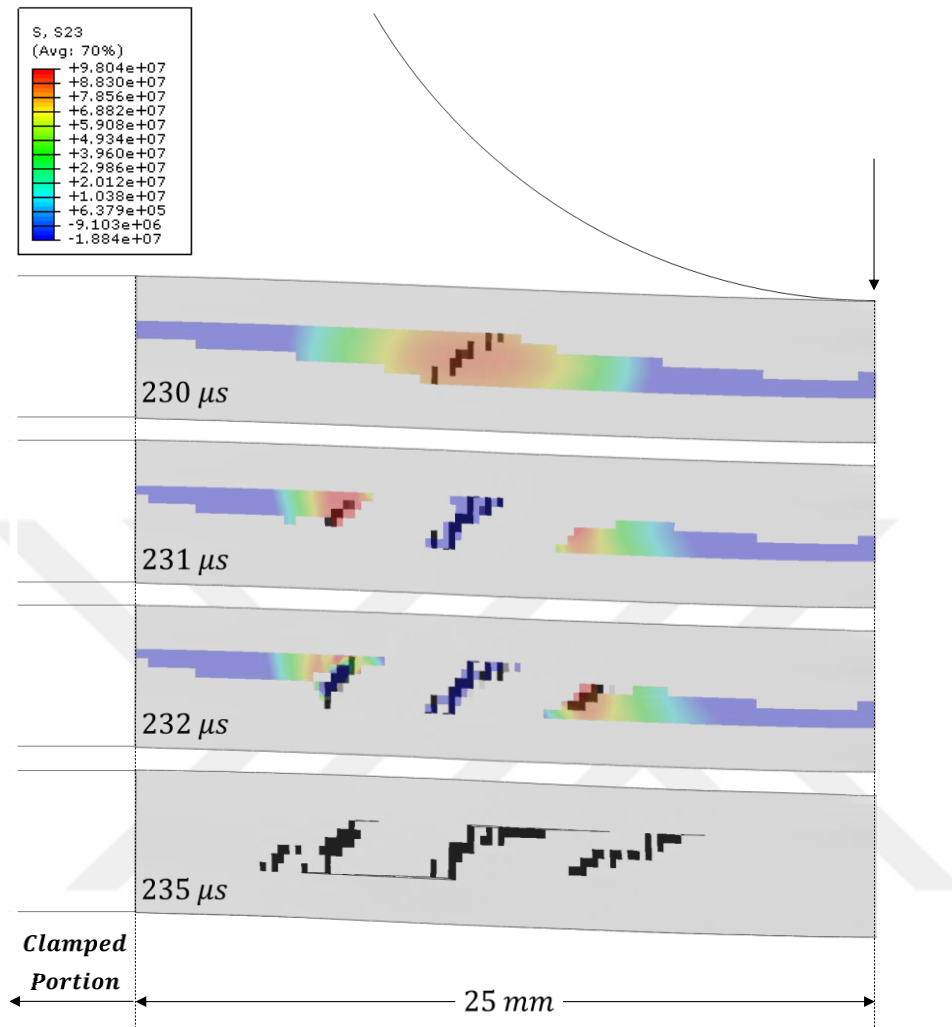


Figure 3.7. Tensile matrix damage formation sequence on half portion of the $[0_5/90_3]_s$ CFRP beam together with the pioneer transverse shear stress (τ_{23}) contours observed on the elements under tension stress in the clustered 90° plies.

Characterization Delamination Propagation

Figure 3.8 shows the variations of crack tip position for 9.15 J and 7.7 J impact analyses with time in comparison with the experimental measurements. The positions of the delamination crack fronts at the top 0/90 interface are measured from the midspan of the beam using the results of finite element analyses. Results show that crack propagation is very similar in the impact events simulated with two different

energies. Although the slope of the imaginary crack tip position vs. time curves are locally same, small amounts of margins occurs following the formation of daughter cracks induced by secondary matrix cracks. It can be deduced that these margins are arisen from the difference between the initiation times of secondary cracks.

Although a clear consistency is obtained in delamination propagation behavior in the finite element analyses of beams impacted at different energies, there is no such agreement between the numerically and experimentally obtained data, as seen in Figure 3.8. This fact asserts the necessity of further investigation of delamination propagation sequence for accurate modelling of impact damage in laminated composites.

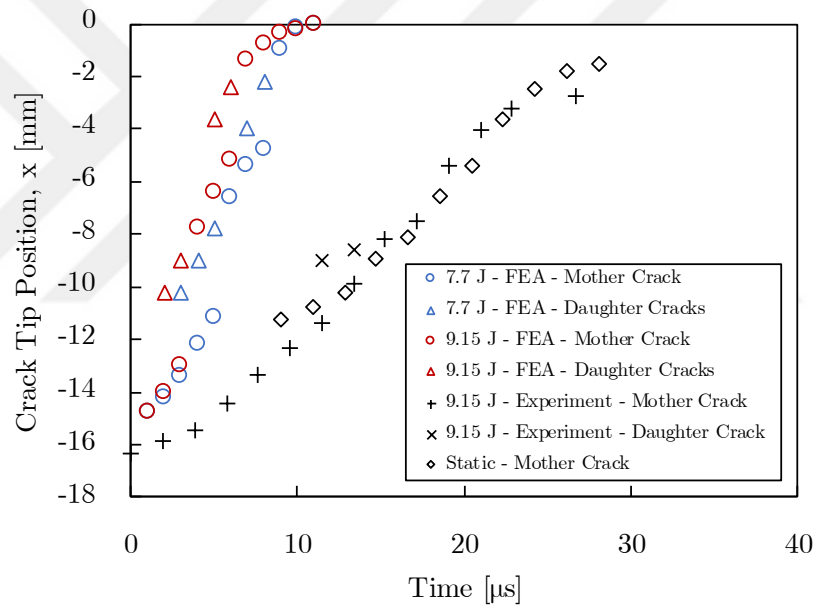


Figure 3.8. Variations of crack tip position for 9.15 J and 7.7 J impact analyses with time in comparison with the experimental measurements.

For this purpose, additional finite element analyses are conducted by changing interlaminar strength and fracture toughness parameters which define the cohesive behavior. The first two finite element analyses are performed with an impact energy of 7.7 J. In the first analysis, all components of the fracture toughness are doubled and

all interlaminar strength terms are kept constant. In case of the second analysis, on the other hand, 1.4 times of all interlaminar strength terms are input in addition to double fracture toughness. The same scenario is repeated with for a 9.15 J impact in the last two analyses. In Figure 3.9a and b, variation of delamination crack tip positions with time are plotted for 7.7 J and 9.15 J impact configurations, respectively, and presented in comparison with the results of static and 9.15 J impact experiments and original finite element analyses of 7.7 J and 9.15 J impact configurations.

Results show that doubling the fracture toughness slightly changes the initial slope of the imaginary crack tip position vs. time curve. However, increasing the components of interlaminar strength to 1.4 times of their original value induces considerable drop in the slope of the imaginary curve. A good agreement is obtained with the experimental data when the reference time is shifted to a larger value (9 μ s) in order to eliminate the delay caused by the difference in the locations where crack initiates.

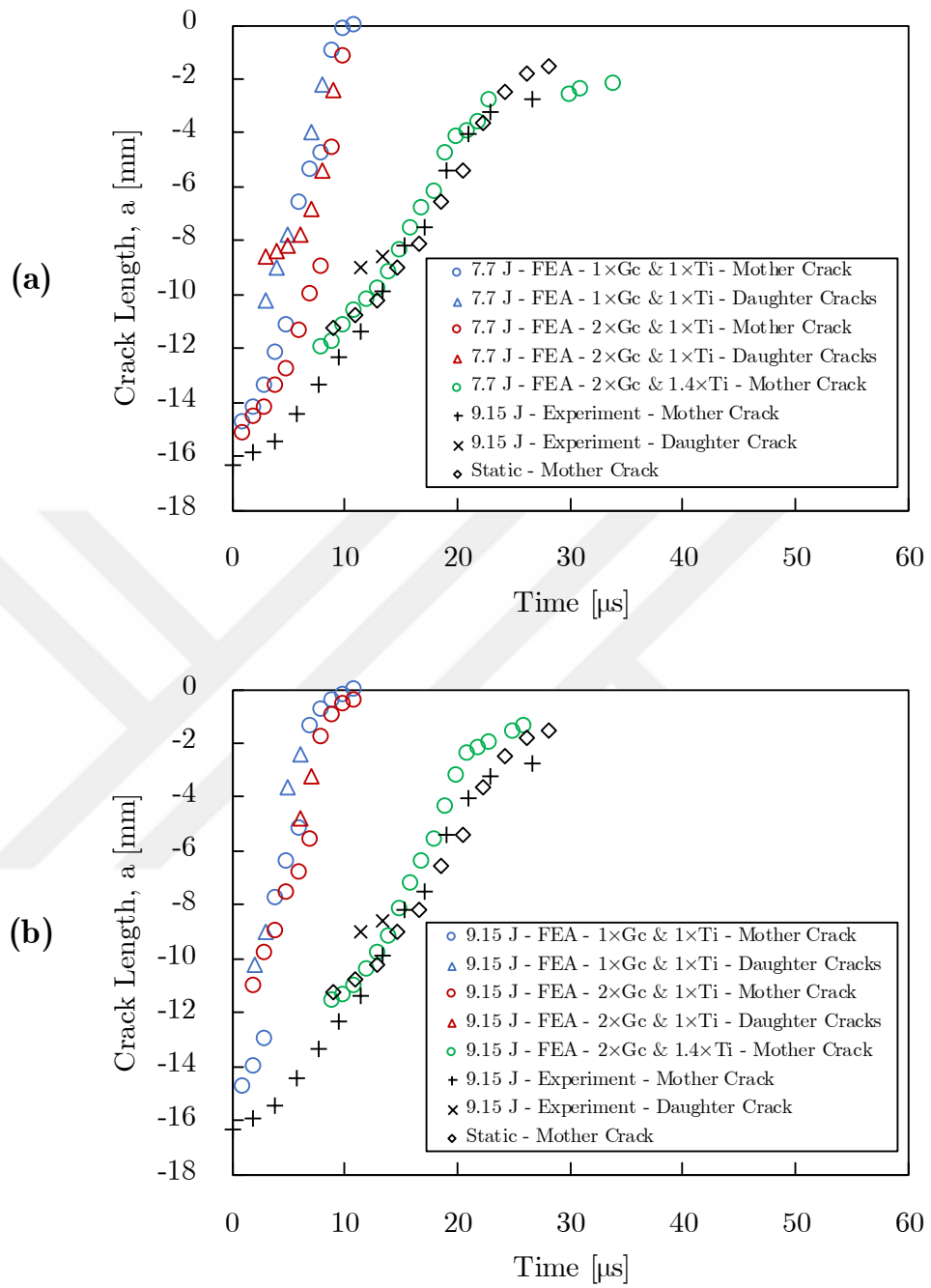


Figure 3.9. Variation of delamination crack tip positions with time for (a) 7.7 J and (b) 9.15 J impact configurations in comparison with the results of static and 9.15 J impact experiments and original finite element analyses of 7.7 J and 9.15 J impact configurations, respectively.

Modelling of Asymmetric Impacts

In this part of the study, results of the finite element analysis of the 9.15 J impact on the $[0_5/90_3]_s$ CFRP composite beam is conducted by shifting the impactor 1 mm as seen in Figure 3.10. The matrix damage occurs initially on the right-hand side of the specimen where the impactor is shifted towards. This crack forms approximately 20 μs earlier compared to symmetric loading. Although a few elements are seen to be damaged on the left-hand side of the beam at 420 μs , development of the matrix damage is completed at 430 μs . This result implies that a time delay of 120 μs is induced between the matrix cracks on each side of the beam by implementing a 1 mm asymmetry into the model.

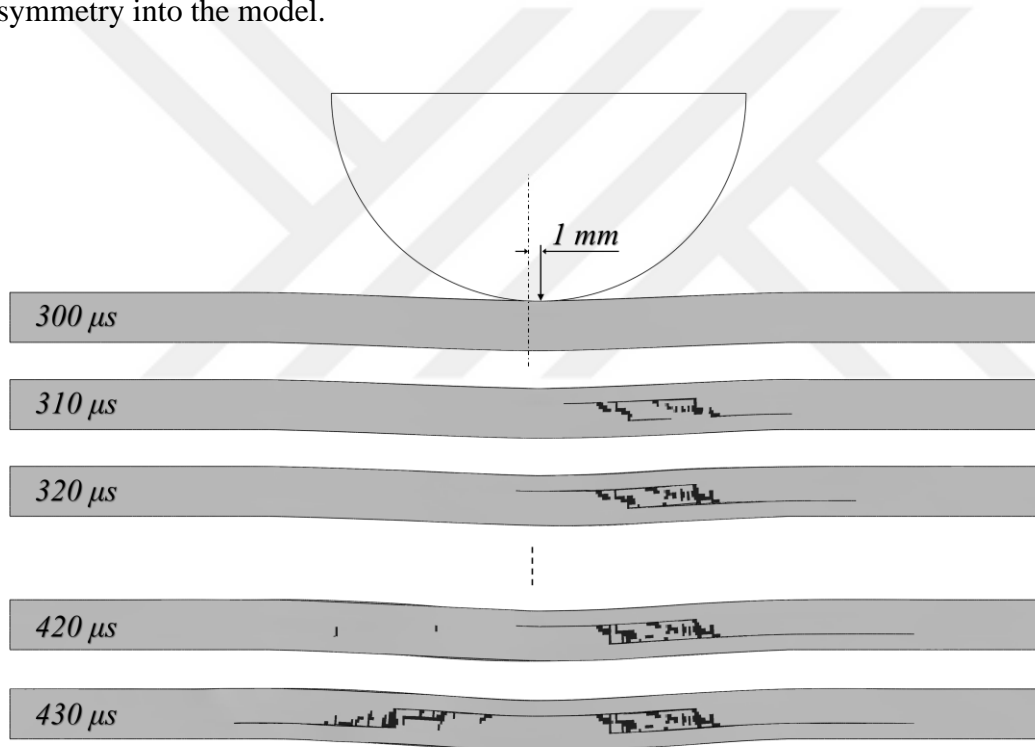


Figure 3.10. Damage formation sequence in the $[0_5/90_3]_s$ CFRP beam subjected to 9.15- J impact with 1 mm-shifted impactor.

3.3.2. $[90_5/0_3]_s$ Beams

Finite element simulation of 7.32 J impact on $[90_5/0_3]_s$ beam is conducted with the detailed model. In this model, squeezing plates are included in the model for better representation of the experimental boundary conditions. The plates squeeze the beam through an out-of-plane displacement of 0.005 mm which is defined to the reference nodes assigned to each clamp. The reason why squeezing plates are modeled instead of simple displacement type boundary condition is the experimental observation of matrix crack formation in top 90° layers near the boundary conditions. Additionally, in some sample runs conducted using the general boundary conditions, it is seen that these cracks are very sensitive to boundary condition assignments and premature formation of them is likely to occur with displacement boundary conditions. Only the results of the finite element analysis conducted with the detailed model is presented in this section.

Figure 3.11 shows the damage formation sequence in the $[90_5/0_3]_s$ beam during 7.32 J impact simulation. Initial failure occurs $315 \mu\text{s}$ after the initial contact in the form of vertical matrix cracks at the maximum bending stress location. At $420 \mu\text{s}$, a delamination front is observed at the region where the vertical matrix cracks reach the neighbor interface. Additionally, vertical matrix cracks form in the upper group of 90° layers at both right and left end of the unsupported portion. At $620 \mu\text{s}$, delaminations initiate at the top $0/90$ interface around each of these matrix cracks. $200 \mu\text{s}$ after this instant, a second vertical matrix crack occurs in the top 90° layers near the former one existing at the left hand side of the beam. From 990 -to- $1030 \mu\text{s}$, two more vertical matrix cracks form in the bottom 90° layers such that one is on the left and the other one is on the right of the initial cracks. When they reach the bottom $0/90$ interface, the left one merges with the existent delamination and the left one nucleates a new delamination front. The last frame in Figure 3.11 corresponds to the instant with maximum impactor displacement. The final damage pattern in the beam is as seen in this frame taken $1460 \mu\text{s}$ after the initial contact.

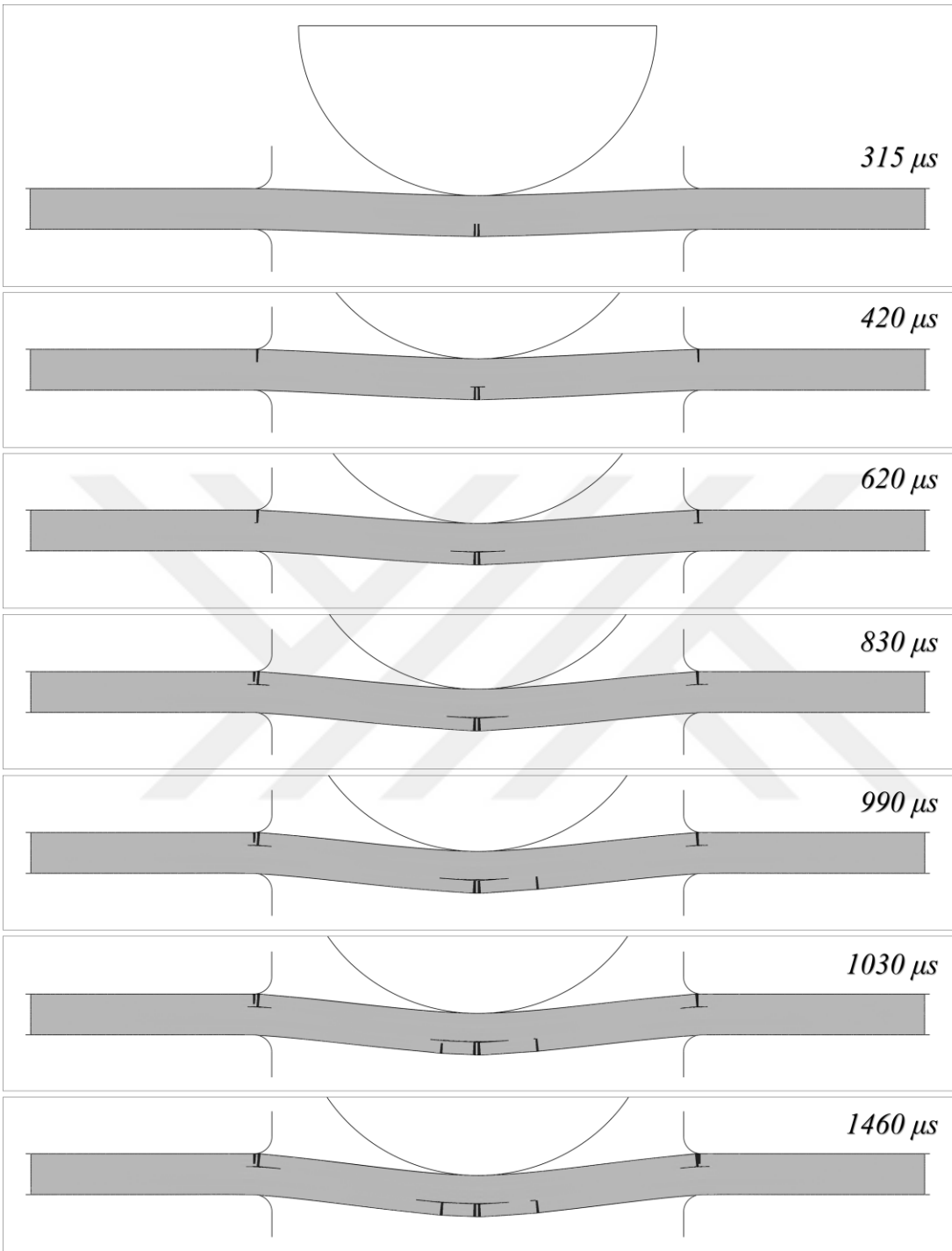


Figure 3.11. Damage formation sequence in the $[90_5/0_3]_s$ CFRP beam subjected to 7.32 J impact

3.4. Conclusions

In this part of the study, finite element simulations of LVI experiments conducted on $[0_5/90_3]_s$ and $[90_5/0_3]_s$ CFRP beams are conducted. For simulation of composite ply damage, a continuum damage mechanics based material model is implemented to ABAQUS/Explicit via a user subroutine VUMAT. Delamination damage is simulated using cohesive zone method with cohesive elements. Results are in good agreement with the experiments in terms of damage form, initiation location and time. Main conclusions of the study are as follows:

- Continuum damage mechanics based material model is able to make a good prediction of the initiation location and time of matrix cracks in both $[0_5/90_3]_s$ and $[90_5/0_3]_s$ CFRP beams.
- It is shown in accordance with the experimental results that diagonal matrix cracks in $[0_5/90_3]_s$ beams are provoked by high shear stresses and that microcracks nucleate new delamination fronts when they reach the interface.
- In the simulations, left and right matrix cracks in $[0_5/90_3]_s$ initiate almost simultaneously. Implementing a 1 mm asymmetry into the model, a time delay of 120 μ s is induced between the matrix cracks on each side of the $[0_5/90_3]_s$ beam, in better agreement with the experimental observations.
- Delamination propagation speeds are not consistent with the experimental observations when original interface properties are used. However, a similar propagation trend is obtained in the finite element model by adjusting the interface properties accordingly. In this exercise, it is concluded that dynamic values of interface properties including interlaminar strength and fracture toughness should be used for accurate simulation of dynamic failure in $[0_5/90_3]_s$ beam subjected to flexural loading.

It is also shown that propagation of dynamic crack $[0_5/90_3]_s$ beam in is very similar in terms of position and time for two different impact energies.



CHAPTER 4

EXPERIMENTAL INVESTIGATION OF LOW-VELOCITY IMPACT DAMAGE IN FIBER-REINFORCED COMPOSITE PLATES

4.1. Introduction

In the study, drop-weight impact tests are conducted on CFRP and GFRP composite plates. A standard drop tower is used for 3-D drop-weight tests. Impact energies are determined using an analytical approach with the aim of creating a reasonable amount of damage in the plate. In the experiments, load acting on the steel impactor is measured by a strain gage embedded into the impactor tup. Post-mortem damage patterns inside the impacted plate specimens are characterized via non-destructive inspection techniques.

4.2. Analytical Model for Impact Response of Composite Plates

Composite plates exhibit different type of behaviors under transverse impact loading depending on the governing parameters of impact event. These governing parameters can be classified into structural, impactor, and environmental parameters. The effect of these parameters on the impact behavior should be understood well in order to estimate the damage caused by an impact since the material response is related to the type of the impact [39].

An analytical model developed by Christoforou and Yigit characterizes elastic response of simple geometries made of anisotropic material subjected to transverse impact event [40]. The analytical model is capable of predicting the maximum force occurred in an elastic impact event which can be indirectly used for damage prediction in a composite laminate as explained later in section 4.3.4. The analytical model described in this section is based on the studies of Christoforou and Yigit [40]-[43].

The type of the impact is classified according to the response of the composite plate under corresponding impact loading as [44]

- Ballistic impact
- Impact on an infinite plate
- Quasi-static impact

Under ballistic impact, seen in Figure 4.1a, the plate response is dominated by the through-the-thickness waves since the contact time is close to the order of time required for the through-the-thickness waves travelling across the thickness. The type of impact response seen in Figure 4.1b is called infinite plate response and occurs when the contact time is greater than the time required for through-the-thickness compressive waves travelling along the thickness, but not sufficient for shear and flexural waves reaching the plate boundaries. In case of a quasi-static impact seen in Figure 4.1c, the contact time is so long that the waves freely travel along through-the-thickness and lengthwise directions.

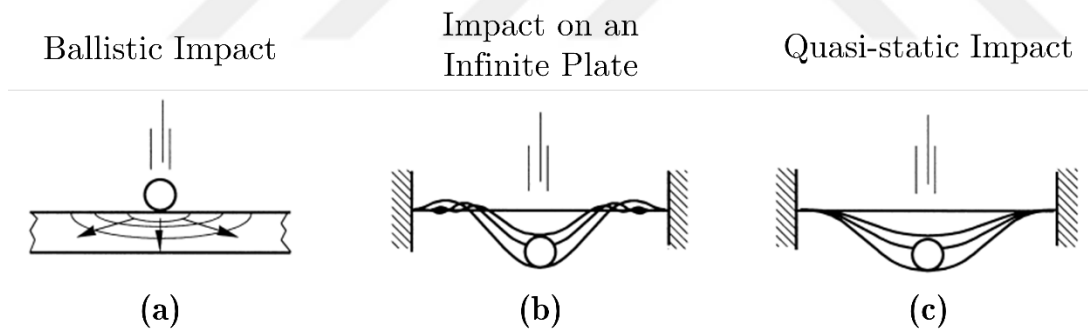


Figure 4.1. Three different types of impact response: (a) ballistic impact, (b) impact on an infinite plate, and (c) quasi-static impact [44].

During a central impact on a simply supported rectangular plate, vertical displacement of the impactor, w_i , can be expressed in terms of central deflection of the plate mid-plane, w_0 , and the local indentation at the impact point, α , as follows [44]

$$w_i = w_0 + \alpha \quad (4.1)$$

An equilibrium is set between the inertial load of the impactor, F_i , the contact load, F_c , and the load due to plate deflection, F_0 , as

$$F_i = F_c = F_0 \quad (4.2)$$

The inertial load of the impactor is defined in terms of impactor mass, M_i , and motion of the impactor, w_i , as shown in Eq. (4.3).

$$F_i = -M_i \ddot{w}_i \quad (4.3)$$

The contact load is expressed via linearized contact law in terms of contact stiffness, k_α , indentation, α , as

$$F_c = k_\alpha \alpha \quad (4.4)$$

The contact stiffness is expressed in terms of impactor tip radius, R , and shear strength of the laminate, S_u , as [45]

$$k_\alpha = 10.4RS_u \quad (4.5)$$

The load due to plate deflection equation differs for ballistic impact behavior, impact on an infinite plate behavior, and quasi-static impact behavior. Since the ballistic impact is beyond the scope of this study, two different plate deflection loads will be considered: deflection load due to quasi-static impact behavior and deflection load due to impact to an infinite plate behavior which are expressed as

$$F_0 = k_{bs}w_0 + k_m w_0^3 + M_p^* \ddot{w}_i \quad \text{for quasi-static impact behavior} \quad (4.6)$$

$$F_0 = 8\sqrt{I_1 D^*} \dot{w}_0 \quad \text{for infinite plate behavior} \quad (4.7)$$

The k_{bs} and k_m terms in the quasi-static plate deflection load equation are bending-shearing and membrane stiffnesses of the plate and the M_p^* term is the equivalent lumped mass of the plate. The bending-shearing stiffness term, k_{bs} , is expressed in terms of effective plate stiffness, D^* , and the smallest in-plane size of the plate, b , as

$$k_{bs} = \frac{D^*}{0.01116b^2} \quad (4.8)$$

The effective plate stiffness term is a combination of bending stiffness terms of the plate and it is given as

$$D^* = \sqrt{\frac{1}{2}D_{11}D_{22} \left(\frac{D_{12} + 2D_{66}}{\sqrt{D_{11}D_{22}}} + 1 \right)} \quad (4.9)$$

The equivalent lumped mass term of the plate, M_p^* , is a function of plate mass, M_p . For a simply supported rectangular plate, M_p^* is defined as

$$M_p^* = \frac{M_p}{4} \quad (4.10)$$

The I_1 term in the deflection load equation for infinite plate behavior is the inertial term and expressed in terms of plate mass, M_p , and in-plane area of the plate, A_p as

$$I_1 = \frac{M_p}{A_p} \quad (4.11)$$

Using the force equilibrium shown in Eq. (4.2), governing equations are obtained for each type of response, namely quasi-static and infinite plate responses as

$$\left(1 + \frac{k_\alpha}{k_{bs}}\right) \ddot{\alpha} + \frac{k_\alpha}{M_i} \alpha = 0 \quad \text{for quasi-static impact behavior} \quad (4.12)$$

$$\ddot{\alpha} + \frac{k_\alpha}{8\sqrt{I_1 D^*}} \dot{\alpha} + \frac{k_\alpha}{M_i} \alpha = 0 \quad \text{for infinite plate behavior} \quad (4.13)$$

Through the derivation of governing equation for quasi-static plate behavior, M_p and k_m terms are neglected.

The boundary conditions of the quasi-static behavior and infinite plate behavior are written as

$$\alpha_0 = 0, \dot{\alpha}_0 = \frac{k_{bs}}{k_{bs}+k_\alpha} V_0 \quad \text{for quasi-static impact behavior} \quad (4.14)$$

$$\alpha_0 = 0, \dot{\alpha}_0 = V_0 \quad \text{for infinite plate behavior} \quad (4.15)$$

where V_0 denotes the initial impact velocity.

Non-dimensionalizing the above governing equations helps to characterize the impact behavior. The normalization factors are maximum indentation, α_{max} , impactor mass, M_i , and inverse of the linear contact frequency, $\sqrt{M_i/k_\alpha}$, for length, mass and time, respectively. Assuming that all the impact energy is dissipated to create maximum amount of indentation by neglecting the global response of the plate, α_{max} is written as

$$\alpha_{max} = V_0 \sqrt{\frac{M_i}{k_\alpha}} \quad (4.16)$$

The non-dimensional governing equations for quasi-static behavior and infinite plate behavior are shown in Eq. (4.17) and Eq. (4.18), respectively. The non-dimensional values are expressed with an over bar.

$$(1 + \lambda^{-1})\ddot{\bar{\alpha}} + \bar{\alpha} = 0 \quad \text{for quasi-static impact behavior} \quad (4.17)$$

$$\ddot{\bar{\alpha}} + 2\zeta_w \dot{\bar{\alpha}} + \bar{\alpha} = 0 \quad \text{for infinite plate behavior} \quad (4.18)$$

where relative stiffness of the structure, λ , is defined as $\lambda = k_{bs}/k_\alpha$, and the loss factor, ζ_w , is defined as $\zeta_w = (1/16)\sqrt{k_\alpha M_i/I_1 D^*}$. Non-dimensional boundary conditions can be written as

$$\alpha_0 = 0, \dot{\alpha}_0 = \frac{k_{bs}}{k_{bs}+k_\alpha} V_0 \quad \text{for quasi-static impact behavior} \quad (4.19)$$

$$\alpha_0 = 0, \dot{\alpha}_0 = V_0 \quad \text{for infinite plate behavior} \quad (4.20)$$

Eq. (4.17) and Eq. (4.18) should be solved for characterization of the impact response. For quasi-static impact response, the solution of Eq. (4.17) is obtained as

$$\bar{\alpha}(\bar{t}) = \sqrt{\frac{\lambda}{1+\lambda}} \sin\left(\sqrt{\frac{\lambda}{1+\lambda}} \bar{t}\right) \quad (4.21)$$

The values of the characterization parameters, relative stiffness, λ , and the loss factor, ζ_w , are calculated for each specimen to use in the impact characterization diagram in order to determine the type of the impact response. Throughout these calculations, impactor mass, radius, plate geometry, and material properties are the necessary inputs. For a specific plate, impactor mass is the only remaining variable for the calculation of characterization parameters. Therefore, it is required to perform the characterization parameter calculations at different impactor masses in order to determine the behavior type correctly.

After the determination of the impact type, solution to the governing equation of the corresponding impact type is utilized for determination of dimensionless maximum force, \bar{F}_{max} . Since the non-dimensional indentation and force parameters, $\bar{\alpha}$ and \bar{F} , are dependent on the non-dimensional time, \bar{t} , and are equal to each other. Therefore, the dimensionless maximum force, \bar{F}_{max} , is

$$\bar{F}_{max} = \bar{\alpha}_{max} \quad (4.22)$$

The maximum elastic impact force is then written as

$$F_{max} = \bar{F}_{max} V_0 \sqrt{M_i k_\alpha} \quad (4.23)$$

The resultant impact characterization diagram which is shown in Figure 4.2 has two non-dimensional parameters and four different regions [43]. The right-side of the diagram corresponds to the quasi-static impact. Between the infinite plate solution line and quasi-static boundary, there is a transition region where the type of the behavior is a mixture of these two behaviors. The region lying close to the $\bar{F} = 1$ results in the half-space behavior. After determining the type of impact, non-dimensional force value of the corresponding impact configuration can be determined from the vertical axis of the impact characterization diagram.

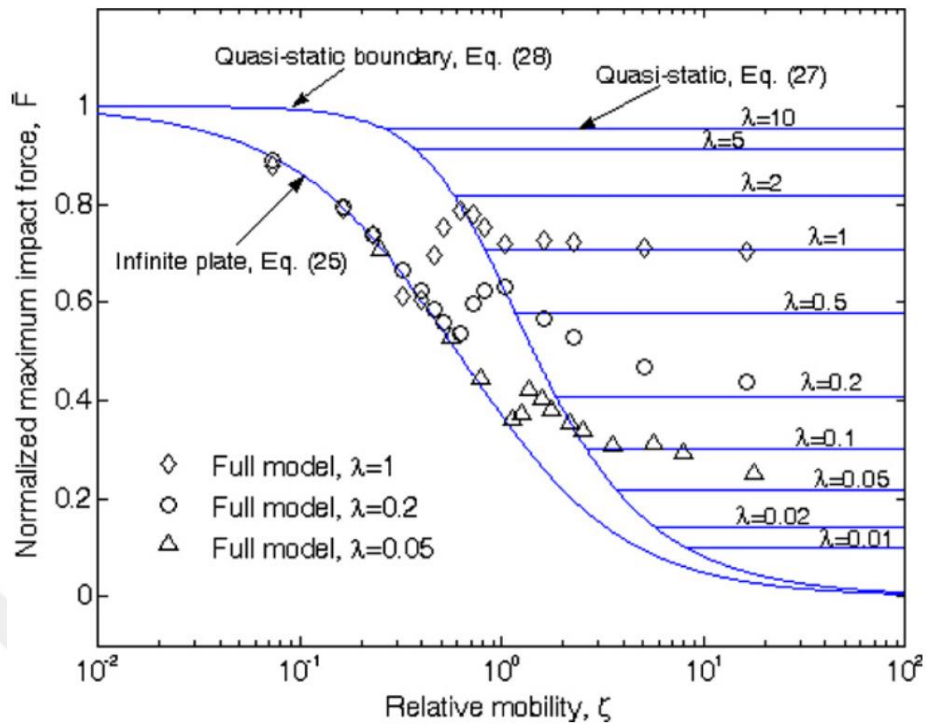


Figure 4.2. Impact characterization diagram [43].

4.3. Experimental Method

In this section, experimental method followed in drop-weight impact testing of composite plates is described. Specimen preparation, experimental setup and determination of impact energies are explained in detail.

4.3.1. Material and Specimen Preparation

$[0_8/90_2]_s$ and $[0_4/90_4/0_2]_s$ composite plate specimens are manufactured using HEXPLY 913 132 HTA unidirectional carbon fibers prepreg and HEXPLY 913 132 unidirectional glass fibers prepreg by hand layup technique. Each batch is cured subsequently at $80 \pm 5^\circ$ for 30 minutes and at $125 \pm 5^\circ$ for 60 minutes at a pressure level of 4 bars in autoclave. These batches are cut into plate specimens of $150 \text{ mm} \times 100 \text{ mm}$ using a water jet.

4.3.2. Experimental Setup

Drop-weight impact experiments are conducted with INSTRON 9340 Drop Tower Impact System equipped with standard instruments according to ASTM D7136 [46], as shown in Figure 4.3a. The impact setup consists of a steel specimen fixture, an impactor crosshead assembly, a carrier, a rebound catcher mechanism, and guiding shafts. The specimen is placed on the steel specimen fixture base which has a rectangular opening of 125 mm x 75 mm and four rubber tip clamps mounted on in order to squeeze the specimen, as shown in Figure 4.3b. The impactor crosshead assembly consisting of a strain gage instrumented impactor tup and a tup-holder weighs 3.387 kg with no additional mass. The impactor tup, which is shown in Figure 4.3c, has a hemispherical tip of 16 mm diameter.

Prior to experiment, drop height of the impactor is adjusted automatically by the carrier system for the prescribed impact energy and mass inputs. The impactor crosshead assembly is released by a quick release mechanism. During the impact event, the load acting on the impactor tup is measured through the strain gages and the load data is sampled by the data acquisition system. After the impactor rebounds from the specimen surface, the anti-rebound system actuated by hydraulic cylinders prevents the secondary impacts on the specimen by catching the crosshead.

Following the impact experiments, damage patterns in the tested specimens are captured using non-destructive techniques. For post-mortem damage visualization of GFRP plates is performed by enlightening the specimens with a monochromatic light source as seen in Figure 4.4a. This process works properly for glass fiber composites through their sufficient translucency. For CFRP plates, on the other hand, an optical infrared thermography setup seen in Figure 4.4b is used to visualize the final damage pattern.

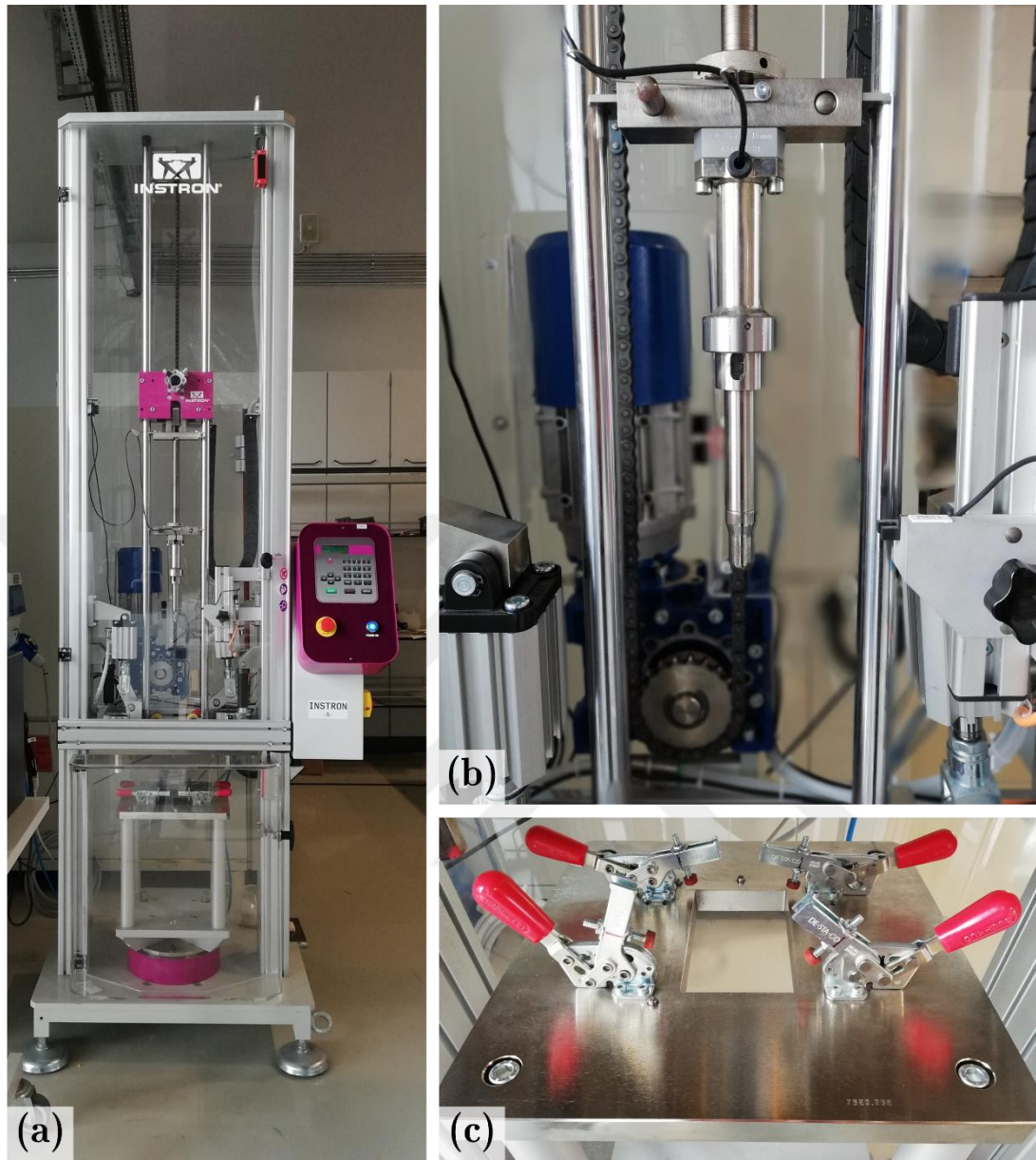


Figure 4.3. (a) INSTRON 9340 drop tower impact system, (b) specimen fixture, and (c) hemispherical impactor tup.



Figure 4.4. Post-mortem damage visualization of (a) GFRP specimens using a monochromatic light source, and (b) CFRP specimens using an optical infrared thermography setup.

4.3.3. Test Procedure

Energies applied in the drop weight impact experiments of $[0_8/90_2]_s$ and $[0_4/90_4/0_2]_s$ specimens are determined following the procedure explained section 4.3.4. In order to obtain the desired energy level, additional mass is installed on the impactor crosshead if necessary.

Before starting the drop-weight experiments thickness of each specimen is measured using a digital comparator as shown in Figure 4.5. These thickness values are inputted to the software of the impact system for adjustment of the release height and the triggering point of the anti-rebound system. The specimen is located on the steel fixture base seen in Figure 4.3c and centered with respect to the window by use of guiding pins mounted on the base table according to ASTM D7136 test standard [46].

The specimen is fixed by four rubber-tipped clamps to prevent its rebound during the impact. During the impact event, the load data is collected at 1 kHz sampling rate.

At the end of the impact test, the specimen is removed from the fixture and subjected to non-destructive inspection (NDI), if required. In the NDI of CFRP plates, thermography technique is used. The specimen is enlightened with halogen lamps at 0.5 Hz and a thermal camera captures discontinuities inside the specimen throughout the procedure. GFRP plates, on the other hand, are positioned in front of a monochromatic light source and photographs of the internal damage pattern are taken with a digital camera.

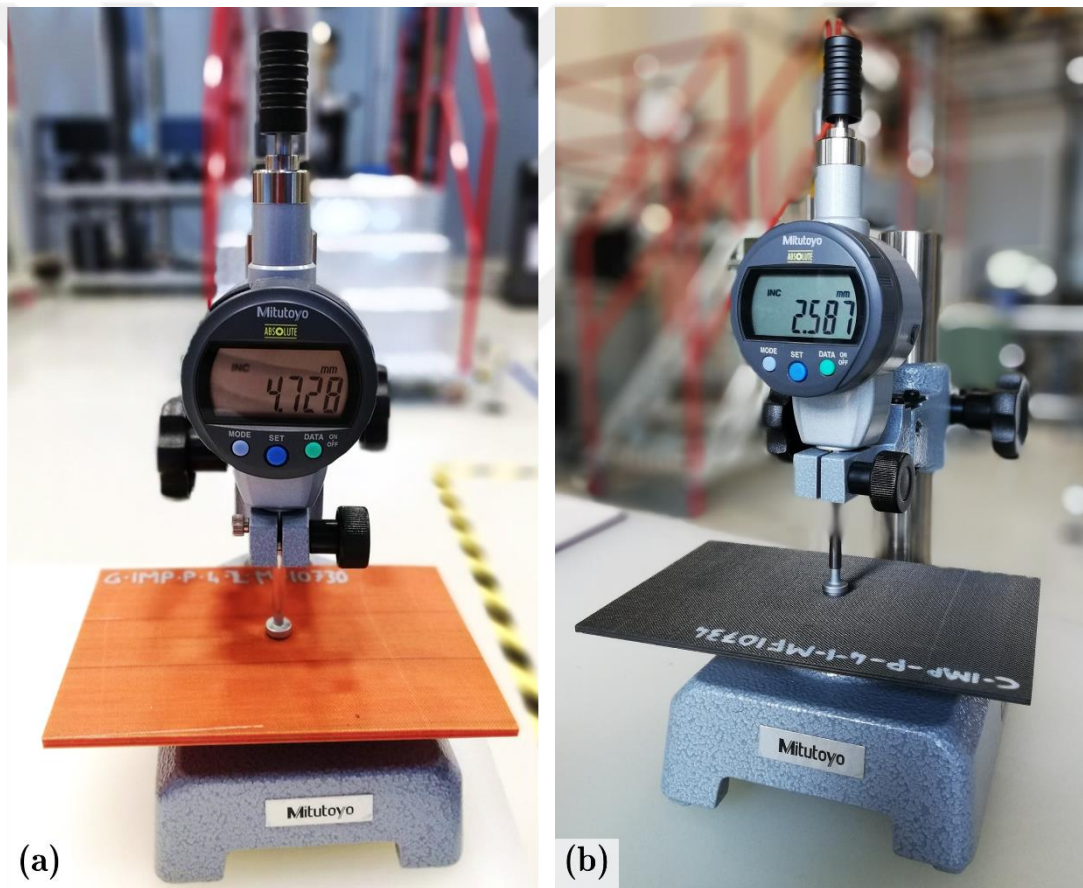


Figure 4.5. Measurement of (a) GFRP and (b) CFRP plate thicknesses using a digital comparator.

4.3.4. Determination of Impact Energies

Since the aim of this study is to understand the delamination damage mechanisms in CFRP and GFRP composite plates under impact loading, the damage created by the impact should be neither too small to be able to observe nor too large to cause penetration. It should be in the range in which the damage mechanisms can be elucidated and used as a substantial foundation in the evaluation of numerical results. For this purpose, the analytical method developed for low-velocity impact of composite plates in Section 4.2 is used to determine the energy required for the expected damage.

4.3.4.1. Analytical Determination of Delamination Threshold Energy

In this section, a semi-analytical approach is developed to determine the energy required for the expected damage using the F_{max} obtained from the analytical method described in Section 4.2.

A relation between the maximum elastic force, F_{max} , and the impact energy, E_0 , can be derived by manipulating Eq. (4.23) as follows

$$\frac{1}{2} \frac{F_{max}^2}{k_\alpha \bar{F}_{max}^2} = \frac{1}{2} M_i V_0^2 = E_0 \quad (4.24)$$

When maximum elastic force, F_{max} , is equal to the force required to create delamination, F_{del} , the energy term in Eq. (4.24), the impact energy, E_0 , is equal to the energy required to create delamination, E_{del} , which can be written in terms of F_{del} , \bar{F}_{max} , V_0 , M_i and k_α as

$$E_{del} = \frac{1}{2} \frac{F_{del}^2}{k_\alpha \bar{F}_{max}^2} \quad (4.25)$$

The delamination force, F_{del} , is defined by Suemasu and Majima [47] in terms of Mode II interlaminar fracture toughness, G_{IIc} , and effective plate stiffness, D^* , as

$$F_{del} = \pi \sqrt{\frac{32D^* G_{IIc}}{n + 2}} \quad (4.26)$$

The number of delaminations, n , can be taken as unity for prediction of delamination onset [48].

Then a magnification factor, kF , is applied on the delamination initiation force in Eq. (4.25) to scale up the impact energy according to the desired level of damage and to compensate the possible mispredictions of the analytical approach. This yields to following expression for the impact energy to be applied in the experiments.

$$E_0 = \frac{1}{2} \frac{(kF \cdot F_{del})^2}{k_\alpha \bar{F}_{max}^2} \quad (4.27)$$

4.3.4.2. Preliminary Tests to Estimate Impact Energy Levels

The kF values applied on the delamination initiation force magnify the impact energy, however the amount of magnification should be checked in order to control whether the resultant delamination damage fits to the desired level of damage or not. Therefore, pre-estimation of the experimental impact energies is performed for specific kF values on various specimens which are spared as dummy specimens to be used for determination of appropriate kF values. The characterization parameters for dummy specimens are calculated and they are found to be in quasi-static impact region for all possible impactor mass values. The corresponding delamination forces of the dummy specimens are calculated using the expressions stated in Eq. (4.25) and Eq. (4.26). Table 4.1 shows the stacking sequences, delamination forces, F_{del} , delamination threshold energies, E_{del} , selected kF values and experimental energies, E_0 , corresponding to that kF values for each dummy specimen. Specified kF values are chosen by comparing experimental energies and corresponding post-mortem damage states found in the literature [39], [48].

Table 4.1. Stacking sequences, predicted delamination forces and energies, kF values, and experimental energies of the dummy CFRP and GFRP plates.

	Stacking Sequence	F_{del} [kN]	E_{del} [J]	kF	E_0 [J]
CFRP	[0 ₇ /25/-25/25/-25/0 ₉]	1.60	2.10	2.5	13.1
				3	18.9
	[0 ₈ /45/-45/45/-45/0 ₈]	1.74	2.12	2	8.5
				2	8.5
				2.35	11.7
				2.35	12.5
GFRP	[(0 ₂ /90 ₂) ₃ /0 ₄ /90 ₂ /0 ₂]	2.35	2.26	3.5	27.7
				2	22.0
	[0 ₈ /25/-25/25/-25/0 ₈]	5.04	5.51	3	49.6
				2.5	34.4
				2.5	34.4
				2.5	36.3
[(0 ₂ /90 ₂) ₃ /0 ₄ /0 ₂ /90 ₂]	5.51	5.81	2.5	36.3	
			2.5	36.3	

Figure 4.6 shows the post-mortem images of the dummy GFRP specimens of [0₈/25/-25/25/-25/0₈] when $kF = 2, 2.5, 3$ and of [(0₂/90₂)₃/0₄/0₂/90₂] when $kF = 2.5$. The damage areas of these specimens are between the limits of delamination area considerations. As the kF value increases for the same stacking sequence, the delamination area increases, and it takes the form of a peanut along the fiber direction. Figure 4.6c has a greater delamination area when compared with the Figure 4.6d even though they have the same kF . The main reason is the number of different angle ply

interfaces since the same amount of energy would create smaller delamination area in a laminate which has high number of interfaces. Since the $[0_7/25/-25/25/-25/0_9]$ laminate (Figure 4.6c) has 8 different angle interfaces and laminate $[(0_2/90_2)_3/0_4/90_2/0_2]$ (Figure 4.6d) has 5 of it, it is expected to observe a larger projected delamination area in $[(0_2/90_2)_3/0_4/90_2/0_2]$ laminate under similar impact energy levels.



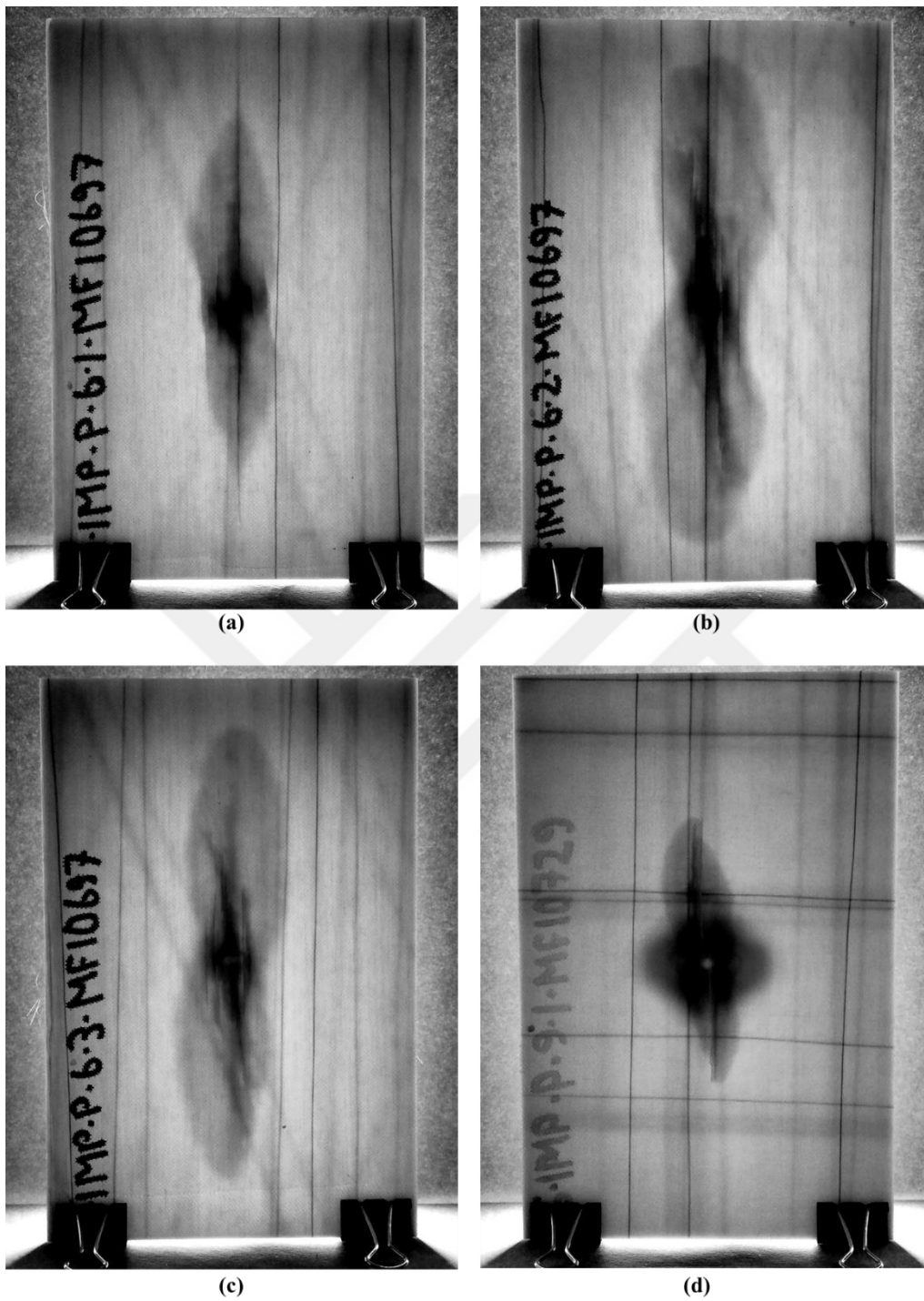


Figure 4.6. Post-mortem pictures of the dummy GFRP specimens of (a) $[0_7/25/-25/25/-25/0_9]$ and $kF = 2$, (b) $[0_7/25/-25/25/-25/0_9]$ and $kF = 3$, (c) $[0_7/25/-25/25/-25/0_9]$ and $kF = 2.5$, (d) $[(0_2/90_2)_3/0_4/90_2/0_2]$ and $kF = 2.5$.

Figure 4.7 shows the post-mortem thermography image of a dummy $[(0_2/90_2)_3/0_4/90_2/0_2]$ CFRP specimen impacted at 12.5 J energy corresponding to $kF = 2.35$. The area of the impact delamination is reasonable under the given kF value for a laminate having relatively high number of different angle ply interfaces.

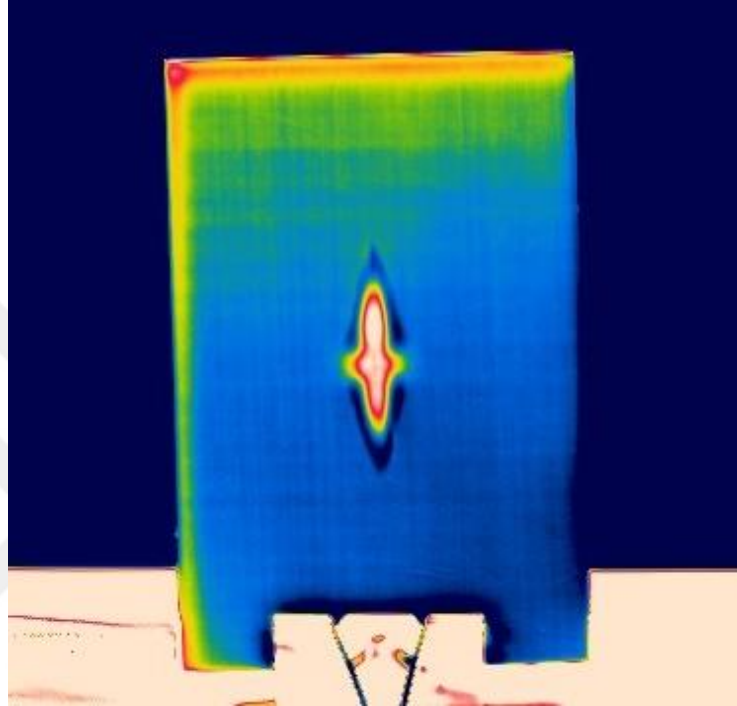


Figure 4.7. Thermography image of a dummy $[(0_2/90_2)_3/0_4/90_2/0_2]$ CFRP specimen showing the delamination damage under 12.5 J impact ($kF = 2.35$).

The kF values chosen for the pre-estimation of the experimental impact energies of dummy specimens resulted in desired level of damage. Therefore, kF values in the range of 2-3 are expected to generate reasonable amount of damage in the real test specimens.

4.3.4.3. Estimation of Impact Energies for Real Specimens

The determination of the kF values of main specimens are done according to the results of pre-estimation tests. Since kF values in the range of 2-3 generated the reasonable amount of damage, all kF values of the main specimens are again chosen

in the range of 2-3, as shown in Table 4.2. Among these values, some exceptions are made by choosing the kF values as 1.5 in order to observe the elastic-like behavior of some plates.

Table 4.2. Stacking sequences, predicted delamination forces and energies, kF values, and experimental energies of the real CFRP and GFRP specimens.

	Stacking Sequence	F_{del} [N]	E_{del} [J]	kF	E_0 [J]
CFRP				2	10
	[0 ₄ /90 ₄ /0 ₂] _s	2243.2	2.23	2.5	15
				2.5	15
				2.5	15
	[0 ₈ /90 ₂] _s	1764.5	2.13	2	10
				2.5	15
1.5				5	
GFRP	[0 ₄ /90 ₄ /0 ₂] _s	5405.5	5.74	1.5	13
				2.5	35
				2.5	35
	[0 ₈ /90 ₂] _s	5055.4	5.52	2	20
				2	20
				1.5	13

4.4. Experimental Results

Results of the impact experiments on selected CFRP and GFRP plates including load-displacement behaviors and post-mortem damage patterns are presented in this section.

4.4.1. Results of CFRP Specimens

4.4.1.1. $[0_4/90_4/0_2]_s$ CFRP Plates

Four $[0_4/90_4/0_2]_s$ CFRP plates (named also C-IMP-P-4) are impacted at in order of 10 J, 15 J, 15 J, and 15 J. The resultant load-displacement curves obtained from each test are shown in Figure 4.8. The repeatability of the impact tests is demonstrated via the consistency in global behavior. Although the impact energy is different, delamination force, where the first sharp drop in load is observed in load-time history [46], is almost constant in the experiments. Loads corresponding to the delamination formation are ranging from 2.19 kN to 2.42 kN. Average of these forces is found 2.32 kN as seen in the Figure 4.8, and this value is close to the predicted delamination force. The energy absorbed in 10 J – impact is 6.4 J while they are 10.5 J, 10.3 J and 10.2 J in 15 J – impacts. Accordingly, projected delamination areas are expected to be wider in the plates impacted at 15 J.

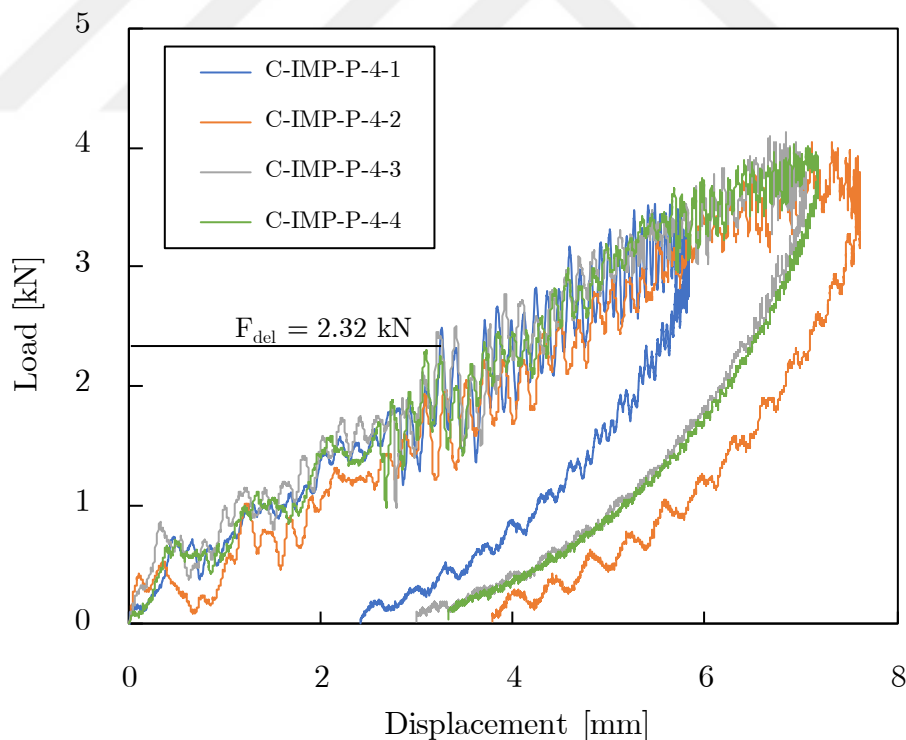


Figure 4.8. Load-displacement curves of $[0_4/90_4/0_2]_s$ CFRP specimens.

Post-mortem thermography images of the C-IMP-P-4-1 and C-IMP-P-4-2 specimens are seen in Figure 4.9 and Figure 4.10, respectively. Resultant delamination amounts are as desired in both specimens implying the accuracy of the impact energy estimations. Projected delamination area is larger in C-IMP-P-4-2 as expected since more energy is absorbed. It should be noted that peanut shape of delamination is wider along longitudinal direction of the plate. This is because the lowermost plies are oriented parallel to the longitudinal axis of the plate and is expected in accordance with the bending stiffness mismatching concept.

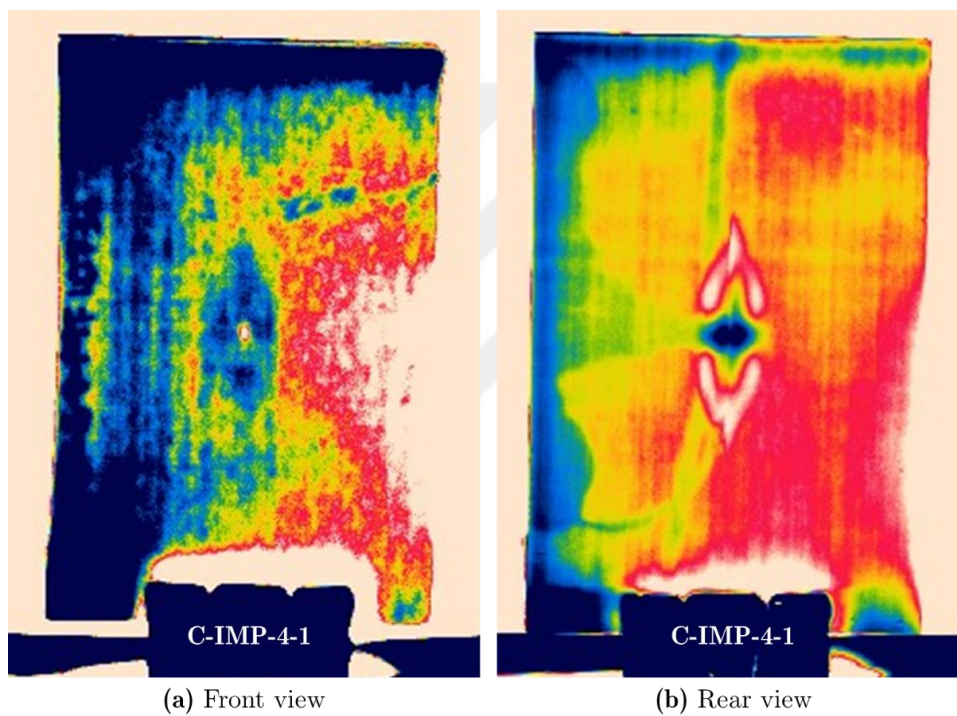


Figure 4.9. Post-mortem thermography images of the C-IMP-P-4-1 specimen.

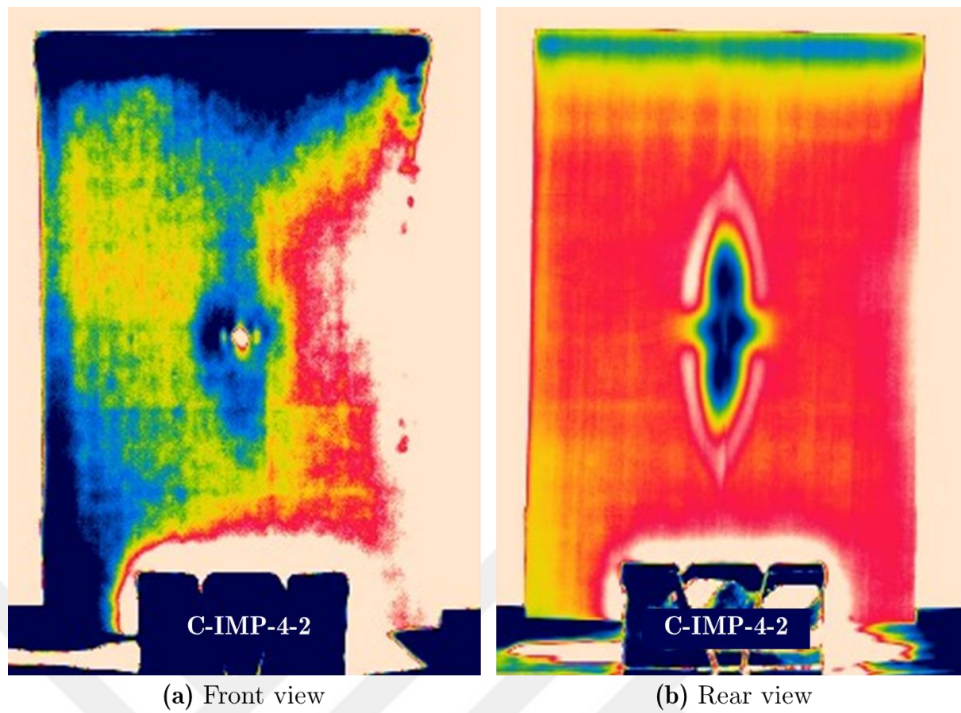


Figure 4.10. Post-mortem thermography images of the C-IMP-P-4-2 specimen.

4.4.1.2. $[0_8/90_2]_s$ CFRP Plates

10 J, 15 J and 5 J impact experiments are conducted on three $[0_8/90_2]_s$ CFRP specimens C-IMP-P-5-1, C-IMP-P-5-2 and C-IMP-P-5-3, respectively. Load-displacement curves obtained from these experiments are shown in Figure 4.11. The average delamination force for $[0_8/90_2]_s$ CFRP specimens is calculated as 1.68 kN while the predicted force is 1.76 kN. Amount of energies absorbed by the plates are 6.1 J, 11.6 J, and 3.0 J for 10 J, 15 J, and, 5 J impacts, respectively.

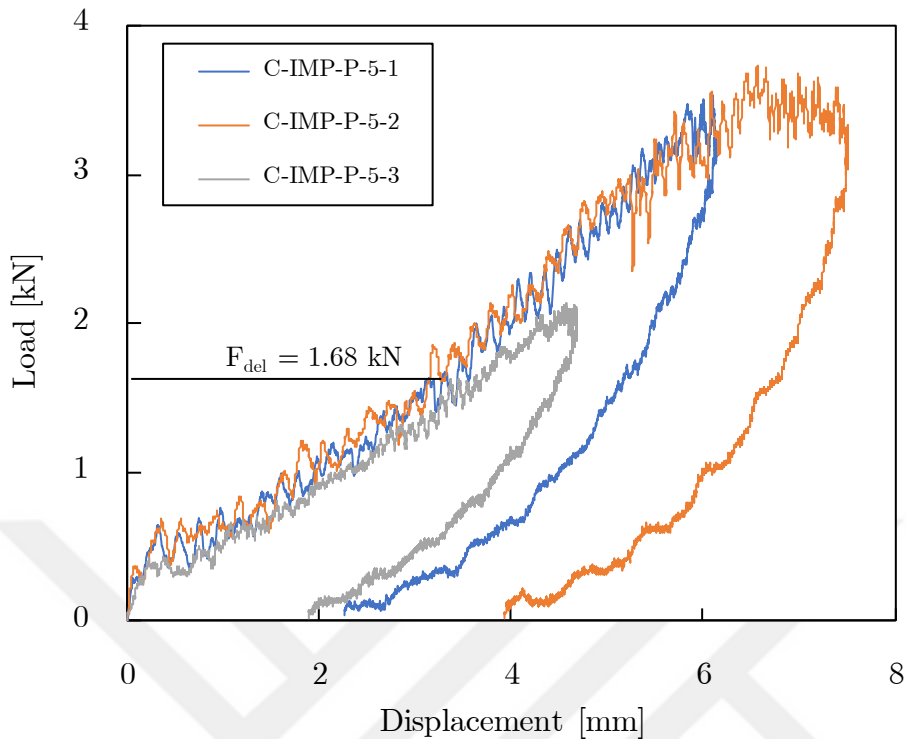


Figure 4.11. Load-displacement curves of $[0_8/90_2]_s$ CFRP specimens.

Figure 4.12 and Figure 4.13 show the post-mortem thermography images of the C-IMP-P-5-1 and C-IMP-P-5-2 specimens, respectively. The amount of delamination is satisfactory for both specimens. Projected delamination area is larger in C-IMP-P-5-2 as expected due to the higher amount of absorbed energy. Additionally, the projected delamination areas are greater in $[0_8/90_2]_s$ specimens compared to that in $[0_4/90_4/0_2]_s$ specimens impacted at the same energies. This is expected because similar levels of energies are dissipated with formation of delamination at fewer interfaces. Similar to the post-mortem images of $[0_4/90_4/0_2]_s$ specimens, larger delaminations extend along the longitudinal plate axis and peanut shape is preserved.

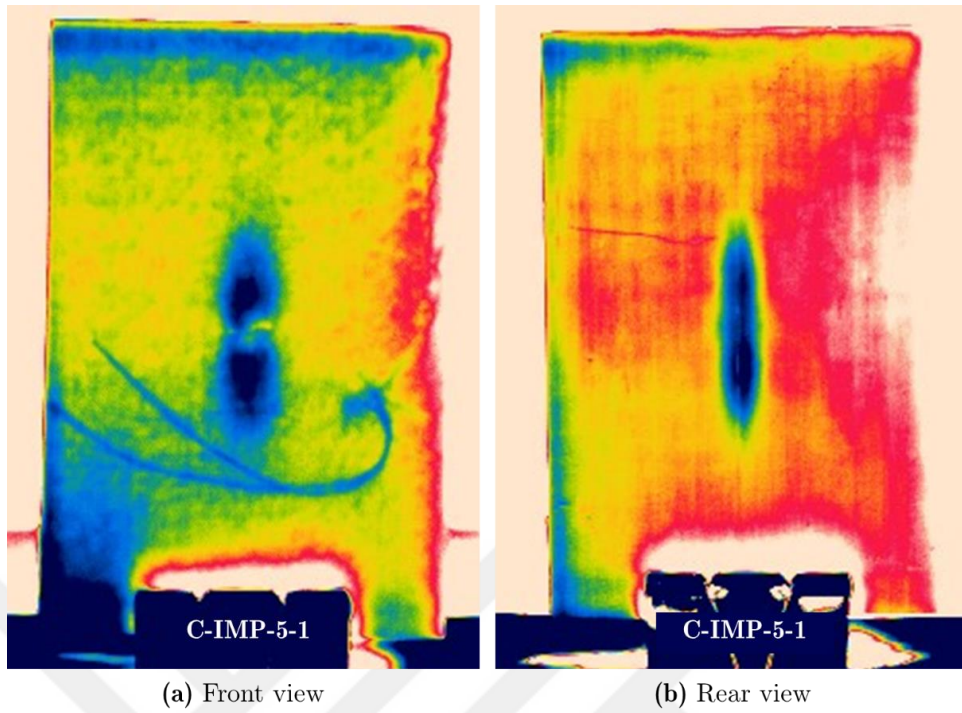


Figure 4.12. Post-mortem thermography images of the C-IMP-P-5-1 specimen.

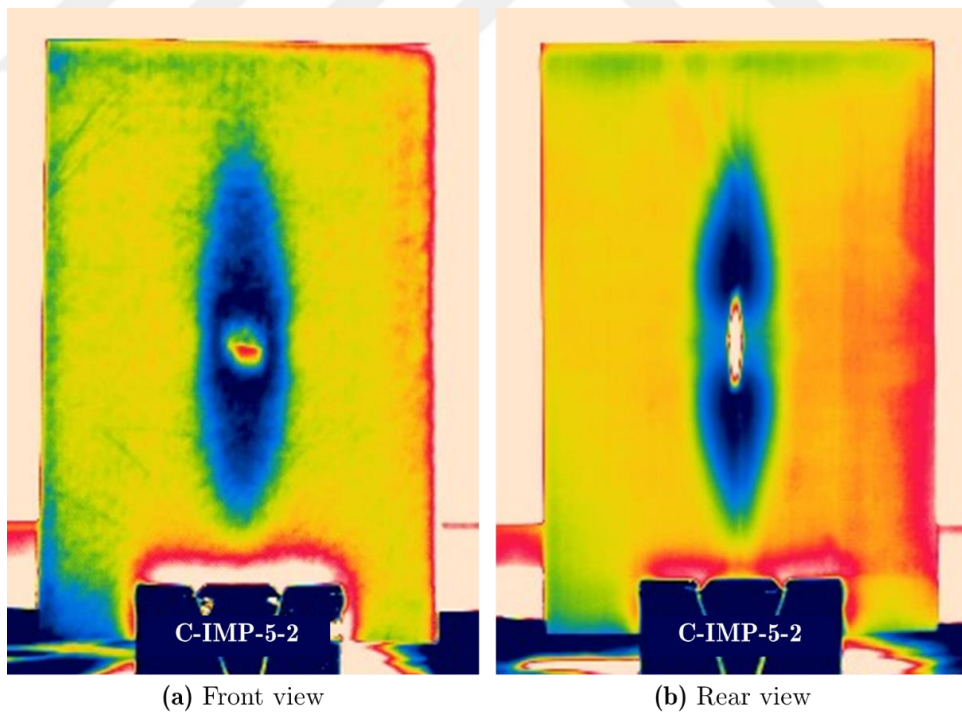


Figure 4.13. Post-mortem thermography images of the C-IMP-P-5-2 specimen.

4.4.2. Results of GFRP Specimens

4.4.2.1. $[0_4/90_4/0_2]_s$ GFRP Plates

Figure 4.14 shows the load-displacement curves of the $[0_4/90_4/0_2]_s$ GFRP specimens tested at 13 J, 35J, 35J and 20 J impact energies. The curves drawn for the specimens impacted at 35 J are very consistent and demonstrates repeatability of the impact tests. The average delamination force is calculated as 3.3 kN while the predicted force for this layup is 5.4 kN. Therefore, the predicted delamination force is overestimated for $[0_4/90_4/0_2]_s$ GFRP specimens.

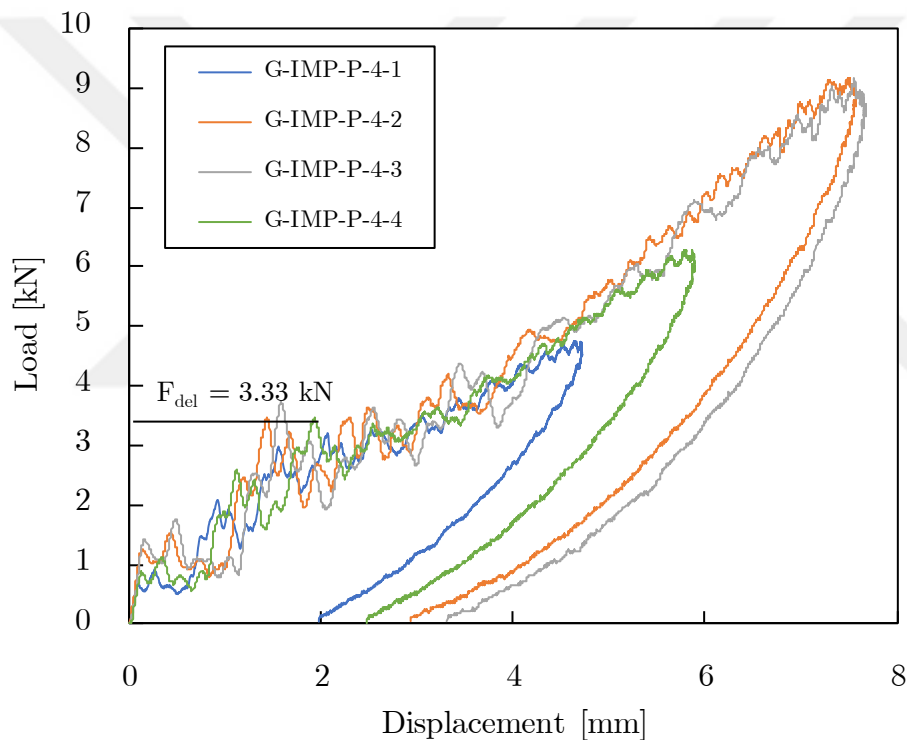
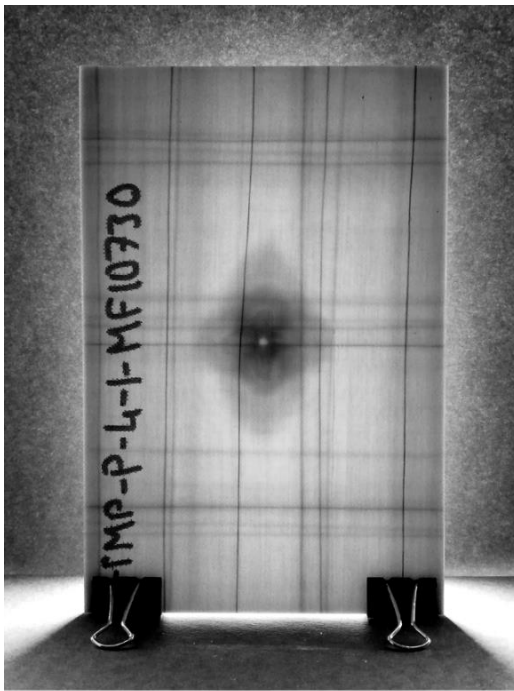


Figure 4.14. Load-displacement curves of $[0_4/90_4/0_2]_s$ GFRP specimens.

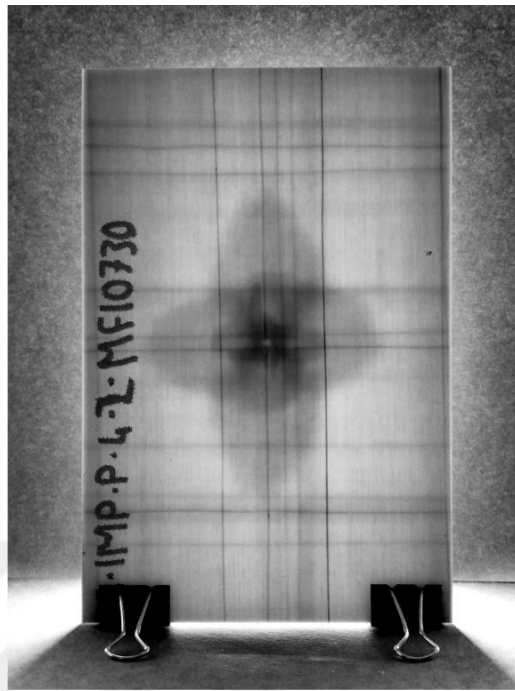
Figure 4.15 shows the post-mortem images of the main GFRP specimens of $[0_4/90_4/0_2]_s$ when kF values are equal to 1.5, 2.5, 2.5, 2 and the impact energy values are equal to 13 J, 35 J, 35 J, and 20 J, respectively. Figure 4.15b and Figure 4.15c show the delamination damage at the same impact energy value; therefore, the damage

area is very similar as expected. As the impact energy decreases gradually as shown in Figure 4.15d and Figure 4.15a, respectively, the damage area also decreases. The peanut shaped delaminations are observed in the fiber directions, 0° and 90° directions, and are wider along the longitudinal direction of the plate due to bending stiffness mismatching phenomenon. The darker regions Figure 4.15 show the overlapping 0° and 90° delamination areas.

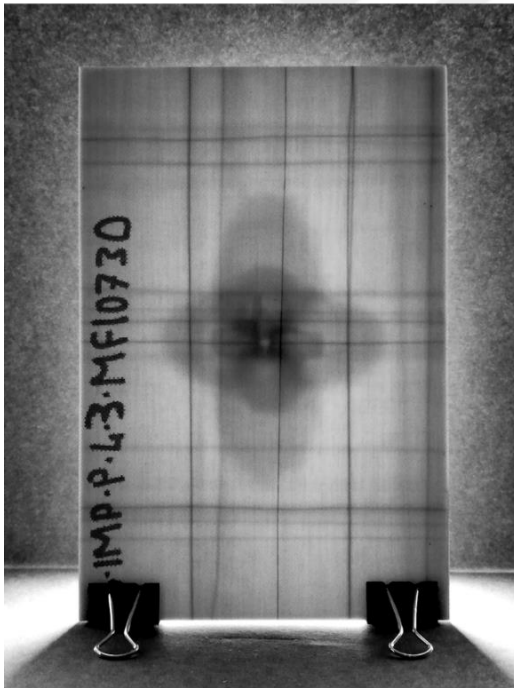




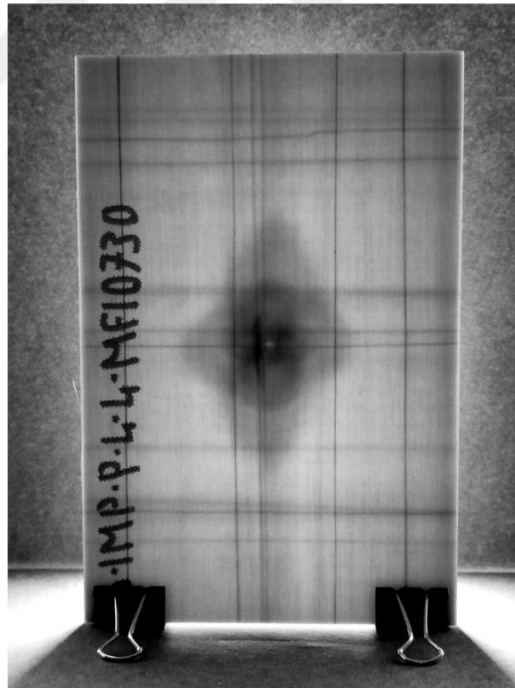
(a)



(b)



(c)



(d)

Figure 4.15. Post-mortem pictures of the main $[0_4/90_4/0_2]_S$ GFRP specimens of (a) $kF = 1.5$, (b) $kF = 2.5$, (c) $kF = 2.5$, (d) $kF = 2$.

4.4.2.2. $[0_8/90_2]_s$ GFRP Plates

Three $[0_8/90_2]_s$ GFRP specimens (named also G-IMP-5) are tested at 20 J, 20 J and 13 J. Since the test data could not be acquired for specimen G-IMP-P-5-1 due to the technical issues related to testing system, load vs. displacement curves of two $[0_8/90_2]_s$ GFRP specimens impacted at energies of 20 J and 13 J are presented in Figure 4.16. As seen in the Figure 4.16, the average delamination force for this layup is found 2.54 kN whereas the predicted value of this force is 5.05 kN. Similar to the results of $[0_4/90_4/0_2]_s$ GFRP specimens, the predicted delamination force is overestimated for $[0_8/90_2]_s$ GFRP specimens. Energies absorbed by plates along the impact event is 12.1 J and 7.6 J for 20 J and 13 J impacts, respectively.

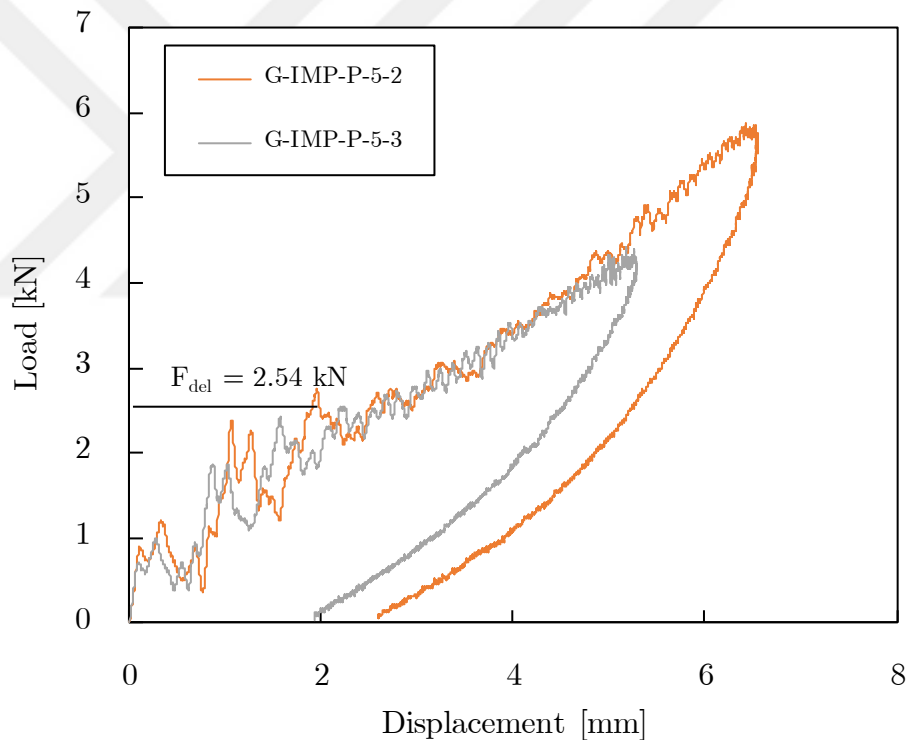


Figure 4.16. Load-displacement curves of $[0_8/90_2]_s$ GFRP specimens.

Figure 4.17 shows the post-mortem images of the main GFRP specimens of $[0_8/90_2]_s$ when kF values are equal to 2, 2, 1.5 and the impact energy values are equal to 20 J, 20 J, and 13 J, respectively. In Figure 4.17a and Figure 4.17b, plates are impacted at

the same energy values and the damage areas are similar. Figure 4.17c shows the delamination damage at a lower impact energy value; therefore, the damage area is smaller. The number of different angle ply interfaces are smaller than the C-IMP-P-4 set of specimens and it results in larger delamination areas when compared with the Figure 4.15. The peanut shaped delaminations are observed in the fiber directions, 0° and 90° directions, and are wider along the longitudinal direction of the plate due to bending stiffness mismatching phenomenon. Delaminations along different fiber directions overlaps at the edges in Figure 4.17 and these regions are observed to be darker.

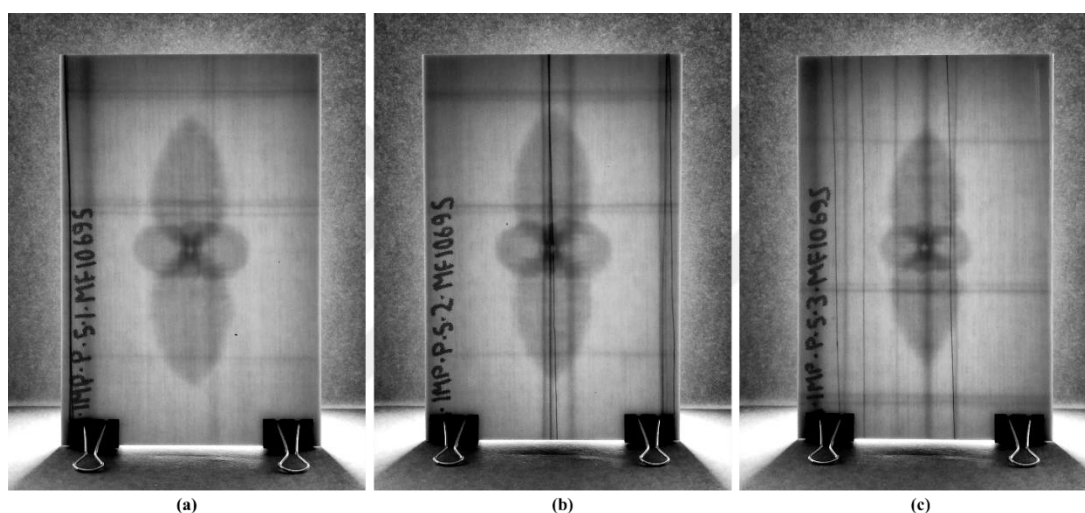


Figure 4.17. Post-mortem pictures of the main $[0_8/90_2]_S$ GFRP specimens of (a) $kF = 2$, (b) $kF = 2$, (c) $kF = 1.5$.

4.5. Conclusions

In this study, drop-weight impact tests conducted on CFRP and GFRP composite plates are presented. An analytical approach is used to determine the impact energies with the aim of creating a reasonable amount of impact damage in the plate. Non-destructive inspection results show that methodology followed for prediction of impact energies works properly. Following conclusions are made from the experimental results:

- Load-displacement responses of the same plates impacted at the same energy level show consistently that 3-D drop-weight impact tests are highly repeatable.
- The amount of force at which a significant delamination occurs depends only on the plate configuration and is independent from the impact energy in case of quasi-static impact.
- NDI results show that projected delamination area is larger under same impact energy for plates with less number of interfaces.
- Delaminations are wider in the same direction as of the fibers of the lower adjacent layer in accordance with the bending stiffness mismatching concept.

CHAPTER 5

NUMERICAL INVESTIGATION OF LOW-VELOCITY IMPACT DAMAGE IN COMPOSITE BEAMS AND PLATES

5.1. Introduction

In this study, drop-weight impact tests on composite plates are simulated. Impact tests of composite laminates are modeled in 3-D space. Impact simulation is conducted with explicit finite element analysis. In order to predict composite ply damage, intralaminar damage model is developed and implemented to ABAQUS/Explicit via a user-written subroutine VUMAT. Delamination damage is simulated using cohesive zone method. Damage initiation and propagation and final damage patterns are investigated comparing the results obtained in simulations with experimental results.

5.2. Numerical Method

In this section, the approach employed in the simulation of the impact induced damage in composite beams plates is described. Damage models used in the simulations are explained in detail. Modelling details of the virtual test setup are also discussed.

5.2.1. Intralaminar Damage Model

The intralaminar damage model predicting initiation and evolution of composite damage is developed based on continuum damage mechanics and is an extension of the 2-D model proposed by Maimi et al. [25] to 3-D. The model accounts for fiber and matrix damages in tension and compression modes.

5.2.1.1. Damage Initiation

Damage initiation in tensile fiber (*FT*), compressive fiber (*FC*), tensile matrix (*MT*) and compressive matrix (*MC*) modes are controlled by loading functions ϕ_N . When

the ϕ_N reaches unity, damage in corresponding mode initiates. Maximum stress and Hashin Failure Criteria [11] are used for longitudinal and transverse loading functions, respectively. Loading functions for each damage mode are given as

Longitudinal tensile mode (if $\sigma_{11} > 0$)

$$\phi_{FT} = \frac{\sigma_{11}}{X_T} \quad (5.1)$$

Longitudinal compressive mode (if $\sigma_{11} < 0$)

$$\phi_{FC} = -\frac{\sigma_{11}}{X_C} \quad (5.2)$$

Transverse tensile mode (if $\sigma_{22} + \sigma_{33} > 0$)

$$\phi_{MT} = \left(\frac{\sigma_{22} + \sigma_{33}}{Y_T}\right)^2 + \frac{\sigma_{23}^2 - \sigma_{22}\sigma_{33}}{S_{23}^2} + \left(\frac{\sigma_{12}}{S_{12}}\right)^2 + \left(\frac{\sigma_{13}}{S_{13}}\right)^2 \quad (5.3)$$

Transverse compressive mode (if $\sigma_{22} + \sigma_{33} < 0$)

$$\phi_{MC} = \left[\left(\frac{Y_C}{2S_{23}}\right)^2 - 1 \right] \frac{(\sigma_{22} + \sigma_{33})}{Y_C} + \left(\frac{\sigma_{22} + \sigma_{33}}{2S_{23}}\right)^2 + \frac{\sigma_{23}^2 - \sigma_{22}\sigma_{33}}{S_{23}^2} + \left(\frac{\sigma_{12}}{S_{12}}\right)^2 + \left(\frac{\sigma_{13}}{S_{13}}\right)^2 \quad (5.4)$$

Ply strengths are measured using ASTM test standards [49]-[51]. X_T and X_C are the longitudinal tensile and compressive strengths, respectively. Y_C is the transverse compressive strength. The value of the transverse tensile strength Y_T^{ud} and longitudinal shear strengths S_{12}^{ud} and S_{13}^{ud} measured by testing unidirectional specimens are meaningless for a ply in a multidirectional laminate, instead in-situ strengths Y_T , S_{12} and S_{13} are used. These strengths are calculated using the components of the fracture toughness and the ply elastic properties for thick, thin embedded and thin outer plies as shown through Eqs. (5.5) and (5.13) [28]. In calculation of in-situ shear strengths, material shear response is assumed linear.

For a thick ply

$$Y_T = 1.12\sqrt{2}Y_T^{ud} \quad (5.5)$$

$$S_{12} = \sqrt{2}S_{12}^{ud} \quad (5.6)$$

$$S_{13} = \sqrt{2}S_{13}^{ud} \quad (5.7)$$

For a thin group of embedded plies

$$Y_T = \sqrt{\frac{8G_{2+}}{\pi t \Lambda_{22}^0}} \quad (5.8)$$

$$S_{12} = \sqrt{\frac{8G_{12}G_6}{\pi t}} \quad (5.9)$$

$$S_{13} = \sqrt{\frac{8G_{13}G_6}{\pi t}} \quad (5.10)$$

For a thin group of outer plies

$$Y_T = 1.79 \sqrt{\frac{G_{2+}}{\pi t \Lambda_{22}^0}} \quad (5.11)$$

$$Y_T = 1.79 \sqrt{\frac{G_{2+}}{\pi t \Lambda_{22}^0}} \quad (5.12)$$

$$S_{13} = \sqrt{\frac{4G_{13}G_6}{\pi t}} \quad (5.13)$$

where t is the thickness of the group of plies, and G_{2+} and G_6 are components of fracture toughness associated with transverse failure in tension and in shear. Λ_{22}^0 is defined as

$$A_{22}^0 = 2 \left(\frac{1}{E_2} - \frac{\nu_{21}^2}{E_1} \right) \quad (5.14)$$

S_{12} and S_{13} are the same and equal to in-plane shear strength measured in standard tests. S_{23} is the transverse shear strength and is calculated as [28]

$$S_{23} = Y_C \cos \alpha_0 \left(\sin \alpha_0 + \frac{\cos \alpha_0}{\tan 2\alpha_0} \right) \quad (5.15)$$

where α_0 is the fracture angle under pure transverse compression loading and is determined through observation on a fractured unidirectional 90° specimen.

Thin-to-thick transition thickness depends on the material and it can be obtained by plotting the in-situ strength expressions for both thin and thick plies over a thickness value. As an example, Figure 5.1 shows the variation of in-situ transverse tensile and inplane shear strengths with thin ply and thick ply models over 1 mm ply thickness together with the unidirectional strengths. It is clearly seen that the transition thickness for this material is about 0.3 mm.

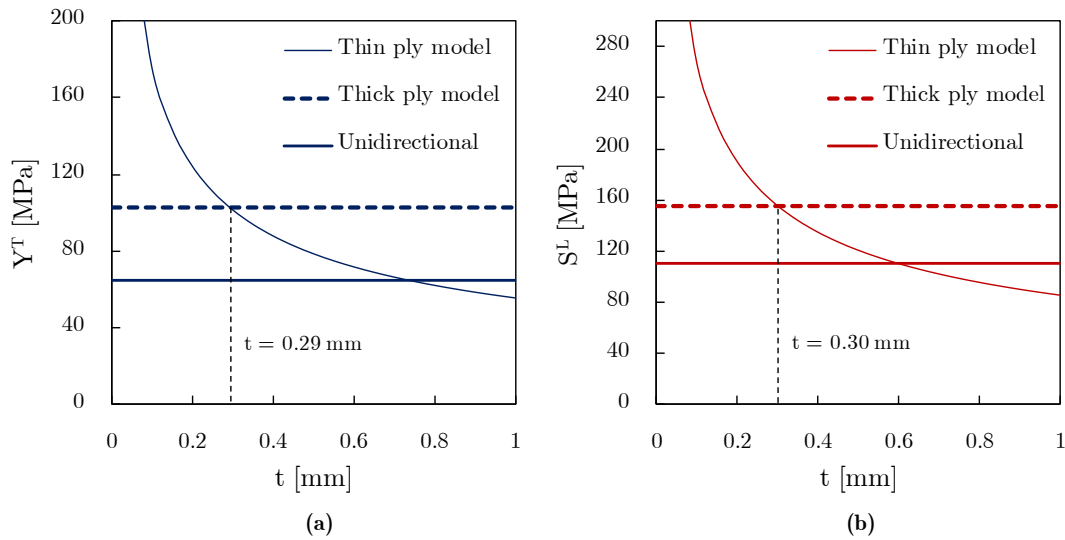


Figure 5.1. Variation of the in-situ (a) transverse tensile and (b) inplane shear strengths with thin ply and thick ply models over 1 mm ply thickness for 913 132 HTA UD Carbon Prepreg material.

Alternatively, one can calculate the correct in-situ strength for a prescribed material and stacking sequence without knowing the thin-to-thick transition thickness as follows

For an embedded ply

$$Y_T = \max \left(1.12\sqrt{2}Y_T^{ud}, \sqrt{\frac{8G_{2+}}{\pi t\Lambda_{22}^0}} \right) \quad (5.16)$$

$$S_{12} = \max \left(\sqrt{2}S_{12}^{ud}, \sqrt{\frac{8G_{12}G_6}{\pi t}} \right) \quad (5.17)$$

$$S_{13} = \max \left(\sqrt{2}S_{13}^{ud}, \sqrt{\frac{8G_{13}G_6}{\pi t}} \right) \quad (5.18)$$

For an outer ply

$$Y_T = \max \left(1.12\sqrt{2}Y_T^{ud}, 1.79 \sqrt{\frac{G_{2+}}{\pi t\Lambda_{22}^0}} \right) \quad (5.19)$$

$$S_{12} = \max \left(\sqrt{2}S_{12}^{ud}, \sqrt{\frac{4G_{12}G_6}{\pi t}} \right) \quad (5.20)$$

$$S_{13} = \max \left(\sqrt{2}S_{13}^{ud}, \sqrt{\frac{4G_{13}G_6}{\pi t}} \right) \quad (5.21)$$

5.2.1.2. Damage Evolution

Elastic domain threshold, r_N , is defined as

$$r_N = \begin{cases} 1 & \text{before damage initiation} \\ \phi_{N,max} & \text{after damage initiation} \end{cases} \quad N = FT, FC, MT, MC \quad (5.22)$$

where $\phi_{N,max}$ is the maximum value of ϕ_N in time history. Damage activation function, F_N , is expressed as

$$F_N = \phi_N - r_N \quad (5.23)$$

Regarding to definition of r_N , while the damage activation function is negative, material response is in elastic domain. Damage evolution occurs when F_N becomes zero.

The evolution of the damage is modelled by a linear softening response with equivalent stress-strain approach, shown in Figure 5.2. The area under the curve corresponds to the energy dissipated per unit volume and is defined as $g_N = G_{eq,c}^N/L^*$ where L^* is the characteristic length of finite element[52]. $G_{eq,c}^N$ is the equivalent fracture toughness for the damage mode N .

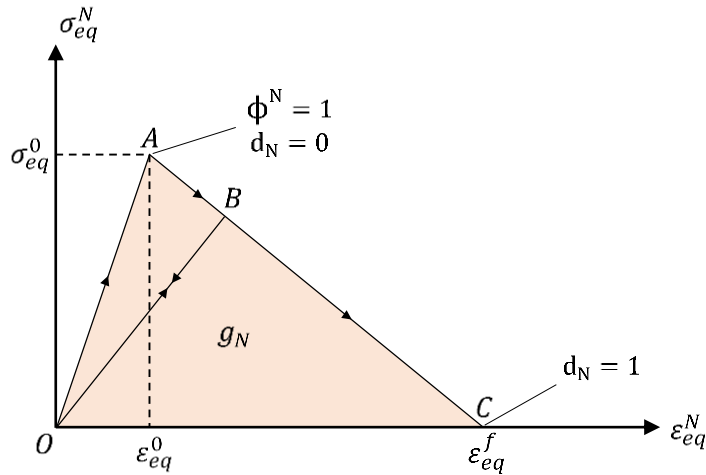


Figure 5.2. Linear softening response for ply material with equivalent stress-strain approach.

Equivalent fracture toughness expressions for each damage mode are given as

$$G_{eq,C}^{FT} = G_{1+} \quad (5.24)$$

$$G_{eq,C}^{FC} = G_{1-} \quad (5.25)$$

$$G_{eq,C}^{MT} = \left[\left(\frac{1}{G_{2+}} \frac{\langle \varepsilon_2^0 \sigma_2^0 \rangle}{\varepsilon_{eq}^{0,MT} \sigma_{eq}^{0,MT}} \right)^\eta + \left(\frac{1}{G_{2+}} \frac{\langle \varepsilon_3^0 \sigma_3^0 \rangle}{\varepsilon_{eq}^{0,MT} \sigma_{eq}^{0,MT}} \right)^\eta + \left(\frac{1}{G_6} \frac{\varepsilon_{12} \tau_{12}}{\varepsilon_{eq}^{0,MT} \sigma_{eq}^{0,MT}} \right)^\eta + \left(\frac{1}{G_6} \frac{\varepsilon_{13} \tau_{13}}{\varepsilon_{eq}^{0,MT} \sigma_{eq}^{0,MT}} \right)^\eta + \left(\frac{1}{G_6} \frac{\varepsilon_{23} \tau_{23}}{\varepsilon_{eq}^{0,MT} \sigma_{eq}^{0,MT}} \right)^\eta \right]^{-1/\eta} \quad (5.26)$$

$$G_{eq,C}^{MC} = G_6 / \cos(\alpha_0) \quad (5.27)$$

G_{1+} and G_{1-} are components of fracture toughness associated with longitudinal failure in tension and compression. G_{1+} and G_{1-} are measured using compact tension and compact compression tests developed by Pinho et al. [53]. G_{2+} and G_6 are components of fracture toughness associated with transverse failure in tension and in shear and can be measured performing standard double cantilever beam [36] and end-notched flexure tests [37] proposed by ASTM, respectively. α_0 is the fracture angle under pure transverse compression loading and is determined through observation on a fractured unidirectional 90° specimen. η is the mode interaction parameter and is found by least-square fit of the experimental values of the fracture toughness under different mixed-mode ratios [4] where mixed-mode bending test as proposed by Crews and Reeder [33] needs to be carried out. $\langle \ \rangle$ is the Macaulay bracket and is defined as $\langle a \rangle := (a + |a|)/2$.

Equivalent stress and strain expressions for corresponding damage modes are as follows

Longitudinal Tensile & Compressive Mode

$$\sigma_{eq}^{FT,FC} = |\sigma_{11}| \quad (5.28)$$

$$\varepsilon_{eq}^{FT,FC} = |\varepsilon_{11}| \quad (5.29)$$

Transverse Tensile & Compressive Mode

$$\sigma_{eq}^{MT,MC} = \frac{\langle \pm \sigma_{22} \rangle \langle \pm \varepsilon_{22} \rangle + \langle \pm \sigma_{33} \rangle \langle \pm \varepsilon_{33} \rangle + \tau_{12} \varepsilon_{12} + \tau_{13} \varepsilon_{13} + \tau_{23} \varepsilon_{23}}{\varepsilon_{eq}} \quad (5.30)$$

$$\varepsilon_{eq}^{MT,MC} = \sqrt{\langle \pm \varepsilon_{22} \rangle^2 + \langle \pm \varepsilon_{33} \rangle^2 + \varepsilon_{12}^2 + \varepsilon_{13}^2 + \varepsilon_{23}^2} \quad (5.31)$$

The term \pm in Eqs. (5.30) and (5.31) are taken + for tensile failure mode and - for compressive failure mode.

The damage variable d_N shows a non-linear saturation type behavior to provide the linear softening response of damaged material and it is expressed as

$$d_N = \frac{\varepsilon_{eq}^f (\varepsilon_{eq}^{max} - \varepsilon_{eq}^0)}{\varepsilon_{eq}^{max} (\varepsilon_{eq}^f - \varepsilon_{eq}^0)} \quad (5.32)$$

where ε_{eq}^0 and ε_{eq}^f are the equivalent strains at the initiation of damage and complete failure, respectively. The maximum value of equivalent strain, in time history, ε_{eq}^{max} , is used to satisfy $\dot{d}_N \geq 0$ condition. Damaged compliance tensor, $\underline{\underline{H}}$, is

$$\underline{\underline{H}} = \begin{bmatrix} \frac{1}{E_1(1-d_F)} & -\frac{\nu_{12}}{E_1} & -\frac{\nu_{13}}{E_1} & 0 & 0 & 0 \\ -\frac{\nu_{12}}{E_1} & \frac{1}{E_2(1-d_M)} & -\frac{\nu_{23}}{E_2} & 0 & 0 & 0 \\ -\frac{\nu_{13}}{E_1} & -\frac{\nu_{23}}{E_2} & \frac{1}{E_3(1-d_M)} & 0 & 0 & 0 \\ 0 & 0 & 0 & \frac{1}{G_{12}(1-d_S)} & 0 & 0 \\ 0 & 0 & 0 & 0 & \frac{1}{G_{13}(1-d_S)} & 0 \\ 0 & 0 & 0 & 0 & 0 & \frac{1}{G_{23}(1-d_S)} \end{bmatrix} \quad (5.33)$$

The closure of transverse and longitudinal cracks under load reversal is taken into account by defining two separate damage variables for tension and compression, d_T and d_C , for both longitudinal and transverse damage modes. The active damage mode is determined by following d_F and d_M definitions[25], [26].

$$d_F = d_{FT} \frac{\langle \sigma_{11} \rangle}{|\sigma_{11}|} + d_{FC} \frac{\langle -\sigma_{11} \rangle}{|\sigma_{11}|} \quad (5.34)$$

$$d_M = d_{MT} \frac{\langle \sigma_{22} \rangle}{|\sigma_{22}|} + d_{MC} \frac{\langle -\sigma_{22} \rangle}{|\sigma_{22}|} \quad (5.35)$$

$$d_S = 1 - (1 - d_{MT})(1 - d_{MC}) \quad (5.36)$$

5.2.2. Interlaminar Damage Model

The interlaminar damage model used in the analysis to simulate delamination damage is the one offered by ABAQUS software and is based on a NASA report [29]. Fracture mechanics based bilinear traction-separation response, seen in Figure 5.3, is assigned to each cohesive element. Since delamination is usually caused by multi-axial stress state subjecting to the interface, mode-mixity is taken account when modeling the cohesive material response.

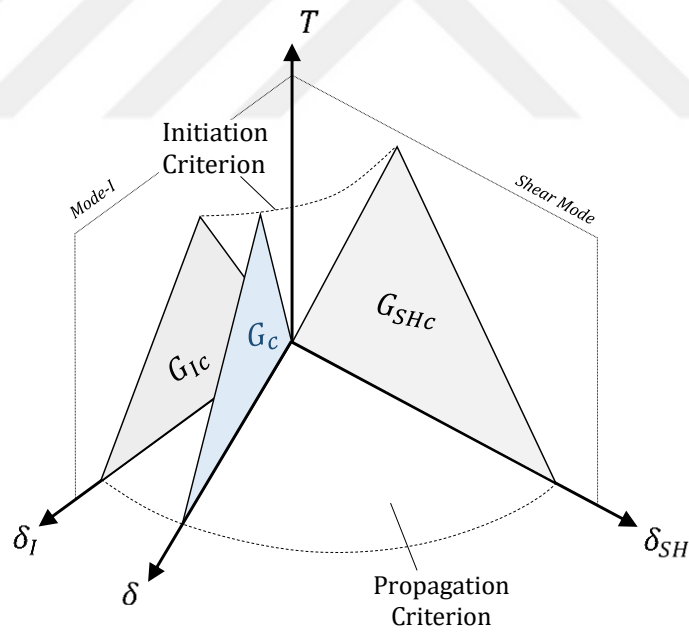


Figure 5.3. Mixed-mode bilinear traction-separation response of cohesive material.

The initial response of the cohesive element is assumed to be linear until a damage initiation where the slope of the line is called penalty stiffness, K_i ($i = I, II, III$). The value of the penalty stiffness must be high enough to prevent interpenetration of the crack faces and to prevent artificial compliance from being introduced into the model by the cohesive elements. However, an overly high value can lead to numerical problems [54].

Turon, et al. [55] proposed an equation for the penalty stiffness for Mode I that ensures that the compliance of the bulk material is much larger than the initial compliance of the cohesive element, as follows

$$K_I = c \frac{E_3}{t} \quad (5.37)$$

where t is the half-laminate thickness and c is a parameter much larger than 1 and $c = 50$ is proposed by Turon et al. which is sufficiently accurate for most problems [55]. Relation between mode I and shear mode interface stiffnesses is proposed by Turon et al. [56] as

$$K_{II} = K_{III} = K_I \frac{G_{Ic}}{G_{IIc}} \left(\frac{T_{o,II}}{T_{o,I}} \right)^2 \quad (5.38)$$

where G_{Ic} and G_{IIc} are mode I and shear mode components of fracture toughness and $T_{o,I}$ and $T_{o,II}$ are the interface strengths in mode I and shear mode.

Initiation of interlaminar damage is controlled by quadratic nominal stress criterion which is given as

$$\left(\frac{\langle T_I \rangle}{T_{o,I}} \right)^2 + \left(\frac{T_{II}}{T_{o,II}} \right)^2 + \left(\frac{T_{III}}{T_{o,III}} \right)^2 = 1 \quad (5.39)$$

In this equation, T_i and $T_{o,i}$ ($i = I, II, III$) are the tractions applying to the surface and interlaminar strengths for corresponding fracture modes, respectively. $T_{o,I}$ is measured in four-point bending test of a curved unidirectional specimen [34] and $T_{o,II}$ is

measured in a short-beam shear test [35]. $T_{o,III}$ can be assumed to be equal to $T_{o,II}$. In case of mode I, only positive traction is included in initiation criteria because compressive normal stresses do not contribute to opening fracture.

Once interlaminar damage initiates, Benzeggagh-Kenane (B-K) criterion is used for modeling mixed-mode propagation of damage [32]. The criterion is given as

$$G_c = G_{Ic} + (G_{SHc} - G_{Ic}) \left(\frac{G_{SH}}{G_T} \right)^\eta \quad (5.40)$$

where G_{SH} and G_T refer to sum of work done by shear mode tractions and by all pure mode tractions, respectively, as shown below.

$$G_{SH} = G_{II} + G_{III} \quad (5.41)$$

$$G_T = G_I + G_{II} + G_{III} \quad (5.42)$$

G_{Ic} is mode I fracture toughness which is measured in a double cantilever beam test [36]. G_{SHc} is defined as $G_{SHc} = G_{IIc} = G_{IIIc}$ and is measured in an end-notched flexure test [37]. η is the mode interaction parameter and is found by least-square fit of the experimental values of the fracture toughness under different mixed-mode ratios [4] where mixed-mode bending test needs to be carried out.

Linear softening response is defined to the cohesive elements in the plane where damage initiation occurs. The cohesive damage variable d shows a non-linear saturation type behavior to provide the linear softening response of damaged cohesive elements and is defined as

$$d = \frac{\delta_{eq}^f (\delta_{eq}^{max} - \delta_{eq}^0)}{\delta_{eq}^{max} (\delta_{eq}^f - \delta_{eq}^0)} \quad (5.43)$$

where δ_{eq}^0 and δ_{eq}^f are the equivalent displacements at the initiation of damage and complete failure, respectively. The maximum value of equivalent displacement, in time history, δ_{eq}^{max} , is used to satisfy irreversibility ($\dot{d} \geq 0$) condition.

5.2.3. Virtual Test Setup

To simulate low-velocity impact experiments on composite plates, three-dimensional finite element model is generated in ABAQUS/Explicit. The model consists of a 3-D deformable composite plate of $150 \times 100 \text{ mm}^2$, a rigid fixture base having a $125 \times 75 \text{ mm}^2$ window, four rigid cylindrical clamps with 10 mm diameter and a rigid semi-spherical impactor with 16 mm diameter. The assembly of the virtual test setup consisting of these parts is shown in Figure 5.4.

$[0_8/90_2]_s$ composite plate of which the geometry is shown in Figure 5.4 is modeled as a three dimensional deformable solid body. The plate consists of 20 unidirectional composite layers having equal thicknesses of 0.125 mm. In the model, clustered plies are considered as a single homogenized thick ply.

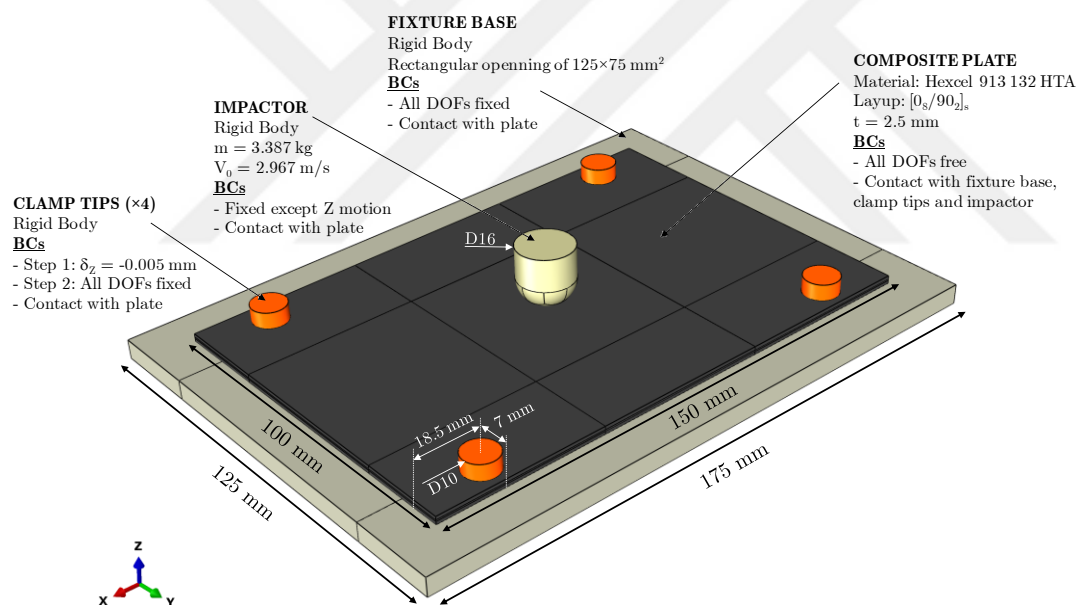


Figure 5.4. Geometry and boundary conditions of the virtual impact test setup.

Composite plate model is presented in Figure 5.5 with the details of the mesh and the materials defined to the finite elements. Plate geometry is meshed with 8-noded linear brick elements with reduced integration and hourglass control (C3D8R in ABAQUS library). Each two ply of composite beam is modeled with one element in through-

the-thickness direction. In-plane mesh size is set variable to reduce the computational cost. A central region of $50 \times 50 \text{ mm}^2$ including the impact zone is meshed uniformly with elements of $0.25 \times 0.25 \times 0.25 \text{ mm}^3$. A biased mesh is used outside of this region such that each element has a 1.1 times greater element size than the previous one while going towards plate boundaries. Material model accounting initiation and propagation of composite ply damage is defined to the finite elements in the central zone while only elastic behavior is found adequate for the remaining elements (see Figure 5.5). In order to prevent unrealistic element deformations due to numerical issues, enhanced hourglass control is introduced to the finite elements of the plate. Additionally, distortion of the elements is limited to the 10% of the original size for preventing excessive distortion due to the issues like negative element volume or material degradation.

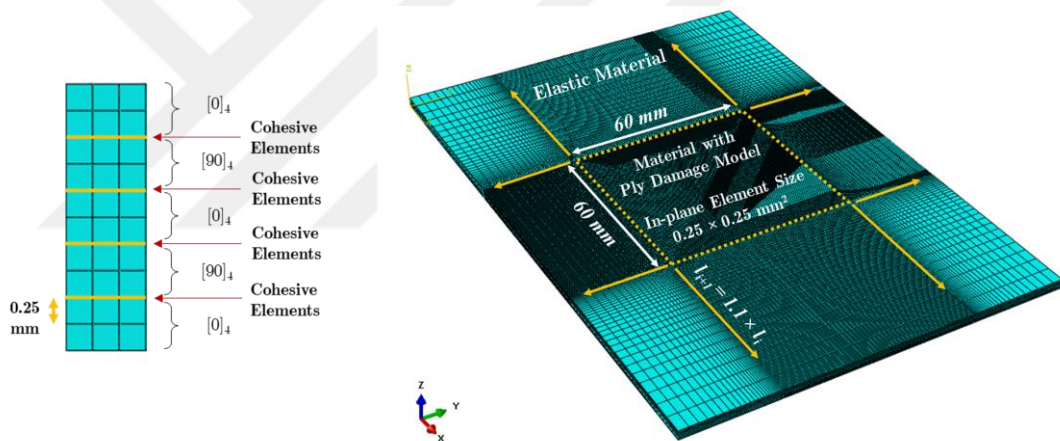


Figure 5.5. Composite plate model showing the details of the mesh and the materials defined to the finite elements.

Cohesive regions are modeled at interfaces of plies with different orientations inside the central region and are composed of $0.25 \times 0.25 \text{ mm}^2$ cohesive elements with zero thickness. Carbon/epoxy material of which the mechanical and interface properties are given in Table 5.1 and Table 5.2 is used as the ply material of composite beam in the analysis.

Table 5.1. Mechanical properties of carbon/epoxy material of plates.

Density	1520 kg/m^3
Elastic	$E_1 = 140 \text{ GPa}; E_2 = 9 \text{ GPa}; E_3 = 9 \text{ GPa}$ $\nu_{12} = 0.35; \nu_{13} = 0.35; \nu_{23} = 0.48$ $G_{12} = 5 \text{ GPa}; G_{13} = 5 \text{ GPa}; G_{23} = 4 \text{ GPa}$
Strength	$X_T = 2000 \text{ MPa}; X_C = 1500 \text{ MPa}$ $Y_T^{ud} = 65 \text{ MPa}; Y_C = 220 \text{ MPa}$ $S_{12}^{ud} = 110 \text{ MPa}; S_{13}^{ud} = 110 \text{ MPa}; S_{23} = 83 \text{ MPa};$
Toughness	$G_{I+} = 81500 \text{ N/m}; G_{I-} = 106300 \text{ N/m}$ $G_{2+} = 270 \text{ N/m}; G_6 = 570 \text{ N/m}$

Table 5.2. Interface properties of carbon/epoxy material of plates.

Interface strength	$T_{o,I} = 65 \text{ MPa}; T_{o,II} = T_{o,III} = 110 \text{ MPa}$
Fracture toughness	$G_{I,c} = 270 \text{ N/m}; G_{II,c} = 570 \text{ N/m}$
B-K criterion constant	$\eta = 1.45$
Penalty stiffness	$K_I = 3.6 \times 10^{14} \text{ N/m}^3; K_{II} = K_{III} = 4.9 \times 10^{14} \text{ N/m}^3$

Fixture base, which is a rectangular steel part having a rectangular window of $125 \times 75 \text{ mm}^2$, is modeled as a discrete rigid body using with outer dimensions seen in Figure 5.4. A total of 1220 Quadratic rigid elements (R3D4 in ABAQUS library) are used for discretization of the fixture base. All degrees of freedoms of the reference point associated with the fixture base are constrained in accordance with the standard experiment. In the assembly, the composite plate is located on the fixture base. Four discrete rigid clamps are positioned on the top surface of the plate at the start of the simulation, as seen in Figure 5.4. Rigid clamps are also discretized using quadratic rigid elements (R3D4).

Hemi-spherical steel impactor is modeled as a discrete rigid body with 16 mm diameter and 3.387 kg mass. The discretization of the hemi-spherical impactor is made by spherified cube method and quadratic rigid elements (R3D4) are used. An initial velocity of 2.976 m/s corresponding to a 15 J impact is given to the impactor and it is located above the center of the composite plate. All degree of freedoms of the impactor except translation in vertical direction are restricted.

In the model, different contact interactions are defined between mating parts using general contact algorithm of the ABAQUS/Explicit: (i) between the impactor and top surface of the plate, (ii) between the bottom surface of the plate and top surface of the fixture base, (iii) between the clamp tips and the top surface of the plate, and (iv) inside the beam. The reason why a contact is defined inside the beam is opposing free surfaces form at the interfaces following a delamination damage. In all cases, hard contact with separation allowance is defined for interactions in normal direction. For tangential motion, contact is defined with Coulomb friction model with friction coefficients 0.3 and 0.5 for metal-to-composite and composite-to-composite contacts, respectively. Rough contact is assumed between the rubber clamp tip and the composite plate meaning that no relative tangential motion occurs between these parts.

During the analysis, following techniques are applied to the model to improve computational efficiency:

- Enhanced hourglass control option of the ABAQUS/Explicit is enhanced.
- Distortion control is applied to prevent excessive distortion or negative element volumes.
- Element deletion is activated to remove an element from the mesh when the its damage variables reach predefined values.
- Mass scaling is introduced to the elements whose stable time increment reduces under a predefined value. This value is determined such that the change in the mass of the plate is less than 1%.

The analysis consists of two consequent solution steps. In the first step, with the aim of squeezing the plate between the fixture base and the clamps, rigid clamps are moved 0.005 mm downward with a smooth step during 0.0001 s. The resultant reaction force in each clamp is measured about 2700 N which is more than twice of the minimum clamping force specified in ASTM D7136 standard [46]. During the second solution step of the analysis, clamps are held stationary and the impactor moves downward with constant velocity until the initial contact between the impactor and the plate occurs. Analysis of the impact event is performed following the initial contact.

5.3. Numerical Results

Finite element analysis of the 15 J - impact experiment on the $[0_4/90_4/0_2]_s$ CFRP plate specimen was performed in a high performance workstation using 30 central processing unit. The analysis ran using 30 CPUs for 3 days until it was terminated 5 milliseconds after the initial contact due to the rebound of the impactor. In this section, results obtained from the finite element analysis are presented.

5.3.1. Impact Dynamics

Displacement vs. time, load vs. time and load vs. displacement curves obtained from the simulation is seen in Figure 5.6a, b, and c, respectively. In Figure 5.6a, displacement of impactor increases until it becomes constant around $t = 4.1 \text{ ms}$. At this instant, impactor reaches its maximum displacement which is around 5.5 mm.

Figure 5.6b shows that the time history of the load acting on the impactor. The first load drop occurs at $t = 0.08 \text{ ms}$. The fact that the load drops sharply may indicate that whether a significant delamination occurs inside the plate or an artificial high stiffness exists at the initial contact. Since the time is too early for the former one, the latter possibility should be considered. After this drop, the load continues to increase encountering with tiny drops until $t = 0.54 \text{ ms}$ while the impact load reads 4.06 kN. From $t = 0.54 \text{ ms}$ to 0.62 ms impact load decreases down to 2.61 kN. Impact load increases up to 3.1 kN at $t = 1.1 \text{ ms}$ and starts to decrease in a wavy form from this point on. The load vs. displacement curve of the simulated virtual test is seen in Figure

5.6c. The load corresponding to the maximum displacement of the impactor is about 1.6 kN.

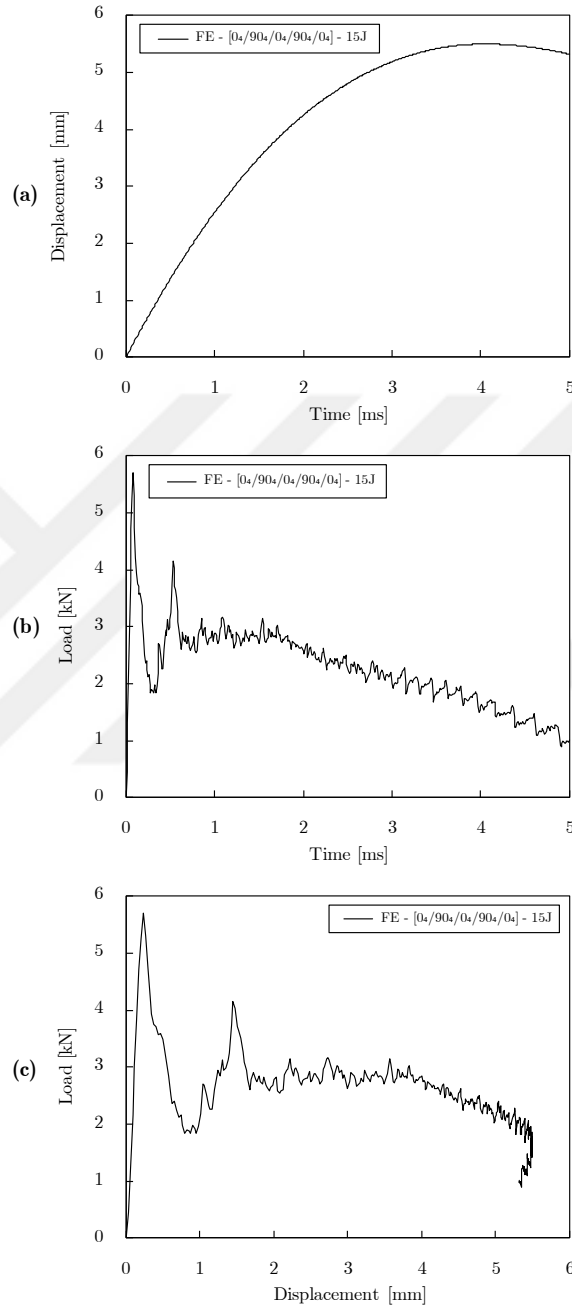


Figure 5.6. (a) Displacement vs. time, (b) load vs. time, and (c) load vs. displacement curves from the finite element analysis of $[0_4/90_4/0_2]_s$ CFRP plate specimen under 15 J - impact.

5.3.2. Ply Damage

Figure 5.7 shows the matrix damage distribution under the impact zone at different contact times (t_i). One quarter of the plate is removed for clear visualization of the damage states in both y-z and x-z planes under the impactor. The sequence of the damage process can be summarized as follows

- The first frame is taken at $t_i = 0$ at which the initial contact between the impactor and the beam happens.
- At $t_i = 0.06 \text{ ms}$, initial matrix crack forms in the bottom layers where the maximum elongation due to bending occurs. This form of the failure is similar to the one observed in the line impact experiments of $[90/0]_s$ beams. Although the stacking sequence of the plate is $[0_4/90_4/0_2]_s$ in the plate coordinate system, matrix cracking of the bottom plies is expected initial failure mode independent from the stacking sequence due to the spherical shape of the impactor, the plate geometry and the boundary conditions. It should also be noted that the cross-section of the $[0_4/90_4/0_2]_s$ plate in y-z plane is same as that of a $[90/0/90]_s$ beam.
- At $t_i = 0.13 \text{ ms}$, the initial matrix crack propagates in the bottom group of 0° plies. A damaged region starts to form in the lowermost ply of the laminate. Some shear and bending cracks and delaminations are also observed through the thickness of the plate.
- At $t_i = 0.30 \text{ ms}$, the initial matrix crack propagates in the bottom ply along the principal axis of the plate. Delamination initiation is completed at all $0/90$ interface at this instant. Additionally, matrix damage occurs in the top 0° plies around the boundary of the contact between the impactor and the plate.
- At $t_i = 0.40 \text{ ms}$, further matrix crack propagation is observed in the bottom ply along the principal axis of the plate.
- At $t_i = 1.00 \text{ ms}$, matrix damage in the bottom ply expands out from the impact zone. A significant increase in sizes of the existent delaminations in two interfaces of the beam are observed in this frame.

- At $t_i = 2.00 \text{ ms}$, the existent matrix damage and delaminations grows outwards from the center of the plate. Multiple vertical matrix cracks occur in the top 0° plies. It can be observed that delamination growth occurs mainly in the orientation of the bottom layer.
- The last frame shows the distribution of the complicated matrix damage state inside the laminate when the impactor reaches the maximum displacement at $t_i = 4.10 \text{ ms}$.

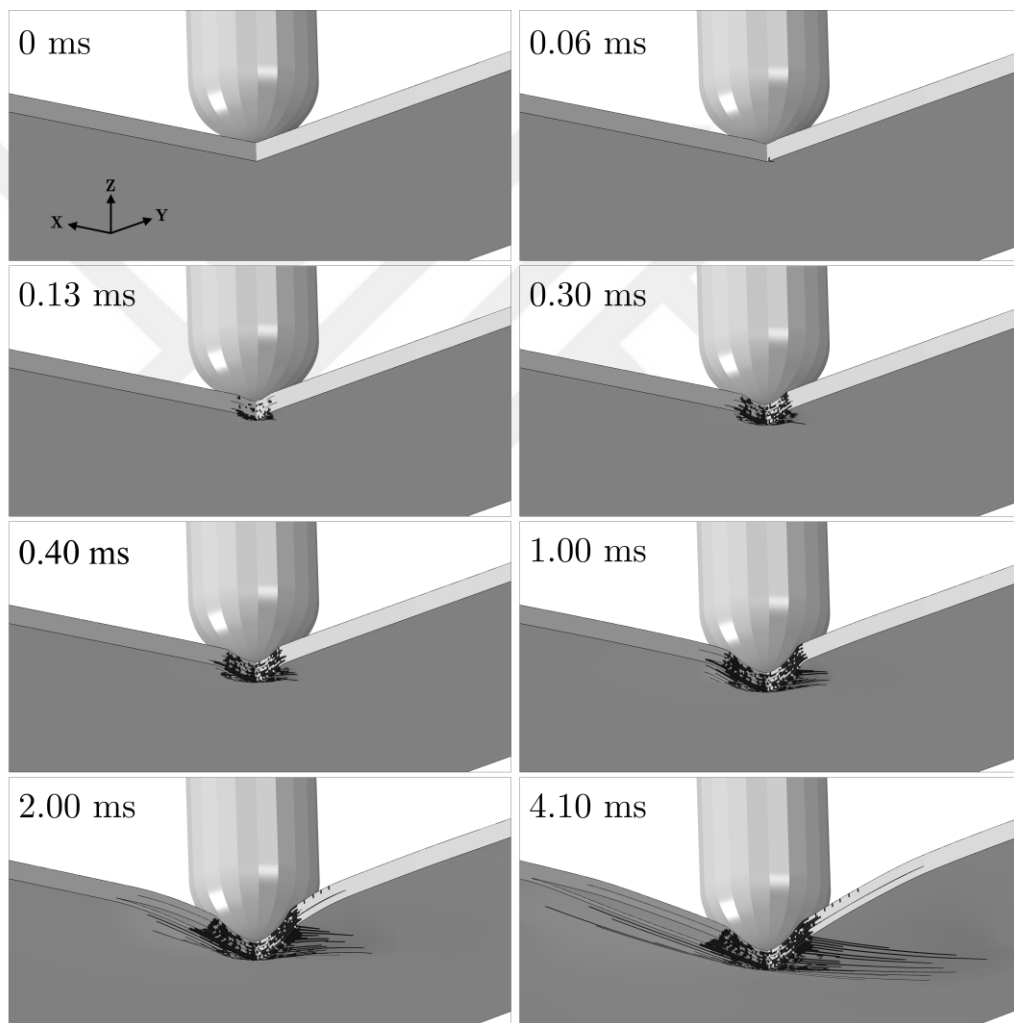


Figure 5.7. Through-the-thickness views matrix damage distribution under the impact zone at different contact times (Images are taken with multiple cut planes: x-z and y-z).

Figure 5.8a and b show the impact footprint and the backface cracks at the end of the analysis ($t_i = 5.00 \text{ ms}$) in the $60 \times 60 \text{ mm}^2$ region where composite ply damage model is assigned. It should be noted that this figure reflects the post-mortem damage state of the plate, since the analysis is terminated after rebound of the impactor. However, a visual correlation can be made between the Figure 5.8. and the tested plates.

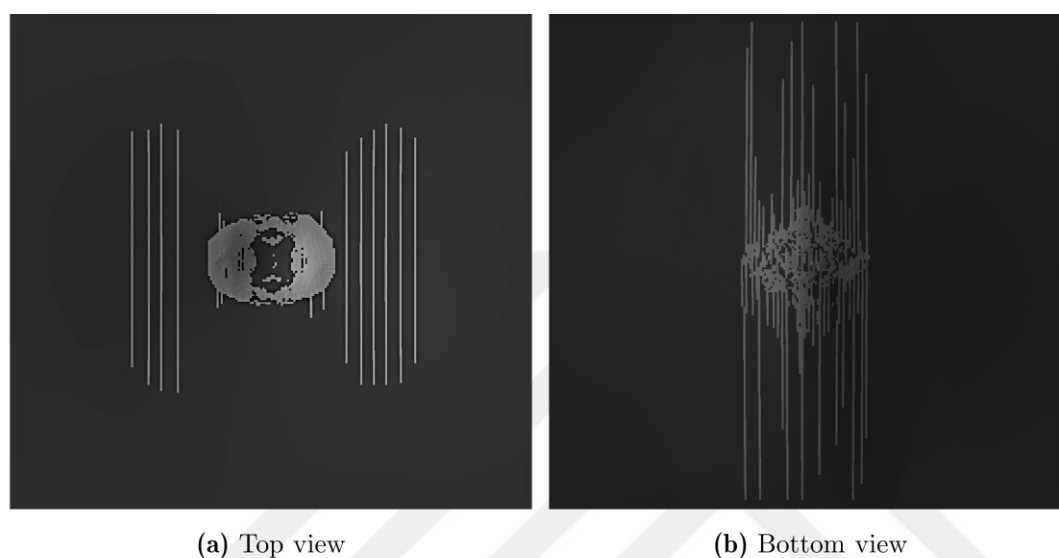


Figure 5.8. Simulated footprints on the (a) top and (b) bottom surfaces of the plate at the end of the analysis.

5.3.3. Delamination

Figure 5.9 shows the delamination damage at the end of the analysis ($t_i = 5.00 \text{ ms}$) at each four 0/90 interfaces starting from the uppermost. The pictures encircle the $100 \times 100 \text{ mm}^2$ central region of the plate. Results show that delaminations propagate in the same direction as of the fibers of the lower adjacent ply.

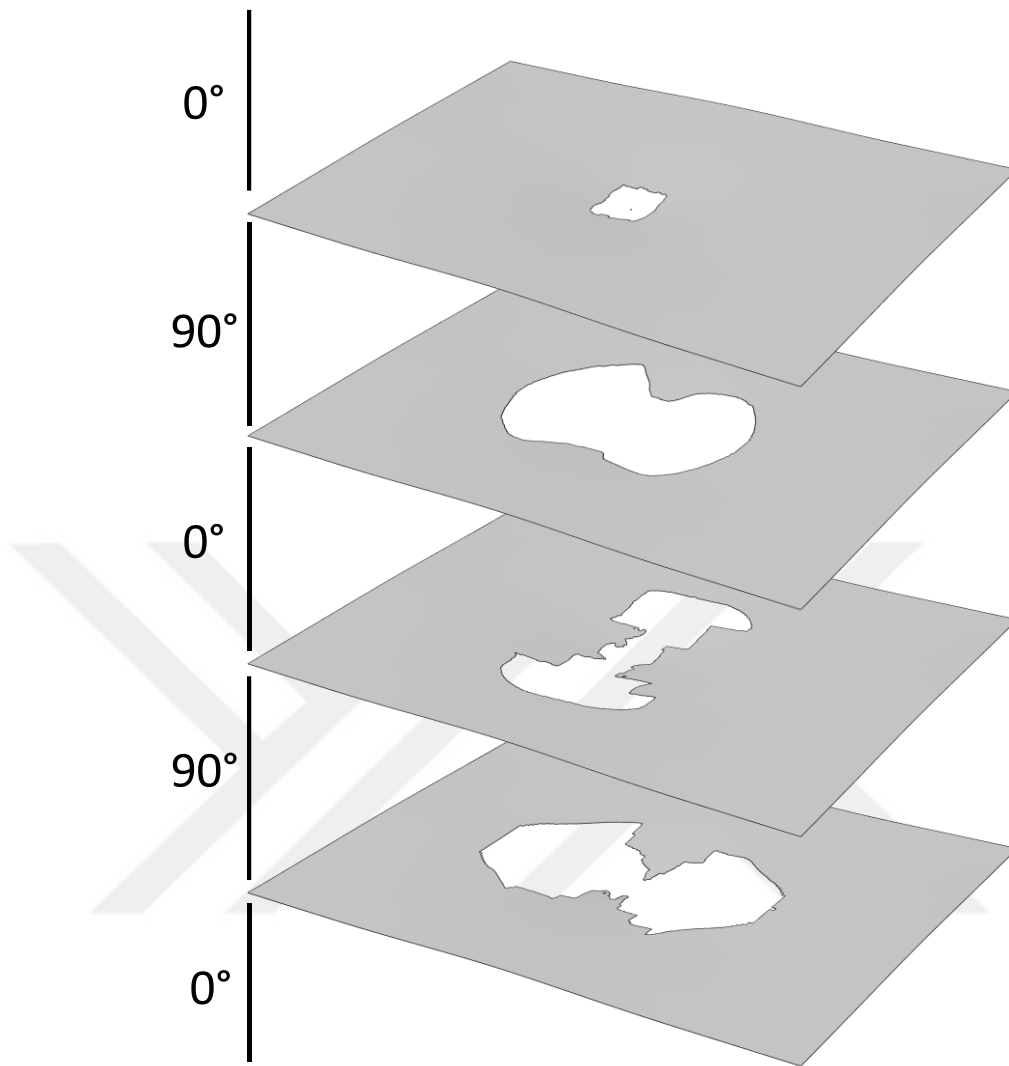


Figure 5.9. Delamination damage at 0/90 interfaces of the laminate at the end of the simulation ($t_i = 5.00 \text{ ms}$).

5.4. Conclusions

In this study, a virtual impact test setup was modeled and finite element analysis of the 15 J – impact event on the $[0_4/90_4/0_2]_s$ CFRP plate specimen was conducted in ABAQUS/Explicit. A material model accounting matrix and fiber failure modes of the composites was developed and implemented into the model via a user-written

subroutine VUMAT. Delamination damage in the plate was simulated by inserting cohesive elements at the interfaces of plies with different orientations.

The results of the analysis show that the initial failure mechanism is the matrix cracking in the lowermost plies independent from the stacking sequence of the laminate. Although matrix cracking does not lead to a considerable drop in the impact load, it should be taken into account in the analyses since it promotes formation of delamination which is one of the most energy dissipative failure modes of composites. It is also observed that delaminated regions expand in the same direction as of the fibers of the lower adjacent layer in accordance with the bending stiffness mismatching concept.

Figure 5.10 compares the projected delaminations in the experiment and the simulation. Although overall projected delaminated area is larger in case of simulations, a good agreement was obtained in terms of the extent of the delamination in the direction of plate length. Figure 5.11 shows the impact damage footprints and backface damages obtained in the experiment and the simulation. Simulation results which are captured while rebound of the impactor happens at a contact time of 5.0 ms are in good qualitative correlation with the post-mortem experimental results.

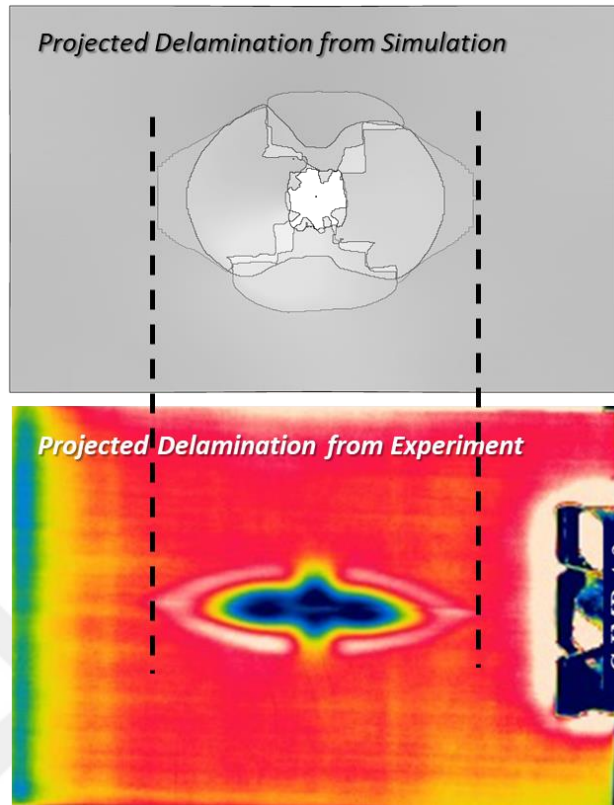


Figure 5.10. Comparison of the projected delaminations obtained in the 15 J experiment on $[0_4/90_4/0_2]_s$ CFRP plate and its simulation.

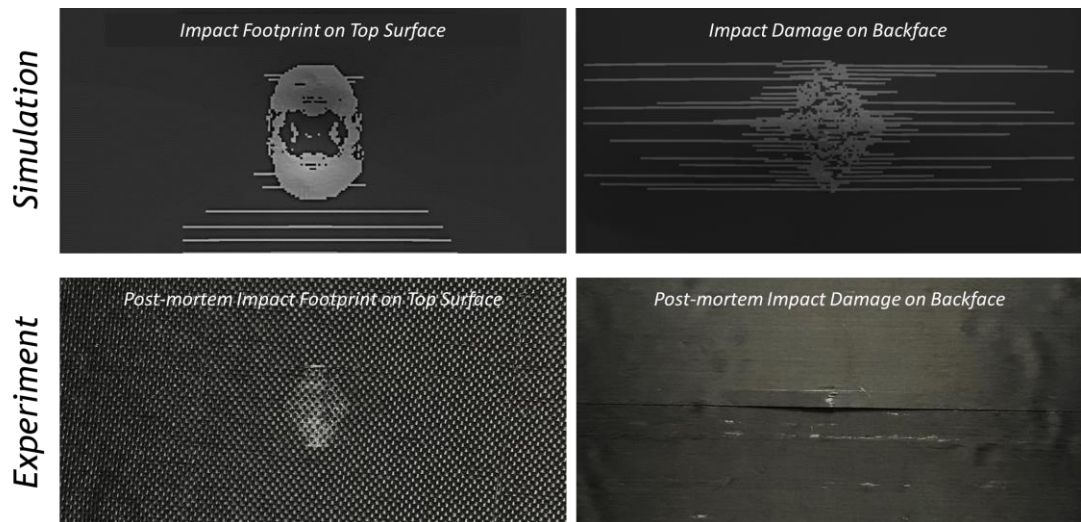


Figure 5.11. Comparison of impact footprint on top surface of the plate and impact damage in on backface obtained in the simulations and experiments.



CHAPTER 6

CONCLUSIONS

6.1. Summary of the Thesis

In this thesis, transverse impact induced damage process in composite beams and plates were investigated experimentally and numerically. The objective was to understand the impact induced damage mechanisms in composite laminates made of unidirectional preregs and to create high-fidelity simulation models. For this purpose, two consequent studies were conducted in this thesis. In the first part of the study, impact induced damage in composite beams was investigated. 2-D line impact experiments were conducted for making in-situ observation of damage process possible. Simulations of the experiments were carried out using a finite element method. Composite ply and interface damages were modeled using continuum damage mechanics based material models and cohesive zone method, respectively. In the second part of the study, impact induced damage in composite plates was investigated. Standard-like drop-weight impact tests were carried out on CFRP and GFRP plate laminates having different stacking sequences. Post-mortem damage pattern in the plates were analyzed via various non-destructive inspection methods. For simulating these tests, a virtual drop-weight impact test setup was created in ABAQUS/Explicit finite element tool. Damage modelling techniques validated in the first part of the study are implemented into the finite element model to simulate composite ply damage and delaminations. A good agreement was obtained between experimental and numerical results in terms of form of the final damage pattern.

6.2. Conclusions of the Study on Composite Beams

For conducting impact experiments on beams, a drop-weight low-velocity impact setup was designed and built. Impact tests were carried out on $[0/90]_s$ and $[90/0]_s$ beam laminates at several impact energies. Damage processes in the beams were captured

via the ultra-high-speed camera. Delamination tip speeds were calculated by differentiating the crack tip position data obtained by visual assessment. Strain fields on the side of the specimen were calculated using digital image correlation method. The main conclusions of the beam impact experiments can be summarized as

In $[0/90]_s$ CFRP beams,

- Under both static and dynamic flexural loading, dynamic failure propagation is observed.
- Delamination tip speeds are found to be 850 m/s in both static and impact tests.
- Experimental data consisting of the crack tip history and speed can be used as a benchmark for the simulations.

In $[90/0]_s$ CFRP beams,

- Initial failure mechanism is vertical matrix crack formation below the impact line in the bottom 90° layers and near the clamps in the top 90° layers.
- These matrix cracks nucleate delaminations which propagate at slow rates.

Simulations of the experiments were carried out using finite element method. 3-D model of the 2-D line impact model was generated in ABAQUS/Explicit. A continuum damage mechanics based composite ply damage was developed and implemented to the finite element tool via the user-written subroutine VUMAT of the previous study [9]. Delamination damage was simulated by inserting cohesive elements at the interfaces of plies having different orientations. Results of the finite element simulations of 2-D line impact event showed that

- CDM based material model is able to predict the form, initiation location and time of matrix cracks in both $[0_5/90_3]_s$ and $[90_5/0_3]_s$ CFRP beams.
- Delamination propagation speeds are overestimated with given material properties.
- Dynamic values of interface properties can have an effect on the accuracy of dynamic failure simulations.

- Implementing a 1 mm asymmetry into the model, a time delay of 120 μs is induced between the matrix cracks on each side of the $[0_5/90_3]_s$ beam, in better agreement with the experimental observations.

6.3. Conclusions of the Study on Composite Plates

Drop-weight impact tests were conducted on CFRP and GFRP composite plates. An analytical approach was used to determine the impact energies with the aim of creating a reasonable amount of impact damage in the plate. Non-destructive inspection results show that methodology followed for prediction of impact energies works properly. Following conclusions are made from the experimental results:

- Load-displacement responses of the same plates impacted at the same energy level show consistently that 3-D drop-weight impact tests are highly repeatable.
- The amount of force at which a significant delamination occurs depends only on the plate configuration and is independent from the impact energy in case of quasi-static impact.
- NDI results show that projected delamination area is larger under same impact energy for plates with less number of interfaces.
- Delaminations are wider in the same direction as of the fibers of the lower adjacent layer in accordance with the bending stiffness mismatching concept.

Simulation of the 15 J – impact event on the $[0_4/90_4/0_2]_s$ CFRP plate was conducted in ABAQUS/Explicit. A material model accounting matrix and fiber failure modes of the composites with Hashin failure initiation criteria was developed and implemented into the model via a user-written subroutine VUMAT. Delamination damage in the plate was simulated by inserting cohesive elements at the interfaces of plies with different orientations. The results of the analysis show that the initial failure mechanism is the matrix cracking in the lowermost plies independent from the stacking sequence of the laminate. Although matrix cracking does not lead to a considerable drop in the impact load, it should be taken into account in the analyses

since it promotes formation of delamination which is one of the most energy dissipative failure modes of composites.

6.4. Concluding Remarks and Future Work

In this thesis, numerical simulations of impact experiments on composite beams and plates were conducted and results of the simulations were compared with the experimental results. Overall, good agreement was obtained between the results of simulations and experiments in terms of initiation, progression and final shape of the damage. However, an important observation was made on the difference in delamination speeds obtained from the beam experiments and the simulations. In the scope of this thesis, a case study in simulations were repeated using different values of interface properties was performed. It was concluded that dynamic values of interface properties can have an effect on the accuracy of dynamic failure simulations. Further investigation might be useful for better understanding of the physical reasoning behind this difference observed in the experiments and the simulations.

In the static and impact experiments conducted on composite beams, it was observed that there was no exact location of the initial matrix crack. This uncertainty might be due to local fluctuations in strength properties of composite materials. In order to induce the crack location uncertainty in simulations, randomly fluctuated strength properties around an average value can be implemented to the finite element model.

In addition to the above-mentioned discussions, a single experiment was modeled with the virtual plate impact test setup. Although the impact event including contact, damage formation and rebounding was simulated successfully, further investigation is needed to discover deficiencies of the finite element model since several assumptions were made in development of the virtual test setup. For this purpose, remaining experiments, which are presented also in this thesis, would be simulated using the finite element model.

In conclusion, results obtained from the experiments and the simulations of both beams and plates were agreed well in general. Several exciting observations that can

lead to accurate simulations were made in the experiments. Besides the interesting results of the experiments and simulations performed in the study, I believe that the methodology followed in the thesis can be used as a guide for the development of high fidelity virtual test setups.





REFERENCES

- [1] Choi, H. Y., Downs, R. J., & Chang, F. K. (1991). A new approach toward understanding damage mechanisms and mechanics of laminated composites due to low-velocity impact: Part I—experiments. *Journal of Composite Materials*, 25(8), 992-1011.
- [2] Rechak, S., & Sun, C. T. (1990). Optimal use of adhesive layers in reducing impact damage in composite laminates. *Journal of Reinforced Plastics and Composites*, 9(6), 569-582.
- [3] Lopes, C., Gurdal, Z., Camanho, P., Maimi, P., & Gonzalez, E. (2009). Simulation of low-velocity impact damage on composite laminates. In 50th AIAA/ASME/ASCE/AHS/ASC Structures, Structural Dynamics, and Materials Conference, at Palm Springs, California, USA.
- [4] Lopes, C. S., Camanho, P. P., Gürdal, Z., Maimí, P., & González, E. V. (2009). Low-velocity impact damage on dispersed stacking sequence laminates. Part II: Numerical simulations. *Composites Science and Technology*, 69(7-8), 937-947.
- [5] Lopes, C. S., Sádaba, S. S., Camanho, P. P., & González, C. (2014). Advanced simulation of low velocity impact on fibre reinforced laminates. In 4th International Conference on Impact Loading of Lightweight Structures (ICCILS 2014), at Cape Town, South Africa.
- [6] Lopes, C. S., Sádaba, S., González, C., Llorca, J., & Camanho, P. P. (2016). Physically-sound simulation of low-velocity impact on fiber reinforced laminates. *International Journal of Impact Engineering*, 92, 3-17.
- [7] González, E. V., Maimí, P., Camanho, P. P., Turon, A., & Mayugo, J. A. (2012). Simulation of drop-weight impact and compression after impact tests on composite laminates. *Composite Structures*, 94(11), 3364-3378.

- [8] Soto, A., González, E. V., Maimí, P., De La Escalera, F. M., De Aja, J. S., & Alvarez, E. (2018). Low velocity impact and compression after impact simulation of thin ply laminates. *Composites Part A: Applied Science and Manufacturing*, 109, 413-427.
- [9] Topac, O. T., Gozluklu, B., Gurses, E., & Coker, D. (2017). Experimental and computational study of the damage process in CFRP composite beams under low-velocity impact. *Composites Part A: Applied Science and Manufacturing*, 92, 167-182.
- [10] Hashin, Z., & Rotem, A. (1973). A fatigue failure criterion for fiber reinforced materials. *Journal of Composite Materials*, 7(4), 448-464.
- [11] Hashin, Z. (1980). Failure criteria for unidirectional fiber composites. *Journal of Applied Mechanics*, 47(2), 329-334.
- [12] Puck, A. (1969). Calculating the strength of glass fibre/plastic laminates under combined load. *Kunststoffe*, 55, 18-19.
- [13] Puck, A., & Schneider, W. (1969). On failure mechanisms and failure criteria of filament-wound glass-fibre/resin composites. *Plastics & Polymers*, 37(127), 33-44.
- [14] Hinton, M. J., & Soden, P. D. (1998). Predicting failure in composite laminates: the background to the exercise. *Composites Science and Technology*, 58(7), 1001-1010.
- [15] Pinho, S. T., Dávila, C. G., Camanho, P. P., Iannucci, L., & Robinson, P. (2005). Failure models and criteria for FRP under in-plane or three-dimensional stress states including shear non-linearity. NASA/TM-2003-213530.
- [16] Pinho, S. T., Darvizeh, R., Robinson, P., Schuecker, C., & Camanho, P. P. (2012). Material and structural response of polymer-matrix fibre-reinforced composites. *Journal of Composite Materials*, 46(19-20), 2313-2341.

- [17] Kachanov, L. M. (1958). Time of the rupture process under creep conditions, *Izy Akad. Nank SSR Otd Tech Nauk*, 8, 26-31.
- [18] Malvern, L. E. (1969). *Introduction to the Mechanics of a Continuous Medium*. Englewood Cliffs, NJ: Prentice-Hall.
- [19] Matzenmiller, A. L. J. T. R., Lubliner, J., & Taylor, R. L. (1995). A constitutive model for anisotropic damage in fiber-composites. *Mechanics of Materials*, 20(2), 125-152.
- [20] Ladevèze, P., Allix, O., Deü, J. F., & Lévêque, D. (2000). A mesomodel for localisation and damage computation in laminates. *Computer Methods in Applied Mechanics and Engineering*, 183(1-2), 105-122.
- [21] Barbero, E. J., & De Vivo, L. (2001). A constitutive model for elastic damage in fiber-reinforced PMC laminae. *International Journal of Damage Mechanics*, 10(1), 73-93.
- [22] Lonetti, P., Barbero, E. J. (2001). Damage model for composites defined in terms of available data. *Mechanics of Composite Materials and Structures*, 8(4), 299-315.
- [23] Oller, S., Botello, S., Miquel, J., & Oñate, E. (1995). An anisotropic elastoplastic model based on an isotropic formulation. *Engineering Computations*, 12(3), 245-262.
- [24] Williams, K. V., Vaziri, R., & Poursartip, A. (2003). A physically based continuum damage mechanics model for thin laminated composite structures. *International Journal of Solids and Structures*, 40(9), 2267-2300.
- [25] Maimí, P., Camanho, P. P., Mayugo, J. A., & Dávila, C. G. (2007). A continuum damage model for composite laminates: Part I—Constitutive model. *Mechanics of Materials*, 39(10), 897-908.

- [26] Maimí, P., Camanho, P. P., Mayugo, J. A., & Dávila, C. G. (2007). A continuum damage model for composite laminates: Part II—Computational implementation and validation. *Mechanics of Materials*, 39(10), 909-919.
- [27] Dvorak, G. J., & Laws, N. (1987). Analysis of progressive matrix cracking in composite laminates II. First ply failure. *Journal of Composite Materials*, 21(4), 309-329.
- [28] Camanho, P. P., Dávila, C. G., Pinho, S. T., Iannucci, L., & Robinson, P. (2006). Prediction of in situ strengths and matrix cracking in composites under transverse tension and in-plane shear. *Composites Part A: Applied Science and Manufacturing*, 37(2), 165-176.
- [29] Camanho, P. P., & Dávila, C. G. (2002). Mixed-mode decohesion finite elements for the simulation of delamination in composite materials. *NASA/TM-211737*, 1-37.
- [30] English, S. A. (2014). A 3D orthotropic strain-rate dependent elastic damage material model. Livermore (California): Sandia Labs.
- [31] Gözlüklü, B. (2014). Modelling of intersonic delamination in curved-thick composite laminates under quasi-static loading (PhD Thesis). Ankara, Turkey: Middle East Technical University.
- [32] Benzeggagh, M. L., & Kenane, M. J. C. S. (1996). Measurement of mixed-mode delamination fracture toughness of unidirectional glass/epoxy composites with mixed-mode bending apparatus. *Composites Science and Technology*, 56(4), 439-449.
- [33] Crews Jr, J. H., & Reeder, J. R. (1988). A mixed-mode bending apparatus for delamination testing. *NASA/TM-100662*.
- [34] ASTM D6415/D6415-06a. (2013). Standard test method for measuring the curved beam strength of a fiber-reinforced polymer-matrix composite. West

Conshohocken, PA, United States: American Society for Testing and Materials.

- [35] ASTM D2344/D2344M-16. (2016). Standard test method for short-beam strength of polymer matrix composite materials. West Conshohocken, PA, United States: American Society for Testing and Materials.
- [36] ASTM D5528-13. (2013). Standard test method for mode I interlaminar fracture toughness of unidirectional fiber-reinforced polymer matrix composites. West Conshohocken, PA, United States: American Society for Testing and Materials.
- [37] ASTM D7905/D7905-19. (2019). Standard test method for determination of the mode II interlaminar fracture toughness of unidirectional fiber-reinforced polymer matrix composites. West Conshohocken, PA, United States: American Society for Testing and Materials.
- [38] Yang, Q., & Cox, B. (2005). Cohesive models for damage evolution in laminated composites. *International Journal of Fracture*, 133(2), 107-137.
- [39] González, E. V., Maimí, P., Camanho, P. P., Lopes, C. S., & Blanco, N. (2011). Effects of ply clustering in laminated composite plates under low-velocity impact loading. *Composites Science and Technology*, 71(6), 805-817.
- [40] Christoforou, A. P., & Yigit, A. S. (1998). Effect of flexibility on low velocity impact response. *Journal of Sound and Vibration*, 217(3), 563-578.
- [41] Christoforou, A. P., & Yigit, A. S. (1998). Characterization of impact in composite plates. *Composite Structures*, 43(1), 15-24.
- [42] Christoforou, A. P. (2001). Impact dynamics and damage in composite structures. *Composite Structures*, 52(2), 181-188.

- [43] Yigit, A. S., & Christoforou, A. P. (2007). Limits of asymptotic solutions in low-velocity impact of composite plates. *Composite Structures*, 81(4), 568-574.
- [44] Olsson, R. (2000). Mass criterion for wave controlled impact response of composite plates. *Composites Part A: Applied Science and Manufacturing*, 31(8), 879-887.
- [45] Yigit, A. S., & Christoforou, A. P. (1994). On the impact of a spherical indenter and an elastic-plastic transversely isotropic half-space. *Composites Engineering*, 4(11), 1143-1152.
- [46] ASTM D7136/D7136M-15. (2015). Standard test method for measuring the damage resistance of a fiber-reinforced polymer matrix composite to a drop-weight impact event. West Conshohocken, PA, United States: American Society for Testing and Materials.
- [47] Suemasu, H., & Majima, O. (1996). Multiple delaminations and their severity in circular axisymmetric plates subjected to transverse loading. *Journal of Composite Materials*, 30(4), 441-453.
- [48] Lopes, C. S., Seresta, O., Coquet, Y., Gürdal, Z., Camanho, P. P., & Thuis, B. (2009). Low-velocity impact damage on dispersed stacking sequence laminates. Part I: Experiments. *Composites Science and Technology*, 69(7-8), 926-936.
- [49] ASTM D3039/D3039M-17. (2017). Standard test method for tensile properties of polymer matrix composite materials. West Conshohocken, PA, United States: American Society for Testing and Materials.
- [50] ASTM D3410/D3410M-16. (2016). Standard test method for compressive properties of polymer matrix composite materials with unsupported gage section by shear loading. West Conshohocken, PA, United States: American Society for Testing and Materials.

- [51] ASTM D3518/D3518M-18. (2018). Standard test method for in-plane shear response of polymer matrix composite materials by tensile test of a 45 laminate. West Conshohocken, PA, United States: American Society for Testing and Materials.
- [52] Bažant, Z. P., & Oh, B. H. (1983). Crack band theory for fracture of concrete. *Matériaux et Construction*, 16(3), 155-177.
- [53] Pinho, S. T., Robinson, P., & Iannucci, L. (2006). Fracture toughness of the tensile and compressive fibre failure modes in laminated composites. *Composites Science and Technology*, 66(13), 2069-2079.
- [54] Song, K., Dávila, C. G., & Rose, C. A. (2008). Guidelines and parameter selection for the simulation of progressive delamination. In: *Proceedings of the 2008 Abaqus Users' Conference: May 19–22, Newport, Rhode Island, USA*. Dassault Systemes.
- [55] Turon, A., Davila, C. G., Camanho, P. P., & Costa, J. (2007). An engineering solution for mesh size effects in the simulation of delamination using cohesive zone models. *Engineering Fracture Mechanics*, 74(10), 1665-1682.
- [56] Turon, A., Camanho, P. P., Costa, J., & Renart, J. (2010). Accurate simulation of delamination growth under mixed-mode loading using cohesive elements: definition of interlaminar strengths and elastic stiffness. *Composite Structures*, 92(8), 1857-1864.